Transformations in the electronic subsystem of metal solid solutions near a radiation-induced phase transition

V. S. Khmelevskaya, V. G. Malynkin, and M. Yu. Kanunnikov

Institute of Nuclear Power Engineering, Obninsk
(Submitted April 25, 1998)
Pis'ma Zh. Tekh. Fiz. **24**, 1–8 (December 12, 1998)

Nonmonotonic changes in the mechanical properties of various alloys are demonstrated under the action of radiation which stimulates phase transitions. A comparison with the results of measurements of the thermoelectric power confirmed the assumption that the nature of the interparticle bonds changes. © *1998 American Institute of Physics.* [S1063-7850(98)00112-8]

It has been observed[1–3] that in metal solid solutions exposed to ion bombardment a special state of matter forms in a narrow range of radiation parameters (doses, irradiation temperatures, and flux densities). This state is characterized by heterophase properties occurring in a previously homogeneous equilibrium material, the properties change substantially (particularly the microhardness), and an unusual morphology appears (spatial self-organization).

This set of properties can identify this state as a dissipative structure predicted by the thermodynamics of irreversible processes ''far from equilibrium,''[4,5] and the observed transformation can be regarded as a kinetic phase transition.

This solid state has unique properties for different materials (Fe–Ni, Fe–Cr–Ni, and Cu–Ni fcc alloys, Fe–Cr and V–Ti–Cr bcc alloys, and pure Zr and Ti metals with an hcp crystal lattice) and different methods of ion bombardment (accelerator, plasma, cw and pulsed). When the ion energy and species and the ion flux intensity vary, the properties of the state are the same, although it appears in a different range of external parameters.

The principal indicator for this state is a change in the x-ray diffraction pattern which denotes the appearance of heterophase properties, i.e., splitting of the diffraction peaks or a specific change in their shape.[3] At the same time, substantial changes in the properties and structural morphology are observed in the range of diffraction effects. Figure 1 shows an example of structures observed on two different scale levels (using metallography and electron microscopy). Both cases reveal a clearly defined spatial organization.

In many cases, the changes in the properties of alloys, especially the microhardness, in the region of existence of these dissipative structures are anomalously large. For example, in Fe–Cr alloys the microhardness exceeds 10 000 MPa (initial value 2000 MPa), in V–Ti–Cr alloys it exceeds 12 000 (initial value 1600 MPa), and in Fe–Cr–Ni alloys it is around 7000 MPa (initial value 1500 MPa). Such a high level of microhardness in metals cannot be described in terms of any dislocation mechanism and has thus been assumed that the state of the metallic bond changes in the region of the dissipative structure.

In order to check out this idea, we measured the temperature dependence of the thermoelectric power. For the experiments we used Fe–12Cr–Mo–V–Nb, V–4Ti–4Cr, and Fe–18Cr–10Ni–Ti alloys for which the initial state was a solid solution in all cases. The samples were bombarded by 40 keV Ar^+ ions in an accelerator at various irradiation temperatures (between room temperature and 900 °C for V–Ti–Cr and between room temperature and 600 °C for Fe–Cr–Ni) and to various doses (Fe–Cr, 500 °C, between 0.5×10^{18} and 1.5×10^{18} ions/cm^2). The thermoelectric power was measured by an integration method[6] using an

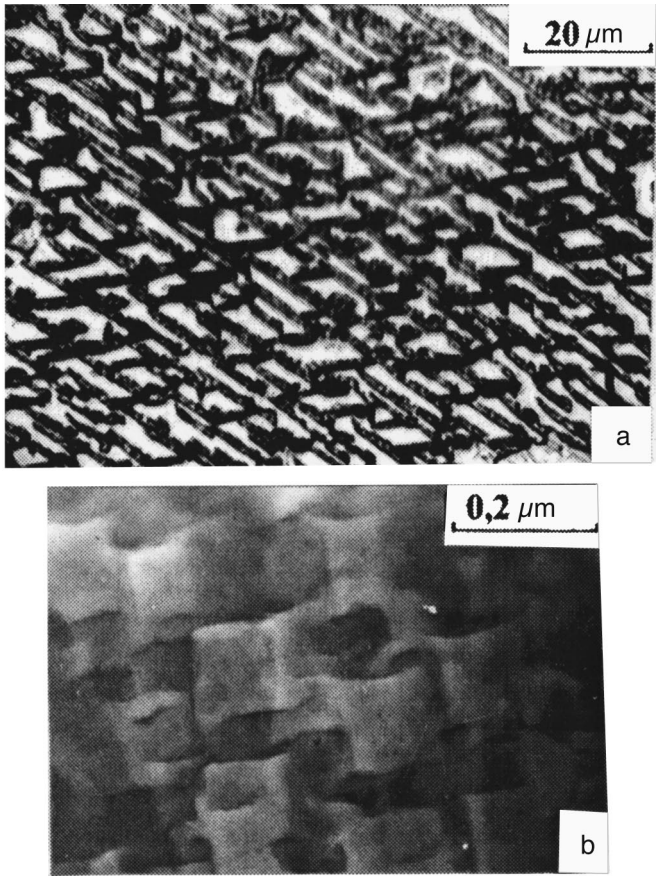

FIG. 1. Microstructure of Fe–12Cr–Mo–W–V–Nb alloy recorded by metallographic analysis (a) and electron microscopy (b).

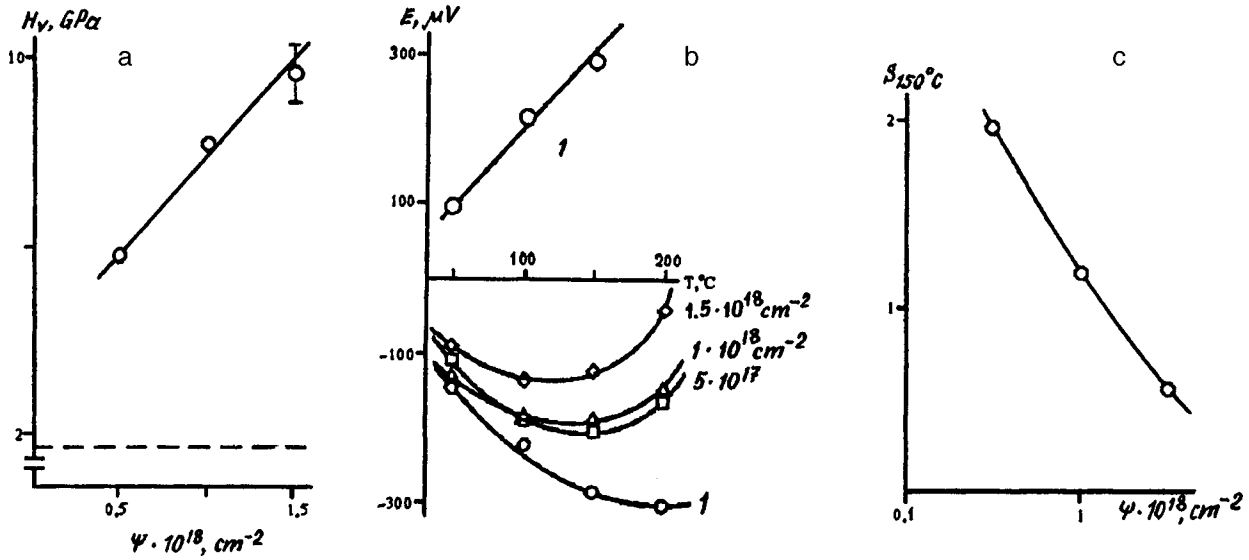

FIG. 2. Microhardness (a) (the dashed line gives the initial value), temperature dependence of the thermoelectric power (b) (*1* — initial value), and temperature coefficient of thermoelectric power (c) in Fe–12Cr–Mo–W–V–Nb alloy bombarded by 40 keV Ar^- ions (500 °C) to different doses; *1* — σ-phase.

apparatus based on a PMT-3 microhardness meter in which the indenter was replaced by a tungsten tip on which was placed a microfurnace brought in contact with the surface of the metal (hot junction). The results of the measurements are shown in Figs. 2–4.

For irradiated Fe–Cr alloys in the range of parameters in which a dissipative structure exists (Fig. 2), the slope of the temperature dependence $E(T)$ varies from the initial sample with radiation dose, the largest changes being observed at the highest dose of 1.5×10^{18} ions/cm^2 and the slope $S=-dE/dT$ being the opposite of that in the initial sample. Also plotted for comparison is the curve of $E(T)$ for the σ phase of the FeCr intermetallide with a predominantly covalent bond. It can be seen that S has different signs in the metal solid solution and the intermetallide. Thus, as the dose increases, the ''metallic'' coefficient of thermoelectric power rotates to the ''covalent'' coefficient and the changes in S correlate with the changes in the microhardness.

The same ''dielectrification'' is observed for the V–Ti–Cr alloy. In this case, a dissipative structure appears at irradiation temperatures in the range 500–700°, which corresponds to the strongest radiation hardening (Fig. 3). The slope of $E(T)$ varies from the initial value at 100° to 200°, and then increases until 600°, where all the effects are strongest, and then returns to the initial value at higher temperatures. The changes in S calculated using these curves corresponds to the changes in microhardness.

The same correlation was observed for Fe–Cr–Ni alloys (Fig. 4). The slope of the temperature dependence of the

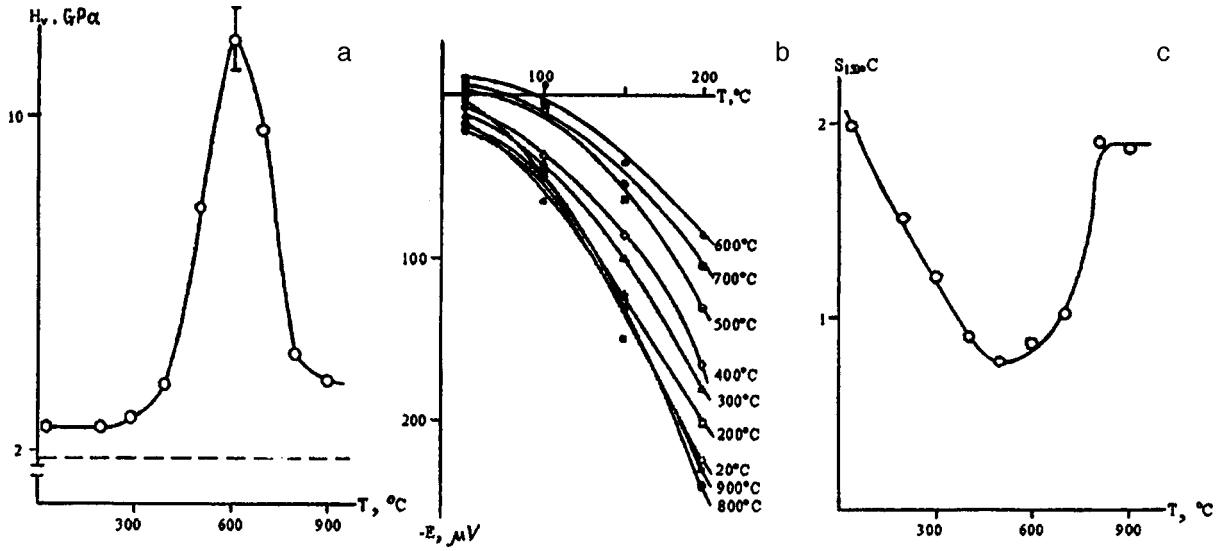

FIG. 3. Microhardness (a) (the dashed gives the initial value), temperature dependence of the thermoelectric power (b), and temperature coefficient of thermoelectric power (c) in V–4Ti–4Cr alloy bombarded by 40 keV Ar^+ ions (1.5×10^{18} ions/cm^2) to different temperatures.

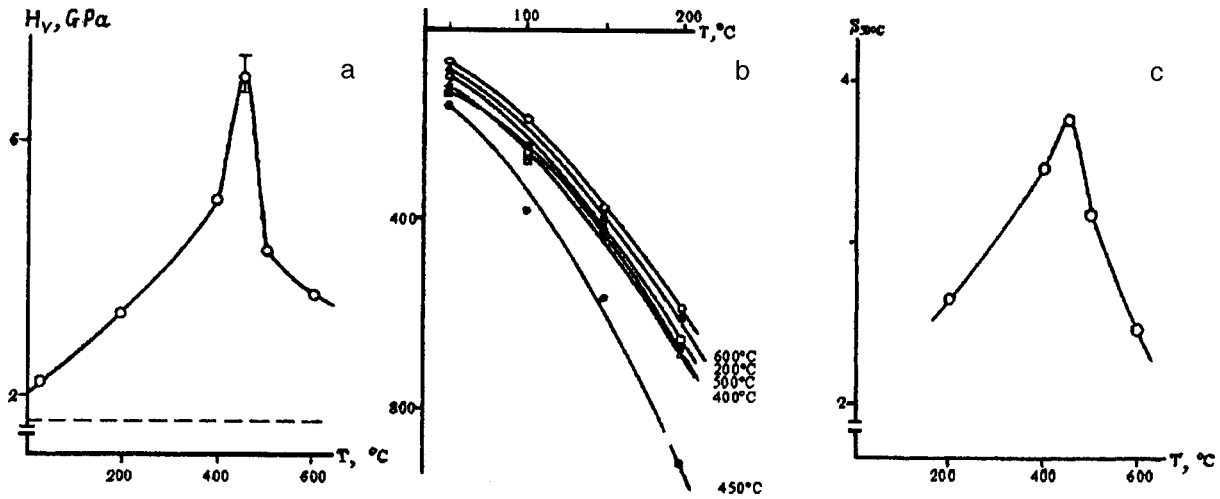

FIG. 4. Microhardness (a), temperature dependence of the thermoelectric power (b), and temperature coefficient of thermoelectric power (c) in Fe–18Cr–10Ni–Ti alloy bombarded by 40 keV Ar^+ ions (1.5×10^{18} ions/cm^2) to different temperatures.

thermoelectric power also varies in parallel with the other effects but the sign of the changes is the opposite of that observed for Fe–Cr and V–Ti–Cr alloys. We can postulate that this is caused by differences in the electronic structure in the two different crystal lattices, i.e., bcc (Fe–Cr and V–Ti–Cr alloys) and fcc (Fe–Cr–Ni).

We know that S is a function of the derivative of the density of states at the Fermi surface. Such differences are quite feasible in alloys of transition metals with multiply connected Fermi surfaces.

The authors would like to thank Professor V. G. Vaks for extremely valuable comments and interest in this work.

This work was supported by the Russian Fund for Fundamental Research, Project No. 96–021632a.

[1] V. S. Khmelevskaya, S. P. Solov'ev, and V. G. Malynkin, Itogi Nauki i Tekhn. Ser. Puchki Zar. Chastits i Tverd. Telo **2**, 151 (1990).
[2] V. S. Khmelevskaya, V. G. Malynkin, and S. P. Solovyev, J. Nucl. Mater. **199**, 214 (1993).
[3] V. S. Khmelevskaya and V. G. Malynkin, Phase Transit. **60**, 59 (1997).
[4] G. Nicolis and I. Prigogine, *Self-Organization in Nonequilibrium Systems* (Wiley, New York, 1977).
[5] G. Haken, *Synergetics* (Springer-Verlag, Berlin, 1978).
[6] F. A. Blatt, P. A. Shroeder, K. L. Foiles, and D. Greig, *Thermoelectric Power of Metals* (Plenum Press, New York, 1976).

Translated by R. M. Durham

Long-range influence of weak photon irradiation (0.95 μm wavelength) on the mechanical properties of metals

D. I. Tetel'baum, A. A. Trofimov, A. Yu. Azov, E. V. Kuril'chik, and E. E. Dotsenko

Physicotechnical Research Institute at the N. I. Lobachevskiĭ State University, Nizhniĭ Novgorod
(Submitted December 2, 1997; resubmitted April 30, 1998)
Pis'ma Zh. Tekh. Fiz. **24**, 9–13 (December 12, 1998)

It has been established that when 18 μm thick permalloy foils are exposed to 0.95 μm light for 0.2–100 s, the microhardness increases on both sides. This effect is not caused by radiation heating and is discussed in terms of a model proposed earlier to explain a low-dose long-range effect under ion bombardment. © *1998 American Institute of Physics.* [S1063-7850(98)00212-2]

We have already observed[1–5] changes in the mechanical properties of rolled metal foils at low (10^{13}–10^{16} cm^{-2}) ion or electron irradiation doses. Since the changes extend over distances much greater than the ranges of the bombarding particles (as far as the opposite sides of foils 10–100 μm thick), this effect has been called a low-dose long-range effect. The model proposed by us[6] indicates that this effect is caused by the action of radiation-excited elastic waves on a system of extended defects. A characteristic feature of this effect is that it is observed not only under irradiation conditions when atoms can be knocked from sites and the particle energy is dissipated mainly in elastic (nuclear) losses but also when atoms cannot be directly knocked out and the particles are slowed predominantly by inelastic (electron) energy losses. This factor has stimulated experiments in which the electronic system of a metal is excited by optical (laser) radiation rather than by corpuscular radiation, with an average power density of the same order of magnitude as that for corpuscular radiation. In this case, the macroscopic heating is negligible and energy is absorbed mainly in a thin surface layer of the foil. The main difference is that under corpuscular irradiation energy is introduced as space–time ''bunches'' (cascades), whereas under optical irradiation, the energy is quasiuniform in the plane parallel to the surface.

Here we used permalloy-79 foils, the material for which the most investigations have been made of the low-dose long-range effect. The foils were 18 μm thick and illumination was provided by 0.95 μm cw semiconductor laser radiation with power density 0.25 W/cm^2. The microhardness H was measured using a PMT-3 microhardness meter. The data were averaged over ten indentations, each of which was measured four times. The mean arithmetic error was less than 3% at the 0.9 confidence level. The deviations of H for different samples prior to irradiation were also within this limit. The load was 50 g, for which the indentation depth was $\sim$1.5 μm.

Figure 1 shows the relative changes in H induced by irradiation, on the irradiated side and on the opposite side of the foil, plotted as a function of the illumination time τ (since the duration was measured in seconds, the value $\tau = 0.2$ s is very approximate). It can be seen that the microhardness increments $(\Delta H/H)$ substantially exceed the error and the systematic nature of the dependence on τ serves as additional evidence that the effect is realistic. The decrease in the increment $(\Delta H/H)$ with irradiation time indicates that the $(\Delta H/H)$ curve must have a maximum at a time of less than 0.2 s.

In order to check that the change in H under irradiation is not caused by heating of the sample by the laser beam, we determined the values of H for foils exposed to brief annealing (2 min) in a furnace at temperatures up to 373 K. No changes in H compared with the initial value were observed within experimental error. In our case, the temperature of the samples under irradiation is known to be lower than 373 K, i.e., the observed effect is not caused by radiation heating.

We shall now discuss this effect. We know from the literature[7,8] that exposure of solids to hard (vacuum) ultraviolet radiation may give rise to defects. However, the defect formation mechanisms proposed by Klinger *et al.*[7] and Koz'ma *et al.*[8] clearly cannot be applied directly to the infrared (0.95 μm). In addition, they do not explain why the changes in H observed on the opposite side of the foil are greater than those on the irradiated side. We are also familiar with a photomechanical effect[9] in which illumination directly during indentation influences the depth of indentation in measurements of H. In our case, however, the change in H occurs after illumination and persists for at least a month (although the changes do undergo partial relaxation over a few days or weeks). In order to emphasize the difference from the photomechanical effect,[9] it is appropriate to call this effect a photomechanical metal memory effect.

In our view, following the reasoning put forward at the beginning of this article, the nature of the effect is basically the same as the low-dose long-range effect under ion bombardment: changes in H are caused by the generation of elastic waves and their action on initial extended defects such as dislocations, grain boundaries, and so on. Further details of this mechanism are given in Refs. 1–6. An important role in the generation of elastic waves under photon irradiation may be played by the internal photoeffect in which electrons are knocked out of the metal into the natural oxide, followed by the evolution of processes similar to those described by Klinger *et al.*[7] However, point defects are not necessarily formed in the oxide—elastic waves can be generated by im-

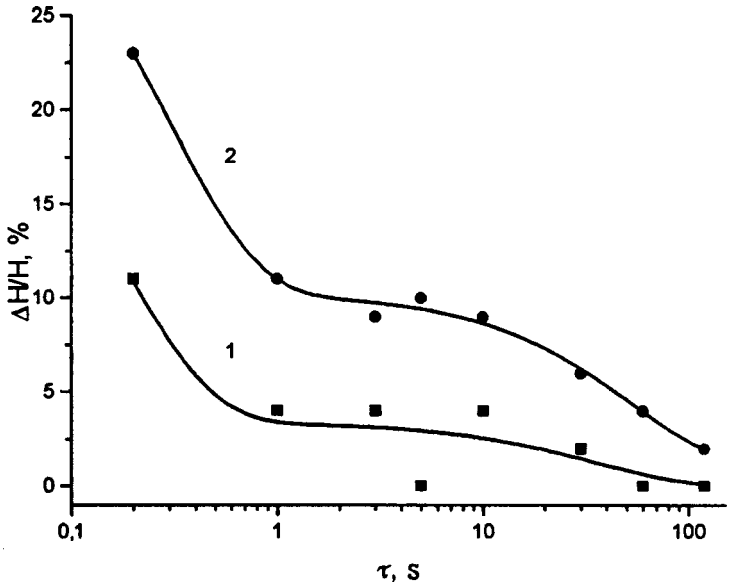

FIG. 1. Relative changes in microhardness versus illumination time: *1* — irradiated side, *2* — opposite side.

parting momenta to the oxide atoms as a result of the Coulomb forces associated with charge transfer.

The nonmonotonic variation of $(\Delta H/H)$ with irradiation time may be similar to that for the nonmonotonic dependence on the dose under ion bombardment. According to the elastic wave model, $(\Delta H/H)$ may be larger on the unirradiated side than on the irradiated side because of competition between elastic wave attenuation (dissipation) and amplification in secondary processes.[10] Obviously, these explanations are of a preliminary nature, since the effect requires more detailed study. Note that we established an effect similar to that described not only for permalloy foils but also for copper ones. Moreover, preliminary experiments have shown that as under ion bombardment,[5] the changes in H are transferred across the interfaces of the foils when stacks are irradiated. We hypothesize that this effect is fairly general and is characteristic of solids with a high degree of structural imperfection.

[1] P. V. Pavlov, D. I. Tetel'baum, E. V. Kuril'chik *et al.*, Vysokochast. Veshchest. No. 4, 26 (1993).
[2] D. I. Tetel'baum and E. V. Kuril'chik, Vysokochast. Veshchest. No. 2, 98 (1995).
[3] D. I. Tetel'baum, V. P. Sorvina, and E. V. Kuril'chik, Izv. Ross. Akad. Nauk, Ser. Fiz. **60**(5), 210 (1996).
[4] D. I. Tetel'baum, E. V. Kuril'chik, A. I. Sidorova *et al.*, Metally No. 5, 114 (1996).
[5] D. I. Tetelbaum, E. V. Kurilchik, and N. D. Latisheva, Nucl. Instrum. Methods Phys. Res. B **127/128**, 153 (1997).
[6] P. V. Pavlov, Yu. A. Semin, V. D. Skupov *et al.*, Fiz. Tekh. Poluprovodn. **20**, 503 (1986) [Sov. Phys. Semicond. **20**, 315 (1986)].
[7] M. I. Klinger, Ch. B. Lushchik, T. V. Mashovets *et al.*, Usp. Fiz. Nauk **147**, 523(1985) [Sov. Phys. Usp. **28**, 994 (1985)].
[8] A. S. Koz'ma, S. V. Malykhin, O. V. Sobol' *et al.*, Fiz. Metall. Metalloved. No. 7, 168 (1991).
[9] N. N. Novikov, Ukr. Fiz. Zh. **17**, 724 (1972).
[10] Yu. A. Semin, V. D. Skupov, and D. I. Tetel'baum, Pis'ma Zh. Tekh. Fiz. **14**, 273 (1988) [Sov. Tech. Phys. Lett. **14**, 121 (1988)].

Translated by R. M. Durham

Hardening of metals exposed to ultraviolet radiation

A. I. Fedorov

Institute of Atmospheric Optics, Siberian Branch of the Russian Academy of Sciences, Tomsk
(Submitted November 10, 1997; resubmitted April 10, 1998)
Pis'ma Zh. Tekh. Fiz. **24**, 14–18 (December 12, 1998)

Results are presented of experimental investigations of various regimes for exposure of metal samples (steel 45) to XeCl laser radiation to enhance their microhardness and wear resistance. The specific power and radiation energy were varied between 7.5×10^6 and 1×10^8 W/cm^2 and between 1 and 20 J/cm^2, respectively. It was shown that a specific microhardness can be predefined for surface layers of metal to depths up to 300 μm as a function of the irradiation regime. © *1998 American Institute of Physics.* [S1063-7850(98)00312-7]

The development of high-power ultraviolet excimer lasers has stimulated the search for their possible applications in new technologies.[1–3] This explains the increased interest being shown in experimental and theoretical investigations of the interaction between ultraviolet radiation and metals.[4–6] At present we do not have any clear physical picture of the action of ultraviolet excimer laser radiation on metals. Arutyunyan *et al.*[4] reported experimental and theoretical investigations of the action of pulse-periodic XeCl laser radiation of intensity $\sim10^6-10^8$ W/cm^2 on various metal targets (Al, Cu, Ti) in vacuum and in various buffer gas media. These authors showed that at high radiation intensities the metal target is heated more slowly because of the pulsed energy losses to vaporization, whereas at low intensities this slowing is caused by thermal radiation and transfer of heat into the metal. The power density was taken to be the main factor in the action, while the role of the energy density was neglected in connection with the interaction between the radiation and the metals.

Here, results of experimental investigations of the action of XeCl laser radiation on metal samples (steel 45) are reported, which indicate that their microhardness and wear resistance are enhanced, depending on the irradiation regimes.

In the experiments the laser radiation intensity (W) acting on the samples was varied between 7.5×10^6 and 1×10^8 W/cm^2 and the energy density (Q) was varied between 1 and 20 J/cm^2 for pulse lengths between 30 and 200 ns. The investigations were carried out using three steel samples (I–III) which had undergone conventional heat treatment (quenching, tempering). The initial microhardness H_1 after heat treatment had the following values: I — 600 kgf/mm^2, II — 620 kgf/mm^2, and III — 650 kgf/mm^2. The front surface of samples II and III was exposed to laser radiation in the following regimes: (*1*) $Q=1.5$ J/cm^2, $W=7.5\times10^6$ W/cm^2; (*2*) $Q=5$ J/cm^2, $W=2.5\times10^7$ W/cm^2; (*3*) $Q=10$ J/cm^2, $W=5\times10^7$ W/cm^2; and (*4*) $Q=20$ J/cm^2, $W=1\times10^8$ W/cm^2.

The microhardness measurements were made using a PMT-3 device with load $P=0.1$ kg. At the surface of the samples the microhardness varied as follows: sample II: 680 (*1*), 570 kgf/mm^2; sample III: 440 (*3*) and 820 (*4*) kgf/mm^2, where (*1*—*4*) are the laser irradiation regimes. Depending on the energy density and the radiation intensity, the surface

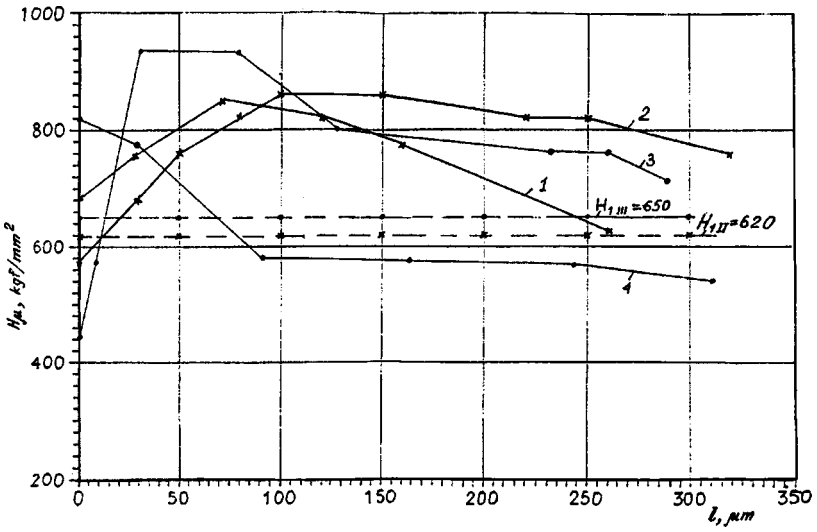

FIG. 1. Changes in microhardness versus depth for steel 45 samples II and III exposed to XeCl laser radiation in regimes *1–4*.

microhardness decreased (regime *3*) or increased (regime *4*) up to 25%. The decrease in the microhardness was caused by self-diffusion of carbon under irradiation, while the increase was evidently attributable to surface evaporation of the metal.

The variation of the microhardness with sample depth was of the greatest interest. To measure this, a transverse cut was made and the surface was then ground and polished (without cold hardening, i.e., surface hardening). The microhardness measurements were made using the PMT-3 device by varying the depth of the cut with an approximate step of 50 μm. Figure 1 gives the microhardness (H_μ) of samples II and III over the depth (1 μm) of a transverse polished section as a function of the irradiation regimes (*1–4*) for $H_1 = 620$ (II) and 650 (III) kgf/mm^2. For regimes (*1–3*) H_μ increased with sample depth as the energy density and radiation intensity increased as a result of heat being transferred into the metal. A further increase in the energy density to 20 J/cm^2 and the radiation intensity to 1×10^8 W/cm^2 (regime *4*) was accompanied by the opposite effect. The surface microhardness increased and then decreased almost linearly to a depth of ~ 100 μm, then remaining constant below the initial level as a result of tempering of the material caused by overheating. Thus, depending on the irradiation regime, the microhardness H_μ can vary with the depth of the material as far as 300 μm.

The samples were also investigated for wear resistance using a type of disk-block. The counterbody was a ShKh 15 steel disk coated with titanium nitride. The wear investigations were carried out in air with the parameters $P = 25$ kgf and $\nu = 80$ rpm. Figure 2 gives the mass loss as a function of time. Since the samples were heated appreciably after long abrasion times, the wear resistance studies were terminated after 15 min. The curves can be divided into three sections (*1–3*). Section *1* corresponded to abrasion of the sample with the counterbody. In section *2* the mass losses of the irradiated samples differed little from those of the initial sample (I) which is consistent with the microhardness of these samples, (Fig. 1, curves *1* and *2*). In section *3* the wear of sample I differed sharply from that of the irradiated samples II and III.

Thus, these results supplement the conclusion reached by Arutyunyan *et al.*[4] that optimum heating regimes exist for metal samples not only as a function of the laser radiation intensity but also as a function of the energy density and irradiation time. On the basis of these investigations the following results were obtained:

1. It has been shown that the microhardness and wear resistance of metals (using steel 45 as an example) can be enhanced as a function of the ultraviolet irradiation parameters (radiation intensity and energy density).

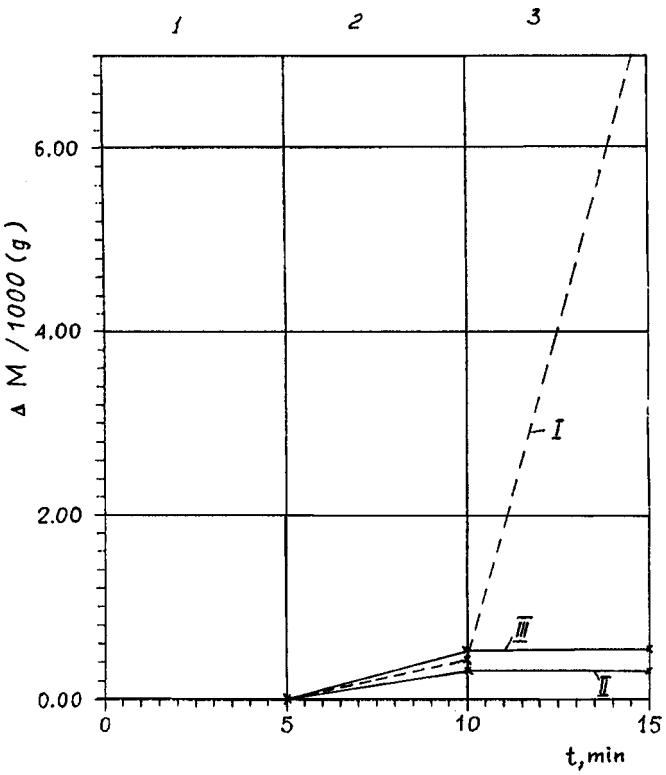

FIG. 2. Relative losses of samples abraded using a friction machine as a function of time for normal (I) and XeCl-laser irradiated samples (II and III).

2. Specific microhardness properties of metal surfaces can be produced over depths up to 300 μm by different thermal regimes of ultraviolet irradiation.

The author would like to thank V. M. Diamant (Republican Engineering Center, Siberian Branch of the Russian Academy of Sciences) for assistance in preparing the microhardness and wear resistance samples.

[1] J. F. Ready, *Lasers in Modern Industry* (Society of Manufacturing Engineers, Dearborn, Mich., 1979; Mir, Moscow, 1981, 638 pp.).
[2] W. W. Duley, *Laser Processing of Materials* (Plenum Press, New York, 1983; Mir, Moscow, 1986, 502 pp.).
[3] U. Sowada, P. Lokai, H. Kahlert, and D. Basting, Laser Optoelektron. **21**(3), 107 (1989).
[4] R. V. Arutyunyan, L. A. Bolshov, V. M. Borisov *et al., Investigation of Regimes of Repetitively Pulsed XeCl–Laser Action on Metals*, Preprint No. 4958/9 [in Russian], Kurchatov Institute of Atomic Energy, Moscow (1989), 48 pp.
[5] B. Godard, P. Murrer, P. Laborde *et al.*, in *Proceedings of "CLEO/ Europe 94"*, Paper CTuG3, p. 42.
[6] A. I. Fedorov, in *Proceedings of Third International Conference on Pulsed Lasers on Atomic and Molecular Transitions*, Tomsk, Russia 1997, p. 29.

Translated by R. M. Durham

Investigation of some characteristics of electron emission from the surface of a PLZT ferroelectric

L. M. Rabkin, G. P. Petin, I. A. Zarubin, and V. N. Ivanov

Rostov-on-Don State University
(Submitted January 19, 1998; resubmitted June 15, 1998)
Pis'ma Zh. Tekh. Fiz. **24**, 19–22 (December 12, 1998)

Results are presented of an investigation of some characteristics of electron emission from the surface of a PLZT ferroelectric (TsTSL in Russian) when a pulsed voltage is applied to the sample. It is shown that the emitted charge is compensated by migration of electric charge through the bulk of the ferroelectric. The energies of the emitted electrons were estimated for a specific ferroelectric sample, and it was shown that the residual gas pressure influences the emitted charge. The results were obtained using a new method for direct measurement of the average pulsed currents in the electrode circuits of the solid-state ferroelectric sample and in the collector circuit. © *1998 American Institute of Physics.* [S1063-7850(98)00412-1]

Information on electron emission from the surface of a ferroelectric was first published in Ref. 1. Polarization reversal by high-voltage pulses persisting on the order of a few tens of nanoseconds gives extremely large pulsed emission currents.[2,3] However, many aspects of the emission mechanism remain unexplained. How is the emitted charge compensated and what is the influence of the residual gases in the vacuum? The present paper attempts to address these issues.

The measuring cell was very similar to those described in Refs. 2 and 3. The sample was a 1 mm thick disk of highly compressed unpolarized PLZT lanthanum-containing lead titanate zirconate ceramic (having the composition 9/35/65) with a diameter of 12 mm. Silver electrodes were deposited on the sample, consisting of a solid 10 mm diameter electrode on one side and a grid with period 0.2 mm and spacing 0.2 mm on the side facing the collector. The collector in the form of a metal cup was moved up to the sample and completely collected all the emitted electrons. The distance between the sample and the inner surface of the collector was 5–6 mm. The high-voltage pulse had the following parameters: amplitude up to 3000 V and width at half-maximum 70 ns. The pulse repetition frequency was 10 Hz. The measuring system allowed us to determine the average currents in the electrode circuit rather than the pulsed values of the current or charges,[2,3] so that it was possible to measure the current in the solid electrode circuit and the current in the grid circuit.

Figure 1 gives the average current in the solid electrode circuit (input current I_{in}), the grid current I_g, and the collector current (output current I_{out}) plotted as a function of the collector voltage for a constant pulsed voltage. Particular attention is drawn to the existence of an input current I_{in}, i.e., a current caused by the migration of charges between the solid and grid electrodes. This current was previously unknown and is most likely a hole current. The current balance condition $I_{\text{in}}=I_{\text{out}}+I_g$ is satisfied. The output current and the grid current depend strongly on the collector potential, whereas the input current depends very little on this potential. The following pattern of events emerges. The electrons leaving the ferroelectric have an appreciable energy spread and possess considerable energy, in the present case up to 600 eV. When the collector potential is negative, some of the electrons cannot overcome the retarding collector potential and return to the grid. The grid current increases and the collector current decreases, almost to zero. When the collector potential is positive, an increasingly large number of emitted electrons reach the collector as its potential increases and the grid current decreases and may become very small.

The dependences of all the measured average currents on the residual gas pressure were then measured when a pulsed voltage was applied to the sample. The measurements were made at zero collector potential and the results are plotted in Fig. 2. The average input and output currents are very similar

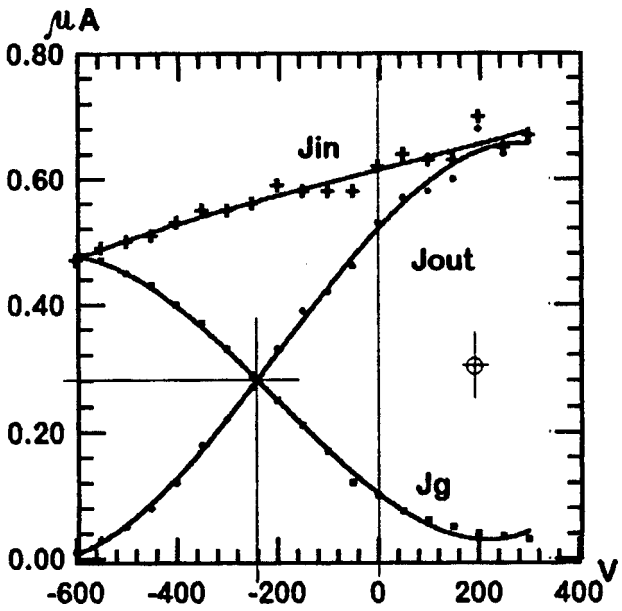

FIG. 1. Input current (I_{in}), output current (I_{out}), and grid current (I_g) versus collector voltage. The onset frequency was 10 Hz and the amplitude of the pulsed voltage was 1500 V.

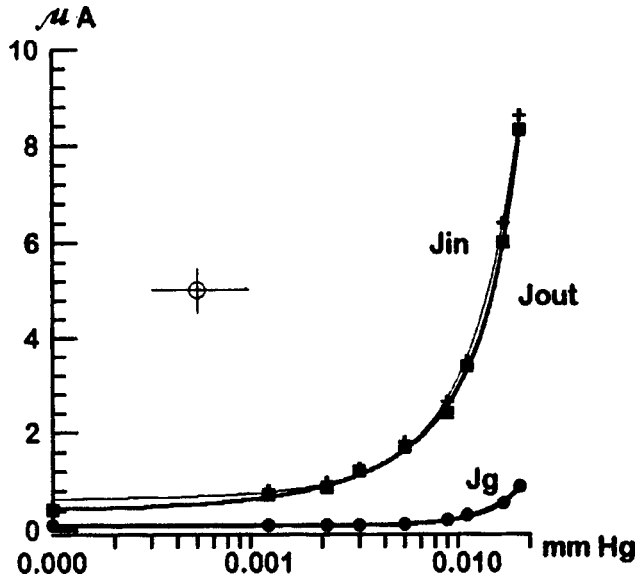

FIG. 2. Input current (I_{in}), output current (I_{out}), and grid current (I_g) versus pressure in measuring chamber. The onset frequency was 10 Hz, the collector voltage was 0 V, and the amplitude of the pulsed voltage was 1500 V.

whereas the grid current remains much lower. An increase in the residual gas pressure is accompanied by an increase in all the currents. The sharp increase in the collector current with increasing pressure is not caused by an increase in the current ion component. The same number of positive and negative charges are formed as a result of ionization of the gas. The positive ions should significantly increase the grid current, but this is not observed. The ion component of the output current is obviously relatively small. The increase of the observed currents with increasing pressure can be attributed to the anomalously strong emission as a result of the Malter effect[5,6] caused by the adsorption of positive ions of the residual gases on the surface of the ferroelectric.

The most interesting conclusion to emerge from this experiment is that the charge emitted from the surface of the ferroelectric is compensated by the current flowing through the bulk of the ferroelectric. The mechanism for this current flow has not yet been clarified, but hole conduction may play some part.

This work was supported financially by the ''Integration'' Program, Project No. 5-82.

[1] G. I. Rozenman, V. A. Okhapkin, Yu. L. Chepelev, and V. Ya. Shur, JETP Lett. **39**, 477 (1984).
[2] H. Gundel, H. Riege, J. Handerek, and K. Zioutas, CERN Report No. CERN/PS/88–66(AR), CERN, Geneva (1988).
[3] H. Gundel, J. Handerek, H. Riege *et al.*, CERN Report No. CERN/PS/89–35 (AR), CERN, Geneva (1989).
[4] I. D. Ivers, L. Schachter, I. A. Nation, G. S. Kerslick, and R. Advani, J. Appl. Phys. **73**, 60 (1993).
[5] V. I. Gaponov, Élektronika **1**, 320 (1960).
[6] D. V. Zyryanov and M. I. Elinson, Radiotekh. Élektron. **1**, No. 1 (1957).

Translated by R. M. Durham

Trapping of solvent by a C_{60} fullerene film

O. F. Pozdnyakov, B. P. Redkov, B. M. Ginzburg, and A. O. Pozdnyakov

A. F. Ioffe Physicotechnical Institute, St. Petersburg;
Institute of Problems in Mechanical Engineering, St. Petersburg
(Submitted June 5, 1998)
Pis'ma Zh. Tekh. Fiz. **24**, 23–29 (December 12, 1998)

Mass spectrometry was used over a wide temperature range to compare processes of solvent (toluene) release and desorption of C_{60} fullerene molecules from a fullerite film formed from solution on an oxidized metal substrate. It is shown that toluene is strongly retained in the fullerite film and that it is almost impossible to remove the toluene from the film without damaging its structure. Quantitative characteristics of the toluene retention and trapping effect are determined. © *1998 American Institute of Physics.* [S1063-7850(98)00512-6]

Polymer–fullerene composites are attracting close attention among researchers because fullerenes have proved to be an active modifier of the thermal,[1–3] mechanical,[4–6] and optical[7,8] properties of polymers. Thin-film polymer–fullerene composite structures are usually deposited on a substrate from suitable solutions. The planar centrifugation and deposition versions of the solution method, for example, can produce thin homogeneous polymer coatings for various purposes which satisfy the requirements of microelectronics. Thus, accurate allowance must be made for the role of the solvent in the formation of the structure of ultrathin composite films.

In studies of the thermal stability of thin, C_{60}-fullerene-filled polymer films, attention was drawn to the fact that toluene is retained in the composite film up to temperatures at which it is completely destroyed. In order to identify the reason for this toluene behavior, we also studied layers of C_{60} deposited on a substrate from solution as a model system.[2] The result of these investigations of the thermal stability of single-layer and polylayer C_{60} structures should provide a quantitative description of solvent retention and trapping by the fullerite film.

A 1.1 mg/1 ml solution of C_{60} in toluene[1)] was deposited on the surface of an oxidized tantalum foil substrate holder using a microsyringe [the room-temperature solubility of C_{60} in toluene is 2.9 mg/ml (Ref. 9)]. A 10 μl droplet of solution flowed over the surface, occupying an area of ~ 0.5 cm^2, which corresponds to a fullerite layer with a calculated weighted-mean thickness of 100 ML (1 ML$=\sim 2\times 10^{14}$ cm^{-2}). The solvent continued to evaporate in air for a few minutes. After drying, the substrate with the film was placed in the vacuum chamber of an upgraded MX-1320 mass spectrometer. When a vacuum of order 10^{-4} Pa was reached in the chamber, the sample was heated linearly at a rate of 5 K/s. The kinetics of the release of residual toluene molecules was recorded from the intensity of the J_{92} mass spectral line, which corresponds to a molecular ion ($M^+ = 92$ u).

Figure 1a shows typical kinetics of the release of toluene under heating. It can be seen that toluene is desorbed starting from room temperature and reaches a first, fairly broad maximum rate of desorption at $T_1^{\max}\sim 75\,^\circ$C. The desorption intensity then decreases monotonically to $\sim 350\,^\circ$C, still remaining very substantial. Above this temperature the toluene release again increases as far as $T_2^{\max}\sim 440\,^\circ$C, and then drops to the background level. A comparison between the desorption kinetics of toluene near $T_2^{\max}$ and the thermal desorption kinetics of the fullerene molecules recorded from the J_{720} line intensity, which corresponds to the mass of a C_{60}^+ ion (dashed curve in Fig. 1a), reveals that these are the same, i.e., $T^{\max}=T_2^{\max}\cong 440\,^\circ$C. This implies that in this temperature range the release of toluene is caused by sublimation of C_{60}. Since the release of toluene near 75 °C is evidently caused by thermally stimulated desorption of molecules from the solvation sheath, retained despite the high vacuum (so-called bound solvent), the delay in its release up to fullerene sublimation temperatures must be caused by trapping of solvent molecules by the structure of the fullerite film. Thus, the high-temperature release of toluene takes place only as a result of damage to the film structure.

Trapping of the growth medium by a growing single crystal is a common phenomenon and is observed during crystal growth in ultrahigh vacuum (carbon trapping) and especially in solution. Intercalation in various layered crystals or some inert gases in fullerite is a well-known effect.[10] The trapping scales depend on many factors, among them the growth rate of the single crystal.[11] In our case, the kinetics of the toluene release not only indicates that solvent impurities are present in the C_{60} film but also, as we shall show subsequently, serves as a source of new information on the specific characteristics of toluene–fullerene interaction in the solid phase and on other characteristics of this system.

By calibrating the sensitivity of the mass spectrometer,[12] we were able to make some quantitative estimates of the retention and trapping of toluene molecules. For our conditions the total number, i.e., the sum of the numbers of retained (desorbed before the onset of C_{60} sublimation) and trapped (released in the course of sublimation) toluene molecules is 4×10^{15} molecules per $\sim 4.5\times 10^{15}$ C_{60} molecules in the polylayer, i.e., is close to a 1:1 ratio. The quantity of

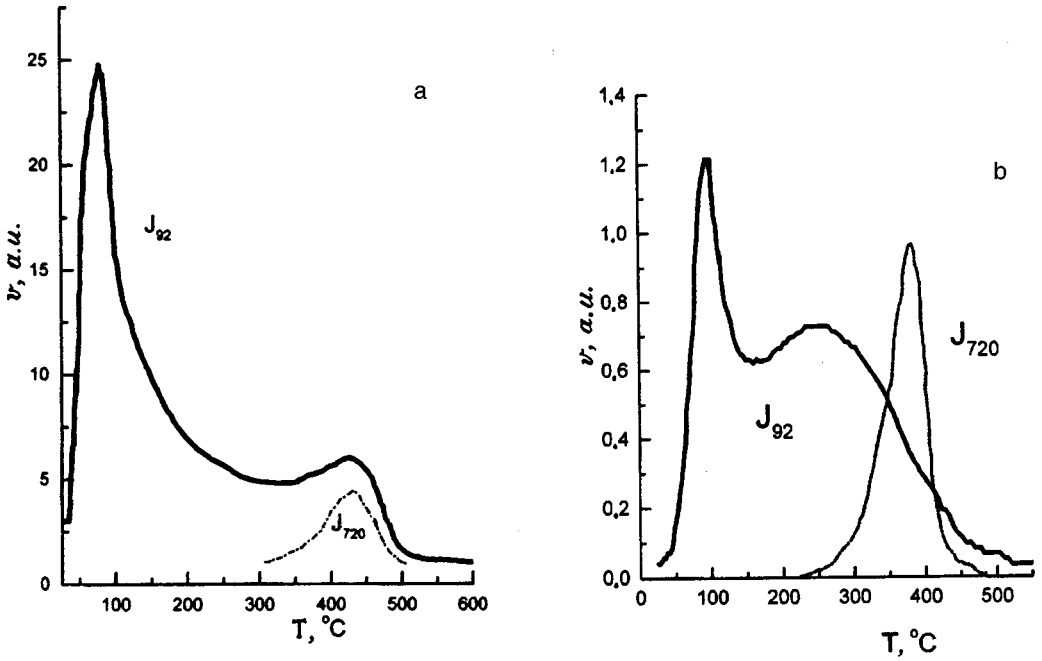

FIG. 1. Temperature dependence of the rate of toluene release J_{92} and fullerene release J_{720} from polylayer (a) and monolayer (b) coatings.

trapped toluene is 7.5 mol.% of the total recorded amount, or 3×10^{14} molecules. This means that one solvent molecule is ''embedded'' in approximately fifteen C_{60} molecules. Figure 1b shows the kinetics of toluene release from a fullerene monolayer obtained by depositing 10 μl of a one hundred times diluted initial C_{60} solution on a substrate. The sublimation kinetics of this C_{60} is also shown by the dashed curve. It can be seen that no toluene desorption peak is observed near $T_2^{\max}$ (440 °C). The other characteristics of the kinetics are similar to the polylayer experiments.

The activation energy E_{act} for desorption of C_{60} from the monolayer determined using the Arrhenius equation is 82 ± 2 kJ/mol and that for the polylayer is $E_{\text{act}}\cong105$ kJ/mol. An estimate of E_{act} for desorption of toluene from the solvate layer near 75 °C gives a value of a few (13–15) kJ/mol, i.e., close to the heat of evaporation of toluene in this temperature range.

Experiments were also carried out to record the release of toluene when the sample was heated in the chamber of the mass spectrometer by two procedures: (1) incomplete heating to $T_1\{180\,^\circ\text{C}\}$ (curve a), holding at T_1 for 1 min, and cooling to room temperature (curve a′), and (2) repeated complete heating of the sample. The results plotted in Fig. 2 suggest that there is a broad spectrum of toluene states in the fullerite film, since preliminary heating only removes specific states and does not affect those higher up the temperature scale.

The shape of the curve can be altered particularly by adding a solution of large organic molecules or macromolecules to the initial fullerene solution. The addition of macromolecules alters the kinetic desorption curve of the solvent (Fig. 3). It can be seen from the figure that the addition of macromolecules to the system (in this case polycyanurate prepolymer) causes a sharp drop in the toluene retained and trapped in a composite film sample. In other words, the presence of macromolecules alters the formation conditions of the fullerite film and thus the structure and adsorption properties.

Note that the structure of a composite film also inherently contains solvent molecules because of the presence of fullerene. Moreover, the kinetic curves of the solvent release indicate the fullerene state in this composite film for the given preparation conditions. For example, if the toluene release and the evaporation of fullerene molecules from the film have similar slopes, this implies that the fullerene in the polymer is in the form of clusters or microcrystallites with trapped solvent molecules. The absence of any toluene release from the composite film in the $\sim$440 °C range serves

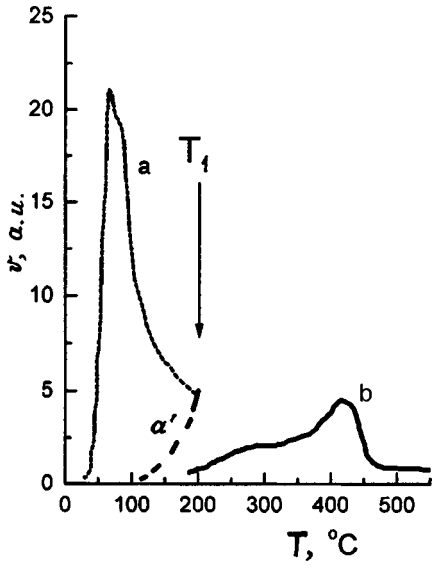

FIG. 2. Kinetics of toluene release from a polylayer during (a) preliminary heating to 180 °C and (b) repeated complete heating.

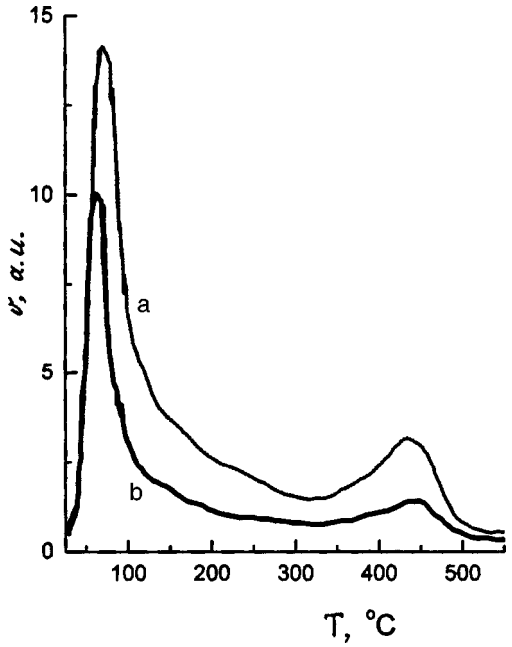

FIG. 3. Comparison of the kinetics of toluene release: a — from a C_{60} polylayer and b — from a composite film containing the same quantity of fullerene and polycyanurate macromolecules (molar ratio ~10:1).

to indicate that the fullerene has a molecularly disperse distribution in the polymer.

To sum up, we have studied the retention and trapping of solvent by a fullerite film and we have demonstrated that macromolecules have a dispersing effect on the structure of the fullerite film. We have determined the energy characteristics of the thermal dissociation of the films and the quantitative parameters of the retention and trapping effect.

This work was carried out as part of the program of the St. Petersburg Scientific Center of the Russian Academy of Sciences (Project No. 13).

[1)]The C_{60} fullerene (>99 wt.%) was synthesized in an arc discharge at the Laboratory of Professor G. A. Dyuzhev, A. F. Ioffe Physicotechnical Institute, Russian Academy of Sciences.

[1] B. M. Ginzburg, A. O. Pozdnyakov, V. N. Zgonnik, O. F. Pozdnyakov, B. P. Redkov, E. Yu. Melenevskaya, and L. V. Vinogradova, Pis'ma Zh. Tekh. Fiz. **22**(4), 73 (1996) [Tech. Phys. Lett. **22**, 166 (1996)].
[2] A. O. Pozdnyakov, O. F. Pozdnyakov, B. P. Redkov, V. N. Zgonnik, E. Yu. Melenevskaya, L. V. Vinogradova, and B. M. Ginzburg, Pis'ma Zh. Tekh. Fiz. **22**(18), 57 (1996) [Tech. Phys. Lett. **22**, 759 (1996)].
[3] L. A. Shibaev, T. A. Antonova, L. V. Vinogradova, B. M. Ginzburg, V. N. Zgonnik, and E. Yu. Melenevskaya, Pis'ma Zh. Tekh. Fiz. **23**(18), 19 (1997) [Tech. Phys. Lett. **23**, 704 (1997)].
[4] H. Thomann *et al.*, European Patent No. 544,513 (2 June 1993).
[5] N. Herron and Y. Wang (Du Pont), U.S. Patent No. 5,350,794 (27 September 1994).
[6] D. D. Bartholomew, U.S. Patent No. 94–11423 (26 May 1994).
[7] N. S. Sarifitci, L. Smilowitz *et al.*, Science **258**, 1474 (1992).
[8] Y. Wang, Nature (London) **356**, 585 (1992).
[9] H. T. Beck and G. Mandi, Fullerene Sci. Technol. **5**(2), 291 (1997).
[10] G. H. Kwei, J. D. Jorgensen, J. E. Schirber, and B. Morosin, Fullerene Sci. Technol. **5**(1), 243 (1997).
[11] T. N. Okhrimenko, V. A. Kuznetsov, O. F. Pozdnyakov, and B. P. Redkov, Kristallografiya, **42**, 541 (1997) [Crystallogr. Rep. **42**, 494 (1997)].
[12] G. S. Anufriev, O. F. Pozdnyakov, and V. R. Regel', Vysokomol. Soedin. **8**, 834 (1966).

Translated by R. M. Durham

Investigation of the decay of Freon-12(14) molecules in a transverse nanosecond discharge

A. K. Shuaibov

Uzhgorod State University
(Submitted May 7, 1998)
Pis'ma Zh. Tekh. Fiz. **24**, 30–34 (December 12, 1998)

Results are presented of an investigation of the characteristics of a transverse nanosecond discharge in Freon-12 and Freon-14 (CF_2Cl_2 and CCl_4 molecules) at pressures of 1–3 kPa. The plasma radiation spectra in the range 200–600 nm and the lifetime and temporal characteristics of the Freon decay product radiation were studied. The energy cost of the decay of a CF_2Cl_2 molecule does not exceed 10–20 eV/mol which is consistent with corresponding data for a microwave discharge. This discharge is of interest for applications in systems to purify air from Freon impurities, which are the main factor responsible for the formation of the ozone holes. © *1998 American Institute of Physics.* [S1063-7850(98)00612-0]

Freon pollution of the Earth's atmosphere has recently become one of the main factors responsible for the formation of ozone holes.[1] Several types of self-sustained discharges can be used for local purification of the atmosphere. For instance, Akhvlediani *et al.*[2] and Gritsinin *et al.*[3] studied the decay of CF_2Cl_2 molecules in a high-power CO_2 laser spark and in surface and microwave discharges. Such investigations have not been made for a transverse nanosecond discharge. Studies of a Freon plasma under the conditions of a transverse nanosecond discharge are of additional interest in connection with the use of CF_2Cl_2 and CCl_4 molecules in electric-discharge excimer lasers and lamps.[4,5] In these devices they serve as halogen carriers whose decay determines the efficiency and service life of the excimer emitter.

The present paper reports investigations of the characteristics of a transverse nanosecond discharge in CF_2Cl_2 and CCl_4 at a total pressure of $\leqslant 3$ kPa. Studies were made of the plasma radiation spectra and the lifetime and temporal characteristics of the Freon decay product radiation.

A transverse nanosecond Freon discharge was ignited in an $18\times 2.2\times 0.7$ cm volume using automatic spark preionization of the 2.2 cm interelectrode gap. The discharge was ignited using a system for transferring the charge of the main capacitance $C_1=30$ nF to a peaking capacitance $C_0=9.4$ nF. The switch was a TGII 1000/25 hydrogen thyratron. The plasma radiation was analyzed using an MDR-2 monochromator with a 1200 lines/mm diffraction grating, a Foton photomultiplier, a 14-FS linear electron multiplier, and a 6LOR-04 oscilloscope. The system used to excite the discharge and record the plasma characteristics was described in more detail by Shubainov *et al.*[6] and Shuaibov

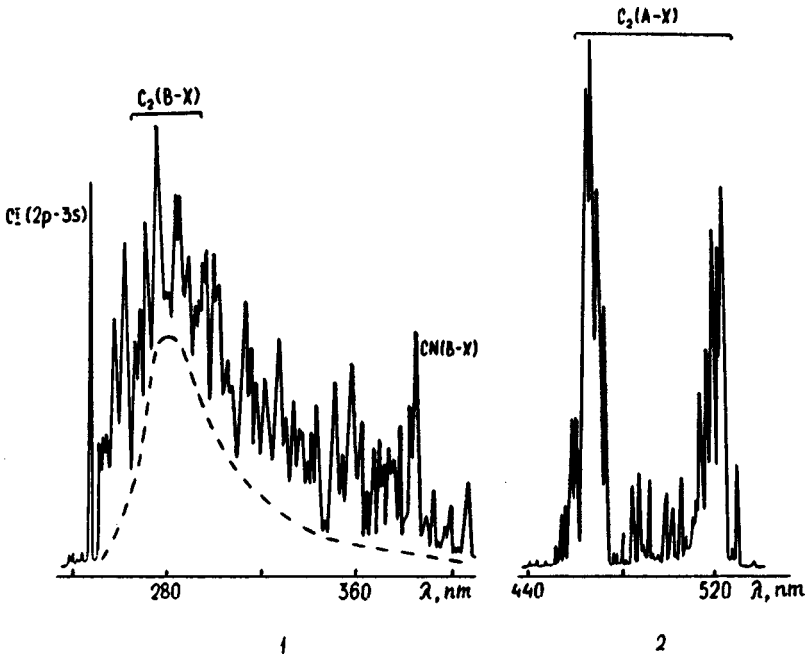

FIG. 1. Plasma radiation spectra of a transverse nanosecond discharge in Freon-12 and Freon-14 at $P=1.2$ kPa.

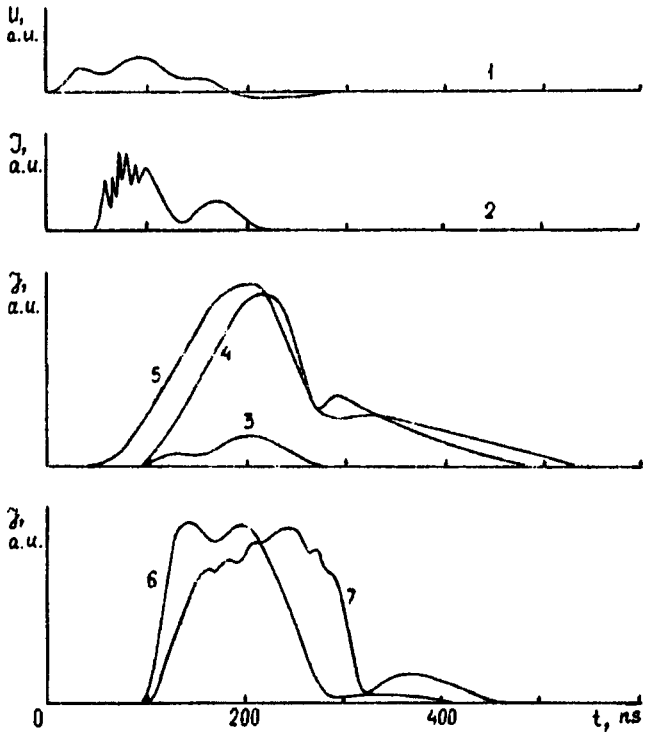

FIG. 2. Oscilloscope traces of voltage (*1*), current (*2*), and radiation (*3–7*) for a Freon-14 discharge at $P=1.2$ kPa and $U=12$ kV: *3* — 247.9 Cl ($2p-3s$), *4* — 466.9 C_2 (A–X)(6–5), *5* — 516.5 C_2 (A–X)(0–0), *6* — 337.1 N_2 (C–B)(0–0), and *7* — 388.3 nm CN (B–X)(0–0).

et al.[7] The energy input to the discharge was 0.1–0.5 J/cm^3. When the Freon-12 content was low ($P\leqslant 0.5$ kPa) and $U=5$–12 kV a homogeneous green discharge was ignited, which became contracted at $U\geqslant 12$ kV to form a dense set of thin luminous filaments uniformly filling a large part of the discharge volume. When the Freon-12 pressure was increased, the discharge near the anode consisted of a dense set of short green flashes, but a homogeneous blue discharge burnt in most of the interelectrode gap. Here we shall pay particular attention to the study of transverse nanosecond discharges at elevated Freon densities.

Typical plasma radiation spectra of a transverse nanosecond discharge are shown in Fig. 1. In the ultraviolet we observed a high-intensity 247.9 nm CI($2p-3s$) line and the N_2(C–B) and CN(B–X) bands, while C_2(A–X) Swan bands were identified in the visible. A broad band with a maximum at 280–300 nm is typical of CF_2Cl_2 molecules. A similar band, the CI line, and C_2(A–X) bands were observed in the plasma radiation spectra of a microwave discharge.[2,3] After 10^3–10^4 transverse nanosecond discharge pulses, the amplitude and width of this band decreased, which may serve as an indicator of the rate of decay of the CF_2Cl_2 molecules. The radiation spectra of the CCl_4 discharge do not contain a similar broad band with a maximum at 470 nm which is observed in a dc discharge at low CCl_4 pressure ($P\leqslant 0.05$ kPa) (Ref. 8). This indicates that the CCl_4 molecules decay completely and very efficiently in a transverse nanosecond discharge, since the appearance of the $\lambda_{max}=470$ nm band is attributed to the excitation of CCl_4 decay products, CCl_3 and C_2Cl_4. Similar decay products of CF_2Cl_2 molecules may be responsible for the appearance of the $\lambda_{max}=280-300$ nm band in the spectrum (*1*) (Fig. 1).

Measurements of the brightness of this band as a function of the number of discharge pulses showed that it reaches $0.5I_{max}$ after 4×10^3 pulses. This number of pulses approximately corresponds to the decay of all the Freon-12 molecules in the discharge chamber or their conversion to other compounds. At pressure 1.2 kPa and $n=5\times 10^3$ pulses (taking into account the specific input energy to the plasma and the passive volume of the discharge chamber), the energy consumption for the decay of a Freon-12 molecule is 10–20 eV/mol, which is almost the same as that for a microwave discharge.[2]

Figure 2 gives oscilloscope traces of the voltage, current, and plasma radiation of a transverse nanosecond discharge. A characteristic feature of Freon discharges is that during the entire energy input to the medium the intensity at the electrodes is appreciable, which is similar to an Ne/SF_6 discharge with prebreakdown ionization multiplication of the electrons.[9] The radiation on the C_2(A–X) and CN(B–X) transition increases smoothly and reaches a maximum when the voltage is completely removed from the interelectrode gap. This indicates that recombination population mechanisms are present or that C_2^* and CN* molecules are formed in reactions involving excited carbon atoms, which can be seen from the time correlation of the C_2(A–X), CN(B–X), and CI($2p-3s$) radiation (Fig. 2).

The radiation attributable to transitions of the nitrogen molecule (present in small quantities in the residual gas) had an oscilloscope trace with two peaks shifted relative to the pump current peaks. This is caused by the collisional mechanisms for population of N_2(C) under our experimental conditions.

To sum up, an investigation of a transverse nanosecond discharge in Freons has shown that at $P=0.5$–3 kPa, this is a spatially homogeneous discharge similar to that with prebreakdown ionization multiplication of the electrons. The CF_2Cl_2 molecules decay within $\leqslant 5\times 10^3$ pulses with specific energy consumptions of 10–20 eV/mol, which are the same as those in a microwave discharge.

[1] G. A. Askaryan, G. M. Batanov, S. I. Gritsinin *et al.*, Zh. Tekh. Fiz. **66**(3), 19 (1996) [Tech. Phys. **41**, 239 (1996)].
[2] Z. G. Akhvlediani, E. M. Barkhudarov, G. V. Gelashvili *et al.*, Fiz. Plazmy **22**, 470 (1996) [Plasma Phys. Rep. **22**, 428 (1996)].
[3] S. I. Gritsinin, S. I. Kossyĭ, M. A. Misakyan *et al.*, Fiz. Plazmy **23**, 264 (1997) [Plasma Phys. Rep. **23**, 242 (1997)].
[4] M. N. Kostin, V. F. Tarasenko, and A. I. Fedorov, Zh. Tekh. Fiz. **50**, 1227 (1980) [Sov. Phys. Tech. Phys. **25**, 704 (1980)].
[5] A. Luches, V. Nassisi, and M. R. Perrone, Opt. Commun. **51**(5), 315 (1984).
[6] A. K. Shubainov, Yu. Yu. Neĭmet, A. I. Khodanich, and V. S. Shevera, Opt. Spektrosk. **75**, 713 (1993) [Opt. Spectrosc. **75**, 422 (1993)].
[7] A. K. Shuaibov, L. L. Shimon, A. I. Dashchenko, and A. I. Minya, Ukr. Fiz. Zh. **43**(1), 27 (1998).
[8] Yu. S. Kravchenko, V. S. Osadchuk, A. F. Sergienko *et al.*, Teplofiz. Vys. Temp. **25**(1), 151 (1987).
[9] A. K. Shuaibov, Pis'ma Zh. Tekh. Fiz. **24**(1), 85 (1998) [Tech. Phys. Lett. **24**, 38 (1998)].

Translated by R. M. Durham

Selective infrared multiphoton dissociation of CF_3I molecules in a pulsed gasdynamic stream: Dependence of the ^{13}C enrichment factor in the C_2F_6 product on the molecular concentration in the beam

G. N. Makarov

Institute of Spectroscopy, Russian Academy of Sciences, Troitsk
(Submitted June 17, 1998)
Pis'ma Zh. Tekh. Fiz. **24**, 35–40 (December 12, 1998)

An investigation was made of isotopically selective infrared multiphoton dissociation of CF_3I molecules in a pulsed gasdynamic stream. It was observed that the ^{13}C enrichment factor in the C_2F_6 product depends strongly on the molecular concentration in the stream. Reasons for this result are discussed. © *1998 American Institute of Physics.* [S1063-7850(98)00712-5]

Highly selective laser separation of isotopes of heavy elements (U, Os, W, . . .) by infrared multiphoton dissociation of UF_6, OsO_4, WF_6, . . . molecules[1] can only be achieved when the molecules are highly cooled in gasdynamic jets or streams.[2,3] This is because of the small isotope shift in the infrared absorption spectra of these molecules ($\Delta\nu_{is} \leqslant 1\ cm^{-1}$). However, when gasdynamic jets and streams are used, collection of the products presents major problems. Previously,[4,5] in order to understand the processes accompanying the infrared multiphoton dissociation of molecules in gasdynamic jets and flows, and also to develop a method of obtaining and efficiently collecting products enriched in the desired isotope, we investigated the dissociation of CF_3I in a pulsed beam. This molecule was selected because the infrared multiphoton excitation and dissociation of CF_3I has been fairly well studied,[6–10] including in a molecular beam,[11] and its dissociation yields stable products (C_2F_6 and I_2). This molecule was initially considered as an initial substance for large-scale laser separation of carbon isotopes.[12] In Ref. 4 we developed an approach which can produce a highly enriched residual gas in a single irradiation cycle, while in Ref. 5 we studied the possibility of obtaining products enriched in the desired isotope (C_2F_6 and COF_2). We showed[5] that the C_2F_6 yield drops sharply with decreasing concentration of CF_3I molecules in the stream, caused by losses of CF_3 radicals to the walls of the chamber in which the molecular stream is formed. In order to reduce the losses of radicals, we suggested using a buffer (acceptor) gas in the chamber at a pressure of 3–5 mTorr. This appreciably increased the yield of products, especially when oxygen was used as the radical acceptor in the chamber. However, we did not examine the influence of concentration effects on the enrichment factor in the products.[5] Nevertheless, the enrichment factor, together with the yield of the desired product, is an important parameter of the separation process.[13] The present study examines how the concentration of CF_3I molecules in the stream affects the ^{13}C enrichment factor of the C_2F_6 product.

The experimental setup, measurement technique, and procedure for collecting and analyzing the products and the residual gas were described in detail in Refs. 4 and 5. Briefly, we used a pulsed ''current loop'' nozzle[14,15] with a nozzle opening pulse of half-height duration $\tau_{nozzle} \cong 150\ \mu s$. The vacuum chamber in which the molecular beam was formed had a volume $V_{ch} \cong 20$ l and was evacuated to $\cong 10^{-5}$ Torr using a turbomolecular pump. The stream was formed using two thin (100 μm) metal strips attached to the wall of the nozzle. The molecules were excited by a TEA CO_2 laser pulse. During irradiation of the molecules in the stream, the main evacuation channel of the vacuum chamber was closed. The products and residual CF_3I gas formed after irradiation were collected in a cryogenic trap connected to the chamber. After the end of the irradiation cycle, the gas from the trap was collected in an optical cell for infrared and mass analysis.

The ^{13}C enrichment factor K_{13}^{prod} of the C_2F_6 was investigated as a function of the total number n_{fl} of molecules in the stream and also as a function of the time delay t_{del} between the nozzle pulse and the exciting laser pulse. The enrichment factor was defined as

$$K_{13}^{prod} = (2I_{121} + I_{120})/(I_{120} + 2I_{119})\xi, \quad (1)$$

where I_{121}, I_{120}, and I_{119} are the intensities of the mass peaks of the $C_2F_5^+$ ion, and $\xi = {}^{13}C/{}^{12}C \cong 0.011$ is the ratio of the percent content of carbon isotopes in the initial CF_3I gas. The number n_{fl} of molecules in the beam was determined from the pressure increment Δp in the vacuum chamber after n nozzle pulses with the pumping shut off,

$$n_{fl} = (p_{fin} - p_{in})V_{ch}/nkT = \Delta p V_{ch}/nkT \quad (Y \cong 300\ K), \quad (2)$$

and also from the infrared absorption spectrum of the CF_3I molecules collected from the vacuum chamber in the optical cell after n nozzle pulses. Since the pulsed beam was spatially bounded and had a fixed volume[5] ($V_{fl} \cong 50\ cm^3$), changes in n_{fl} and t_{del} altered the concentration of irradiated molecules in the stream and henced that of product CF_3 radicals.

Figure 1 shows the dependence $K_{13}^{prod}(n_{fl})$. The molecules were irradiated at the frequency 1043.16 cm^{-1} (9P(24) laser line) in resonance with the ν_1 $^{13}CF_3I$ vibration.[16] This was the frequency at which the maximum enrichment factor of the C_2F_6 product was observed.[5] Also plotted is the

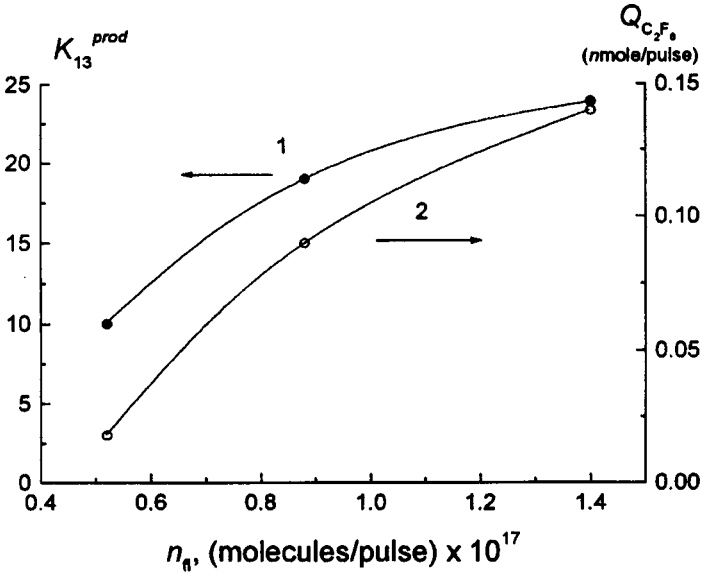

FIG. 1. Dependence of the ^{13}C enrichment factor of C_2F_6 (*1*) and the C_2F_6 yield (*2*) on the total number of CF_3I molecules in the stream, n_{fl}. The molecules were irradiated at a frequency of 1043.16 cm^{-1} (9P (24) laser line) and energy density $\Phi=1.6$ J/cm^2. The time delay between the nozzle pulse and the exciting laser pulse was $t_{del}=250$ μs.

C_2F_6 yield as a function of n_{fl}, $Q_{C_2F_6}(n_{fl})$. It can be seen that as n_{fl} decreases, not only the yield but also K_{13}^{prod} decrease. For instance, when n_{fl} decreases from $\cong 1.4\times 10^{17}$ molecules/pulse to $\cong 5.2\times 10^{16}$ molecules/pulse, K_{13}^{prod} decreases from $\cong 25$ to $\cong 10$. Figure 2 shows the dependence $K_{13}^{prod}(t_{del})$. Also plotted for comparison is the curve $Q_{C_2F_6}(t_{del})$, obtained for excitation of $^{12}CF_3I$ molecules at the frequency 1071.9 cm^{-1} (9R(10) laser line)[5] which characterizes the time evolution of the molecular flux intensity. It can be seen that K_{13}^{prod} decreases fairly substantially as t_{del} increases and decreases relative to the value $t_{del}\cong 280$ μs for which the highest-intensity part of the molecular flow was irradiated. Thus, this result reemphasizes that K_{13}^{prod} decreases substantially as the concentration of product CF_3 radicals in the flow decreases.

In the author's view, the decrease in K_{13}^{prod} with decreasing concentration of irradiated CF_3I molecules in the stream is caused by losses of CF_3 radicals to the chamber walls. A possible mechanism for the loss of radicals is the reaction

$$CF_3+I_2\rightarrow CF_3I+I. \quad (3)$$

It has already been shown[5] that as the concentration of product CF_3 radicals decreases, an increasing relative fraction is lost to the walls without forming C_2F_6. Since the dissociation selectivity in these experiments was lower than the ratio of the ^{12}C and ^{13}C isotope contents in the initial CF_3I gas ($\alpha_{13}<{}^{12}C/{}^{13}C$), the number of product $^{13}CF_3$ radicals was always less than the number of $^{12}CF_3$ radicals, and thus a relatively large fraction of the $^{13}CF_3$ radicals was lost to the walls. This led to a decrease in K_{13}^{prod} as the concentration of irradiated molecules in the stream decreased.

To conclude, it has been shown that the ^{13}C enrichment factor of C_2F_6, K_{13}^{prod} falls sharply as the concentration of CF_3I molecules in the beam decrease. The decrease in K_{13}^{prod} is caused by losses of CF_3 radicals to the walls of the chamber in which the molecular beam is formed. Thus, in order to obtain ^{13}C enriched products, the stream must contain a comparatively high concentration of $^{13}CF_3$ radicals ($N\geqslant 10^{13}$

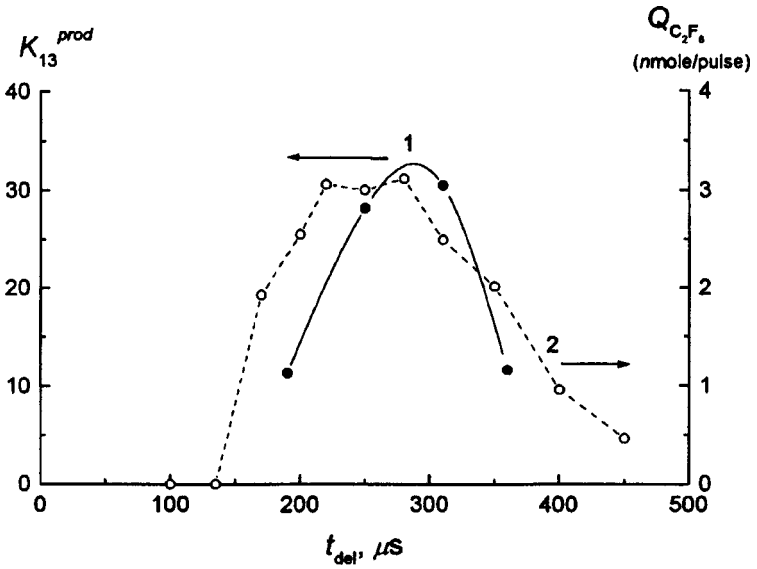

FIG. 2. Dependence of the ^{13}C enrichment factor of C_2F_6 on the time delay t_{del} between the nozzle pulse and the exciting laser pulse (*1*). The CF_3I molecules were irradiated at a frequency of 1043.16 cm^{-1} (9P (24) laser line) and energy density $\Phi=1.6$ J/cm^2 and the CF_3I pressure above the nozzle was 2 bar. Also plotted for comparison is the C_2F_6 yield versus t_{del} (*2*) obtained when the molecules were irradiated at a frequency of 1071.9 cm^{-1} (9R (10) laser line) and energy density $\Phi=3$ J/cm^2 and the CF_3I pressure above the nozzle was 4 bar.

cm^{-3}) and/or a radical acceptor such as O_2 must be used in the chamber.

The author would like to thank V. N. Lokhman, D. E. Malinovskiĭ, and D. D. Ogurok for technical assistance. The work was supported financially by the Russian Fund for Fundamental Research, Grant No. 96-02-16421-a.

[1] V. N. Bagratashvili, V. S. Letokhov, A. A. Makarov, and E. A. Ryabov, *Multiple Photon Infrared Laser Photophysics and Photochemistry* (Gordon and Breach, New York), 512 pp.
[2] J. B. Anderson, in *Gasdynamics, Molecular Beams and Low Density Gas Dynamics*, Vol. 4, edited by P. P. Wegener (Marcel Dekker, New York, 1974), p. 1.
[3] G. N. Makarov, E. Ronander, Van S. P. Heerden, M. Gouws, and K. Van der Merwe, Appl. Phys. B **65**, 583 (1997).
[4] G. N. Makarov, D. E. Malinovskiĭ, and D. D. Ogurok, Zh. Tekh. Fiz. (in press).
[5] G. N. Makarov, V. N. Lokhman, D. E. Malinovskiĭ, and D. D. Ogurok, Kvant. Elektron. (Moscow) **25**, No. 6 (1998).
[6] S. Bittenson and P. L. Houston, J. Chem. Phys. **67**, 4819 (1977).
[7] M. Drouin, M. Gauthier, R. Pilson, and P. Hackett, Chin. Phys. Lasers **60**, 16 (1978).
[8] M. Gauthier, P. A. Hackett, and C. Willis, Chem. Phys. **45**, 39 (1980).
[9] V. N. Bagratashvili, V. S. Doljikov, V. S. Letohov, and E. A. Ryabov, Appl. Phys. **20**, 231 (1979).
[10] V. N. Bagratashvili, V. S. Dolzhikov, V. S. Letokhov, A. A. Makarov, E. A. Ryabov, and V. V. Tyakht, Zh. Éksp. Teor. Fiz. **77**, 2238 (1979) [Sov. Phys. JETP **50**, 1075 (1979)].
[11] V. M. Apatin and G. N. Makarov, Kvantovaya Élektron. (Moscow) **10**, 1435 (1983) [Sov. J. Quantum Electron. **13**, 932 (1983)].
[12] G. I. Abdushelishvili, O. N. Avotkov, V. N. Bagratashvili *et al.*, Kvant. Élektron. (Moscow) **9**, 743 (1982) [Sov. J. Quantum Electron. **12**, 459 (1982)].
[13] V. N. Lokhman, G. N. Makarov, E. A. Ryabov, and M. V. Sotnikov, Kvant. Elektron. (Moscow) **22**, 633 (1995).
[14] G. I. Dimov, Prib. Tekh. Eksp. **5**, 168 (1968).
[15] W. R. Gentry and C. F. Giese, Rev. Sci. Instrum. **49**, 595 (1978).
[16] W. Fuss, Spectrochim. Acta A **38**, 829 (1982).

Translated by R. M. Durham

Formation of heterogeneous molecules at the surface of metals in a mixture of protium and deuterium gases

A. A. Pisarev, P. O. Kokurin, and Yu. V. Borisyuk

Moscow Engineering-Physics Institute
(Submitted June 8, 1998)
Pis'ma Zh. Tekh. Fiz. **24**, 41–44 (December 12, 1998)

An investigation was made of the formation of molecules of mixed hydrogen isotopes at the surface of tungsten. An original method is proposed to determine the chemisorption activation energy from the rate of desorption of heterogeneous molecules. [S1063-7850(98)00812-X]

The behavior of hydrogen in a solid is of interest for many technological applications, including nuclear fusion and hydrogen power engineering. Work with any two hydrogen isotopes at the same time is frequently accompanied by isotopic mixing and this may cause various problems when analyzing the dynamics of sorption and desorption processes. For instance, the formation of HD molecules was observed[1–8] when solids were bombarded with deuterium ions, deuterium plasma, and epithermal atoms.

Here we study the formation of HD molecules as a result of interaction between a metal (in this case tungsten) and gaseous hydrogen in a mixture of H_2 and D_2 gases.

The experiments were carried out in an oil-free vacuum with a high H_2 content and controlled admission of a small quantity of D_2. The HD partial pressure was measured using a high-sensitivity magnetic mass spectrometer.

We observed experimentally that as the temperature of the tungsten increased, the HD signal measured in the vacuum chamber around the sample also increased. Figure 1 gives logarithms of the HD signal as a function of the reciprocal temperature for the same sample but with different prehistories. The first series was carried out using a sample which had been heated to 1500 K before the measurements. In the second series the sample had been held in a low vacuum with a mixture of H_2 and D_2 gases at a higher pressure, and in the third series the sample had been annealed following the first two series. It can be seen that quantity of product HD depends on the preparation of the sample, including the heat treatment and the vacuum conditions. This may indicate that the surface state influences the isotopic mixing. Thus, it may be predicted that in experiments where the main quantity being measured is the desorption rate (experiments to study ion implantation, recycling, permeability, thermal desorption, and so on), the contribution of isotopic mixing may vary from one experiment to another and this may create difficulties when interpreting the experimental data, as was discussed by Pisarev *et al.*[7] in particular.

The experiments can be described using a model based on an approach adopted by Pisarev *et al.*[9] to describe the buildup of gas at the surface and in the bulk of a solid. Simplifying this model for our particular problem, we shall assume that under the experimental conditions, equilibrium is established at the metal surface between the particle flux from the gas to the chemisorbed state at the surface and desorption from it and also between the particle fluxes from the surface into the bulk of the solid and in the opposite direction. We shall also assume that the degree of coverage of the surface is low. In this case, the balance of the deuterium and protium atom fluxes can be written as follows:

$$kI_{0\mathrm{D}}=Kc_{\mathrm{D}}^2+\frac{1}{2}Kc_{\mathrm{H}}c_{\mathrm{D}},$$

$$kI_{0\mathrm{H}}=Kc_{\mathrm{H}}^2+\frac{1}{2}Kc_{\mathrm{H}}c_{\mathrm{D}}.$$

Here the terms on the left-hand side refer to the deuterium and protium atom fluxes from the gas to the surface, where I_0 are the molecular fluxes from the gas and k is the coefficient of molecular dissociation. The right-hand sides refer to the fluxes of desorbed HD, H_2, and D_2 molecules, where c_{H} and c_{D} are the concentrations of H and D atoms at the surface and K is the coefficient of recombination of the atoms to form a molecule.

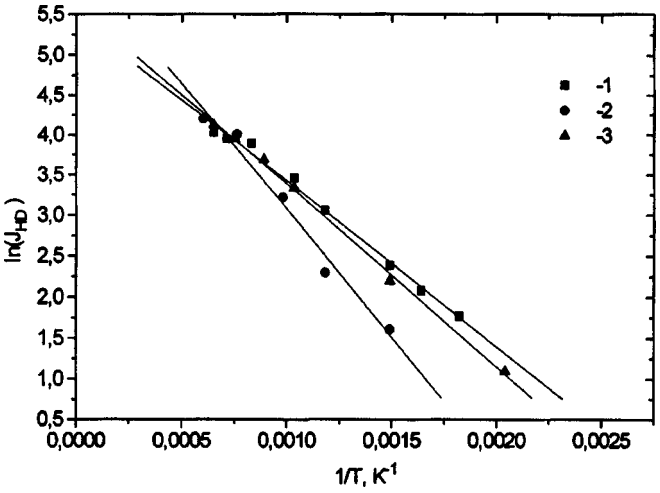

FIG. 1.

After performing some simple calculations assuming that the residual hydrogen pressure is much higher than the residual deuterium pressure $I_{0H} \gg I_{0D}$ and using for k the formula

$$k(T) = k_0 \exp(-2E_c/kT),$$

where E_c is the activation energy for dissociative chemisorption, we obtain an expression for the HD molecular flux:

$$J_{HD} = (k_0 I_{0D}^2/128 I_{0H}) \exp(-E_c/kT).$$

Figure 1 shows that the experimental data can be accurately described by exponential dependences from which E_c can be determined.

It was found that in the experiment using the barely heated sample the activation energy was $E_c = 0.092$ eV (not shown in the figure), but after the sample had been heated to high temperatures and the surface had therefore been cleaned, the value of E_c decreases slightly to $E_c = 0.088$ eV (series 2 in Fig. 1). Then, after secondary contamination of the sample with impurities E_c increases to $E_c = 0.135$ eV (series 2) but after repeated heating, it returns to a level close to the initial value $E_c = 0.096$ eV (series 3). This behavior of E_c is consistent with ideas on the activation and passivation of the surface.

This procedure to determine E_c can easily be applied in experiments to study the interaction of gas, epithermal atoms, fast ions, and plasma with solids, to calculate the coefficient of recombination of atoms to form molecules under specific experimental conditions.

This work was supported by the Russian Fund for Fundamental Research (Grant No. 96-02-18706).

[1] M. Braun and B. Emmoth, J. Nucl. Mater. **128**, 657 (1984).
[2] K. L. Wilson and W. L. Hsu, J. Nucl. Mater. **145**, 121 (1987).
[3] C. R. Longhurst, R. A. Anderl, and D. A. Struttman, J. Nucl. Mater. **141**, 229 (1986).
[4] R. G. Macaulay-Newcombe and D. A. Thompson, J. Nucl. Mater. **212**, 942 (1994).
[5] S. Chiu and A. A. Haasz, J. Nucl. Mater. **210**, 34 (1994).
[6] Ph. Cetier, J. Charuau, Y. Belot *et al.*, Fusion Technol. **28**, 1148 (1995).
[7] A. A. Pisarev, A. V. Varava, and S. K. Zhdanov, J. Nucl. Mater. **220**, 926 (1995).
[8] G. Eilmsteiner, W. Walkner, and A. Winkler, Surf. Sci. **352**, 263 (1996).
[9] A. A. Pisarev and O. V. Ogorodnikova, J. Nucl. Mater. **248**, 52 (1997).

Translated by R. M. Durham

Critical fields in easy-axis antiferromagnetics with allowance for Dzyaloshinskiĭ interaction and uniaxial pressure

G. K. Chepurnykh, V. S. Ivaniĭ, M. I. Kolesnik, and O. G. Medvedovskaya

Institute of Applied Physics, National Academy of Ukraine, Sumy;
A. S. Makarenko State Pedagogical Institute, Sumy
(Submitted June 17, 1997; resubmitted March 25, 1998)
Pis'ma Zh. Tekh. Fiz. **24**, 45–51 (December 12, 1998)

The easy-axis antiferromagnetic α-Fe_2O_3 is used to study the influence of uniaxial pressure on the magnetic phase diagrams. It is shown that there are regions where an abrupt and appreciable change in the magnetization is accompanied not only by a negligible change in the external magnetic field but also by a change in the uniaxial pressure. Thus, the situation usually achieved in magnetically soft materials arises, except that in this case it is controllable.
 [S1063-7850(98)00912-4]

The properties[1–4] of magnetoelastic interaction in antiferromagnetics which show up most clearly near orientational phase transitions have been studied on many occasions (see, for example, Refs. 5 and 6). Assuming that near orientational phase transitions an abrupt and appreciable change in magnetization may accompany not only a change in the magnetic field[6] but also changes in the uniaxial pressure (which is required to produce magnetostrictive transducers[8]), we shall analyze the influence of uniaxial pressure (perpendicular to the easy axis) on the magnetic phase diagrams for the easy-axis antiferromagnetic α-Fe_2O_3.

We shall take the thermodynamic potential in the form[5]

$$F=F_m+F_{ms}+F_s, \tag{1}$$

where the magnetic component F_m is given by

$$F_m=2M_0\left[\frac{E}{2}\mathbf{m}^2+\frac{a_1}{2}(l_x^2+l_y^2)+\beta(m_xl_y-m_yl_x) -\frac{a_2}{4}l_z^4-\mathbf{m}H\right], \tag{1a}$$

and the magnetoelastic F_{ms} and elastic F_s components are given by

$$\begin{aligned}F_{ms}=\int\{&\lambda_1(U_{xx}+U_{yy})l_z^2+\lambda_2U_{zz}l_z^2\\&+\lambda_3[4l_xl_yU_{xy}+(l_x^2-l_y^2)(U_{xx}-U_{yy})]\\&+\lambda_4[2l_xl_yU_{xz}+(l_x^2-l_y^2)U_{yz}]\\&+\lambda_5(l_x^2+l_y^2)(U_{xx}+U_{yy})+\lambda_6(l_x^2+l_y^2)U_{zz}\\&+\lambda_7(l_xl_zU_{xz}+l_yl_zU_{yz})\\&+\lambda_8[2l_xl_zU_{xy}+l_yl_z(U_{xx}-U_{yy})]\}\\\equiv\mathbf{l}\hat{\lambda}\mathbf{l}\hat{U},\end{aligned} \tag{1b}$$

$$\begin{aligned}F_s=\int\Big\{&\frac{1}{2}\mu_1U_{zz}^2+2\mu_2(U_{xx}+U_{yy})^2\\&+\mu_3[(U_{xx}-U_{yy})^2+4U_{xy}^2]\\&+2\mu_4(U_{xx}+U_{yy})U_{zz}+4\mu_5(U_{xz}^2+U_{yz}^2)\\&+4\mu_6[(U_{xx}-U_{yy})U_{yz}+2U_{xy}U_{xz}]+\sigma_{ij}U_{ij}\Big\}dV\\\equiv\frac{1}{2}\hat{\mu}\hat{U}\hat{U},\end{aligned} \tag{1c}$$

$$\mathbf{l}=(M_1-M_2)/2M_0, \quad \mathbf{m}=(M_1-M_2)/2M_0,$$

$$\mathbf{m}\cdot\mathbf{l}=0 \quad (T<T_M=260\ \text{K}),$$

$E\gg\beta\gg a_1\gg a_2$, and the easy axis is parallel to OZ. Minimizing the thermodynamic potential (1) as a function of U_{lk}, we obtain $\partial(F_{ms}+F_z)/\partial U_{lk}=0$. Determining U_{lk} from this equation and substituting the expressions obtained for U_{lk} into Eq. (1b), we obtain

$$F_{ms}=C_1(l_x^2-l_y^2)+C_2l_yl_z, \tag{2}$$

where

$$C_1=\frac{\lambda_4\mu_6-2\lambda_3\mu_5}{8(\mu_3\mu_5-\mu_6^2)}(\sigma_{xx}-\sigma_{yy}),$$

$$C_2=\frac{\lambda_7\mu_6-2\lambda_8\mu_5}{8(\mu_3\mu_5-\mu_6)}(\sigma_{xx}-\sigma_{yy}).$$

In formula (2) we did not write the cumbersome terms whose role reduces to renormalizing the parameters of the magnetic component of the potential (1). According to Dikshteĭn *et al.*[9] uniaxial compression of a crystal along the X axis ($\sigma_{xx}=-p$) also tends to direct the vector $\mathbf{l}$ along the X axis—see the term $C_1(\mathbf{l}_x^2-\mathbf{l}_y^2)$ in formula (2). In addition, since the region of small angles between the easy axis and H is the most interesting, uniaxial pressure in the basal plane

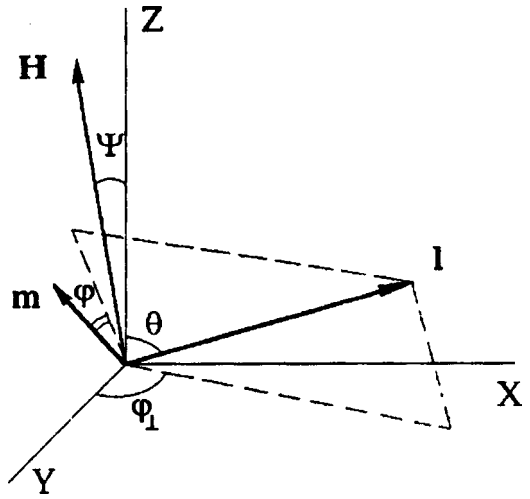

FIG. 1. Orientation of the antiferromagnetism vector **l** and the magnetization vector **m** for an arbitrary orientation of the external magnetic field in the plane *ZY*: θ and $\varphi_\perp$ are the polar and azimuthal angles of the vector **l**, φ is the angle characterizing the direction of the vector **m** in the plane perpendicular to **l** (this angle is measured from the curve of intersection of this plane with the plane passing through the *Z* axis and the vector **l**).

eliminates the uncontrollable influence of the anisotropy in this plane on the orientation of the antiferromagnetism vector **l**.

Minimizing the potential (1) as a function of the variables m, φ, $\varphi_\perp$, and θ (Fig. 1), we obtain the system of equations

$$\partial F/\partial \mathbf{m}=0, \quad \partial F/\partial \varphi=0, \quad \partial F/\partial \varphi_\perp=0, \quad \partial F/\partial \theta=0. \tag{3}$$

An analysis of the system (3) yields the conclusion that since formula (2) contains the term $C_2\mathbf{l}_y\mathbf{l}_z$, when the angle θ varies between $\pi/2$ and 0 in the field $H\|$EA, the angle $\varphi_\perp$ also varies between $\pi/2$ and 0. In the third equation of system (3) we eliminate **m** and φ, determined from the first and second equations, respectively, assuming $\varphi_\perp=\pi/2+\varphi_1$, $\theta=\pi/2-\theta_1$, and after expanding the trigonometric functions as a series allowing for the smallness of φ_1 and θ_1, we obtain

$$\varphi_1=(H_zH_y-C_2E)\left(\theta_1-\frac{\theta_1^3}{6}\right)[H_y^2+4C_1E+H_y\beta]^{-1}. \tag{4}$$

We can regard the angle θ_1 as an order parameter in the orientational phase transition being studied and we can therefore use the Landau theory of phase transitions. Thus, eliminating **m** and φ in the thermodynamic potential, expanding the trigonometric functions as a series as before, assuming that θ_1, $\varphi_1 \ll 1$, and then eliminating φ_1, we find

$$F=F_0+A\theta_1^2+B\theta_1^4, \tag{5}$$

where

$$A=H_z^2+\beta^2+H_y\beta-a_1E-(H_yH_z-C_2E)^2 \times[H_y^2+4C_1E+H_y\beta]^{-1},$$

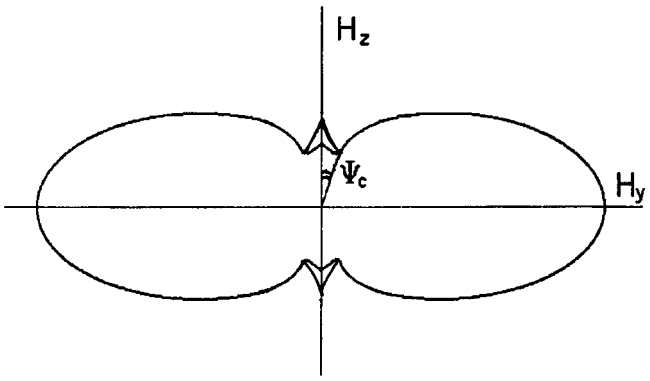

FIG. 2. Critical fields of the easy-axis antiferromagnetic $\alpha-Fe_2O_3$ with uniaxial pressure perpendicular to the easy axis.

$$B=\frac{1}{12}\Bigg[-4(H_z^2+\beta^2)-H_y\beta+4a_1E-6a_2E + \frac{2(H_zH_y-C_2E)^2(2H_y^2+5H_y\beta+8C_1E)}{(H_y^2+4C_1E+H_y\beta)^2} + \frac{3(H_yH_z-C_2E)^4H_y\beta}{(H_y^2+4C_1E+H_y\beta)^4}\Bigg].$$

The Landau theory of phase transitions indicates that for the curve of the second-order transitions and also for the critical curve of first-order transitions the coefficient A vanishes. In addition, at the point where the curve of the second-order transitions goes over to the curve of the first-order transitions (i.e., at the tricritical point), both coefficients A and B vanish. Thus, assuming

$$A=0, \tag{6}$$

we obtain a curve on the H_z, H_y diagram (Fig. 2), which for $\Psi>\Psi_c$ defines the curve of the second-order transition and for $\Psi<\Psi_c$ defines the curve of the lower field of lability. Here, Ψ_c is the critical angle between the easy axis and the direction of the field H within which the transition of the vector **l** to the X axis takes place in the form of a first-order phase transition. If the range of small angles Ψ is disregarded, we can neglect the terms which take account of the uniaxial pressure in Eq. (6) and this equation then gives

$$H_z=\pm\sqrt{aH_y^2+bH_y+H_c^2}, \tag{7}$$

where $a=-1$, $b=-(a_1E-2\beta^2)\beta^{-1}$, $H_c^2=a_1E-\beta^2$. Equation (7) defines an ellipse inside which an angular phase is achieved and outside which the phase is $\mathbf{l}\perp$ EA. At the tricritical point both Eq. (6) and the following equation are valid

$$B=0. \tag{8}$$

If the pressure is such that C_1E, $C_2E \ll \beta H_y$, Eqs. (6) and (8) yield the following expression for the critical angle:

$$\Psi_c=2a_2E[H_c\beta(1+H_c^2/\beta^2)^2]^{-1}, \tag{9}$$

and Eq. (6) gives the following relation for the lower field of lability

$$H_z^2 = H_c^2\left(1 + H_y\frac{H_c^2-\beta^2}{\beta H_c^2}\right). \quad (10)$$

If the pressure is such that C_1E, $C_2E \gg \beta H_y$, Eqs. (6) and (8) give

$$\Psi_c = 2a_2E\{H_c\beta[1+(C_2/4C_1)^2]^2\}^{-1}, \quad (11)$$

and Eq. (6) gives

$$H_z = H_c - H_y/2\{C_2/2C_1+\beta[1+(C_2/4C_1)^2]H_c^{-1}\}. \quad (12)$$

Since we have $H_c \sim \beta$, and $C_2/4C_1 \approx 5.6$ (the numerical values for the magnetoelastic λ_i and elastic μ_i constants of an α-Fe_2O_3 crystal were taken from Refs. 5 and 10), we can see by comparing expressions (9) and (11) that the uniaxial pressure reduces the critical angle by more than two orders of magnitude. Since the theory,[7] experiments,[11] and our calculations using the equations (3) indicate that because of the smallness of the critical angle Ψ_c the magnetization changes abruptly with a negligible change in the magnetic field, we thus obtain states in magnetic materials for which abrupt magnetic reversal takes place accompanying not only changes in the field but also with changes in the uniaxial pressure. That is to say, we obtain a situation usually achieved in magnetically soft materials[8,12] except that in our case, the situation is controllable. Formulas (10) and (12) indicate that for small angles Ψ the uniaxial pressure also substantially changes the magnetic phase diagram. If $H_c > \beta$, it follows from Ref. 13 and relation (10) that as the magnetic field component H_y increases the component H_z also increases, whereas as a result of the uniaxial pressure expression (12) indicates that the component H_z decreases with increasing H_y.

We note that experimental acoustic and resonance investigations near the tricritical point obtained on the phase diagram in terms of the variables H_y, H_z could help us to understand the acoustic anomaly observed in Ref. 1.

[1] A. S. Borovik-Romanov and E. G. Rudashevskiĭ, Zh. Éksp. Teor. Fiz. **47**, 2095 (1964) [Sov. Phys. JETP **20**, 1407 (1964)].
[2] S. Lida and A. Tasaki, in *Proceedings of the International Conference on Magnetism*, Nottingham, England, 1964, p. 583.
[3] I. E. Dikshteĭn, V. V. Tarasenko, and V. G. Shavrov, Zh. Éksp. Teor. Fiz. **67**, 816 (1974) [Sov. Phys. JETP **40**, 404 (1974)].
[4] G. K. Chepurnykh, Fiz. Tverd. Tela (Leningrad) **17**, 430 (1975) [Sov. Phys. Solid State **17**, 268 (1975)].
[5] V. I. Ozhogin and V. L. Preobrazhenskiĭ, Zh. Éksp. Teor. Fiz. **73**, 988 (1977) [Sov. Phys. JETP **46**, 523 (1977)].
[6] L. T. Tsymbal, A. I. Izotov, N. K. Dan'shin, and K. N. Kogaryan, Zh. Éksp. Teor. Fiz. **105**, 948 (1994) [JETP **78**, 508 (1994)].
[7] G. K. Chepupnykh, Fiz. Tverd. Tela (Leningrad) **10**, 1917 (1968) [Sov. Phys. Solid State **10**, 1517 (1968)]; M. I. Kaganov and G. K. Chepupnykh Fiz. Tverd. Tela (Leningrad) **11**, 911 (1969) [Sov. Phys. Solid State **11**, 745 (1969)].
[8] K. P. Belov, *Magnetostrictive Effects and Their Technical Applications* [in Russian], Nauka, Moscow (1987).
[9] I. E. Dikshteĭn, V. V. Tarasenko, and V. G. Shavrov, Fiz. Tverd. Tela (Leningrad) **16**, 2192 (1974) [Sov. Phys. Solid State **16**, 1432 (1975)].
[10] A. S. Borovik-Romanov, *Problems of Magnetism* [in Russian], Nauka, Moscow (1972), p. 4757.
[11] K. L. Dudko, V. V. Eremenko, and V. M. Fridman, Zh. Éksp. Teor. Fiz. **61**, 678 (1971) [Sov. Phys. JETP **34**, 362 (1972)].
[12] A. A. Preobrazhenskiĭ and E. G. Bishard, *Magnetic Materials and Elements* [in Russian], Vysshaya Shkola, Moscow (1986).
[13] V. I. Ozhogin, and V. G. Shapiro, Zh. Éksp. Teor. Fiz. **54**, 96 (1968) [Sov. Phys. JETP **27**, 54 (1968)].

Translated by R. M. Durham

Determination of the electron density in a discharge with nonmetallic liquid electrodes in atmospheric-pressure air from the absorption of microwave probe radiation

Yu. A. Barinov, V. B. Kaplan, V. V. Rozhdestvenskiĭ, and S. M. Shkol'nik

A. F. Ioffe Physicotechnical Institute, Russian Academy of Sciences, St. Petersburg
(Submitted June 15, 1998)
Pis'ma Zh. Tekh. Fiz. **24**, 52–57 (December 12, 1998)

Measurements were made of the absorption of microwave power in a discharge plasma generated using tapwater electrodes in atmospheric-pressure air in order to determine the electron density. The high-voltage discharge burned in a bulk (diffuse) form with a lower current density than an arc discharge. This type of discharge with nonmetallic liquid electrodes is extremely promising for various technical applications. Regimes with $I=50$–60 mA and voltages $U=2.9$–3.1 kV were studied. The measurements were made at probe radiation frequencies $F=29.6$ and 35.2 GHz. A two-conductor transmission line was used to localize the microwave power in the plasma. An estimate was obtained for the average electron density in the central part of the discharge $(4\times10^{11})<n_e<(7\times10^{11})\text{cm}^{-3}$. This result shows good agreement with the results of earlier probe measurements. © *1998 American Institute of Physics.* [S1063-7850(98)01012-X]

1. A self-sustained dc discharge between nonmetallic liquid electrodes, burning stably in air at atmospheric pressure in a diffuse (bulk) form, is an interesting physical object. The electrodes are usually electrolytes, aqueous solutions, or simply tapwater. Although this type of discharge has been known for around a century, the physical processes, composition, and properties of the discharge plasma have been little studied.[1] Earlier[2,3] we reported spectroscopic and probe investigations of this type of discharge using tapwater electrodes. A single electric probe was used to measure the distribution of the potential and electron density n_e along the discharge axis. Since it is difficult to interpret the results of probe measurements under these conditions, it seems necessary to compare the information obtained with results of measuring n_e by a different, preferably noncontact, method.

An analysis of the available calculated and experimental data[2,3] and of the scope of the different diagnostic techniques indicated that a suitable method of determining n_e may be to measure the absorption of microwave probe radiation by the plasma when its frequency is lower than the electron collision frequency.[4] Obviously, such a method presents some difficulties under our conditions (high gas pressure, relatively low electron density, small plasma dimensions, and spatial inhomogeneity).

2. Measurements of the absorption of microwave probe radiation were made in a dc discharge plasma in atmospheric-pressure air between two streams of tapwater. The thickness of the layer of water covering the metal conductors was 4–5 mm and the distance between the water electrodes was ≈7 mm. The measurements reported by Afanas'ev *et al.*[2] and Faure *et al.*[3] were made under similar conditions. Figure 1 shows the design of the discharge unit. One of the metal electrodes was grounded and to the other we applied a ≈4 kV voltage via a 10 kΩ ballast resistor. The discharge burns stably at currents I = 60–80 mA and voltages between the metal conductors $V\approx$ 2.9–3.1 kV.

3. Taking the results obtained in Refs. 2 and 3 as our basis, we shall analyze the conditions in the discharge plasma at a current $I\approx60$ mA. The diameter of the discharge near the electrodes is $2r\approx$ 4–5 mm and at the center of the interelectrode gap it is $2r\approx3$ mm. The plasma diameter was estimated from the half-width of the radial distribution of the radiation intensity at $\lambda=380.4$ nm (second positive system of N_2 bands, sequence $\Delta\nu=-2$). The probe measurements indicate that the electric field is nonuniform: $E\approx4$ kV/cm near the cathode, $E\approx2$ kV/cm near the anode, and $E\approx0.7$ kV/cm in the central part of the interelectrode gap. An estimate of the electron density using the electron branch of the probe characteristic gives $n_e\approx(4-6)\times10^{11}$ cm^{-3}. The spectral measurements show that the gas temperature near the cathode reaches ≈2000 K and decreases toward the anode to ≈1000 K, and the average electron energy is 0.35–0.4 eV. In a plasma with these parameters the electron–atom collision frequency ν is appreciably higher than the electron–electron collision frequency and is $\nu\sim10^2$ GHz and the plasma frequency is $f_0\leqslant10$ GHz.

In order to satisfy the conditions for the open-space method to be valid[4] and to achieve the necessary spatial resolution, the plasma must be probed with microwave radiation at wavelength $\lambda\approx10^{-1}$ cm. In this case, the frequency of the microwave probe radiation F will be almost two orders of magnitude higher than the plasma frequency f_0. With this frequency ratio the absorption of microwave radiation in the plasma will be extremely weak. The attenuation of the received microwave radiation caused by this absorption is described by

$$P/P_0=1-2\langle\alpha\rangle L, \tag{1}$$

where P and P_0 are the powers of the received microwave radiation with and without the plasma, respectively $\langle\alpha\rangle L=\int_0^L\alpha\, dl$, L is the distance covered by the microwave in the plasma, and α is the attenuation constant defined by[4]

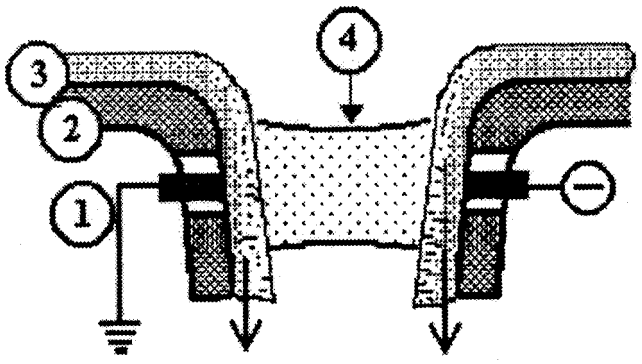

FIG. 1. Schematic of discharge unit: *1*—metal conductors, *2*—ceramics, *3*—tapwater, *4*—discharge plasma, and I—discharge.

$$\alpha^2=\frac{1}{2}\frac{\omega^2}{c^2}\left\{\left[\left(1-\frac{\omega_0^2}{\omega^2+\nu^2}\right)^2+\frac{\nu^2}{\omega^2}\left(\frac{\omega_0^2}{\omega^2+\nu^2}\right)^2\right]^{1/2}-\left(1-\frac{\omega_0^2}{\omega^2+\nu^2}\right)\right\}, \quad (2)$$

where $\omega=2\pi F$; $\omega_0=2\pi f_0=(4\pi n_e e^2/m_e)^{1/2}$.

The coefficient of absorption of $\lambda\approx 10^{-1}$ cm microwave radiation, estimated using formulas (1) and (2) is so small for our conditions $2\langle\alpha\rangle L\leqslant 10^{-3}$, that measurements of the weak attenuation caused by this absorption become technically difficult. The design characteristics of the discharge unit make it almost impossible to use cavity methods which can give high sensitivity. Thus, it is advisable to use longer-wavelength microwave radiation $\lambda\approx 1$ cm to probe the plasma. In this case, our estimates indicate that the attenuation of the microwave radiation is substantially greater, being a few percent. In our experiment a two-conductor line was used to localize the microwave power in a region having transverse dimensions $l\sim 5$ mm. If the ensuing attenuation of the microwave radiation is mainly caused by absorption in the plasma, the electron density averaged over a region of transverse dimension $\sim l$ and length L can be determined from measurements of the attenuation. Bearing in mind the difficulties mentioned above, even this estimate is of some interest at this stage of the research.

4. Figure 2 shows a block diagram of the measuring system. A waveguide channel of 7.2×3.4 mm cross section, consisting of fixed and moving parts, was used for microwave probing of the discharge plasma. The moving part contained waveguide elements, a two-conductor transmission line, a directional coupler with a microwave radiation detector and an absorber to suppress reflection from the end of the waveguide. The wave impedances of the waveguide and the two-conductor line were matched with smooth triangular waveguide joints $\approx$40 mm long without narrow walls. The two-conductor line was formed by two parallel copper wires 0.5 mm in diameter and 25 mm long with centers $\approx$4 mm apart, which were connected electrically to the pointed ends of the matching joints. The signal from the detector, which is proportional to the microwave radiation power transmitted by the channel, was recorded using an S9-8 storage oscilloscope with 10 s sweep time.

The measurements were made as follows. After the discharge had been ignited, the two-conductor line was inserted into the discharge gap midway between the electrodes so that the discharge channel was between the wires (Fig. 2). Signals from the microwave detector were recorded with the discharge switched on and off. It was observed that heating of the wires, which takes place within seconds, influences the recorded signal. Thus, the discharge was switched off 5 s after triggering the sweeping. The signal proportional to the received microwave radiation power was measured directly before and immediately after quenching the discharge. The noise was smoothed by an integrator with a time constant of $\sim 10^{-2}$ s. Several measurements were made at two frequencies, 29.6 and 35.2 GHz, and the results were then averaged.

5. Measurements at the discharge current $I=60$ mA yielded the following values of the absorption coefficient of the microwave probe radiation: $2\langle\alpha\rangle L=0.056$ (mean square deviation $\Delta=0.004$) at $F=29.6$ GHz and $2\langle\alpha\rangle L=0.034$ ($\Delta=0.003$) at $F=35.2$ GHz. In order to determine

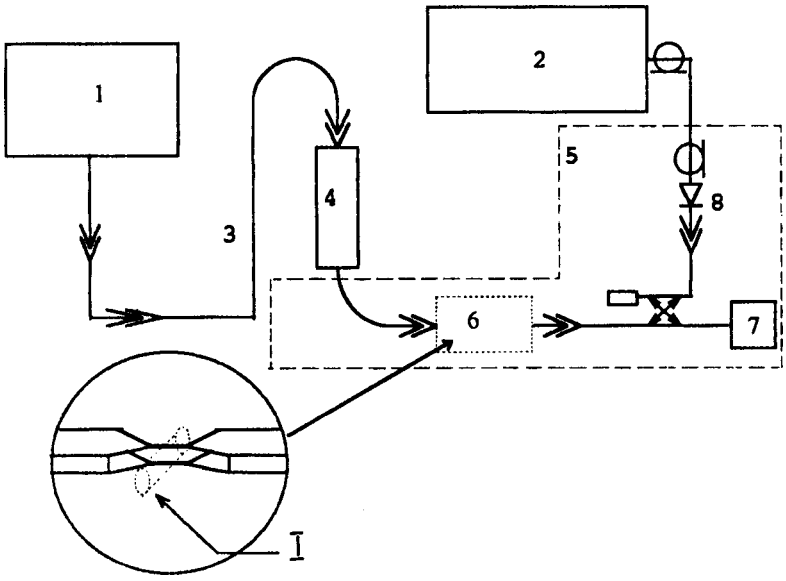

FIG. 2. Block diagram of apparatus: *1*—microwave oscillator, *2*—oscilloscope, *3*—fixed part of waveguide channel, *4*—connector, *5*—moving part of waveguide channel, *6*—two-conductor transmission line with matching elements, *7*—absorber, *8*—directional coupler with microwave radiation detector.

the average density using formulas (1) and (2), we need to know ν and the characteristic size of the plasma formation L. Calculations using different values of ν in the range $(100<\nu<200)$ GHz, which corresponds to the gas temperature $(2000>T>1000)$ K, show that the indeterminacy of ν in this range gives an error of at most 30% in the determination of n_e. The inaccuracy in estimating the size of the plasma formation from the results of spectroscopic measurements gives approximately the same contribution to the error. Taking into account these sources of error, the average electron density in a discharge with nonmetallic liquid electrodes with $I=60$ mA can be estimated as 4×10^{11} cm$^{-3}<n_e<7\times10^{11}$ cm^{-3}. These data show satisfactory agreement with the results of the probe measurements.

We propose in the future to employ this microwave technique to investigate an ac discharge with nonmetallic liquid electrodes using a gated integration technique.

[1] F. M. Gaĭsin and É. E. Son, *Electrophysical Processes in Discharges with Solid and Liquid Electrodes* [in Russian] (Urals University Press, 1989), pp. 357–376.
[2] V. P. Afanas'ev, P. Andre, Yu. A. Barinov, G. Faure, V. B. Kaplan, A. Lefort, and S. M. Shkol'nik, in *Proceedings of the 23rd ICPIG*, Toulouse, France, 1997, Vol. III, pp. 104–105.
[3] G. Faure and S. M. Shkol'nik, J. Phys. D **31**, 1212 (1998).
[4] V. E. Golant, *Microwave Methods of Plasma Research* [in Russian], Nauka, Moscow (1968), 328 pp.

Translated by R. M. Durham

Influence of chemical composition and excess free volume on surface crystallization of amorphous alloys

V. I. Betekhtin, A. G. Kadomtsev, V. E. Korsukov, O. V. Tolochko, and A. Yu. Kipyatkova

A. F. Ioffe Physicotechnical Institute, Russian Academy of Sciences, St. Petersburg;
St. Petersburg State Technical University
(Submitted July 2, 1998)
Pis'ma Zh. Tekh. Fiz. **24**, 58–64 (December 12, 1998)

Small-angle x-ray scattering and electron Auger spectroscopy were used to study the distribution of the excess free volume and the chemical composition of the surface layers of amorphous alloy ribbons. The relationship between these structure parameters and the surface crystallization characteristics of amorphous alloys is analyzed. © *1998 American Institute of Physics.*
[S1063-7850(98)01112-4]

Surface crystallization is a particular form of the crystallization of amorphous alloys obtained by quenching from a melt with single-sided heat transfer. In this case, we know that a dispersed crystalline phase forms primarily in the surface layers of the rapidly quenched amorphous ribbon.[1] A characteristic feature of this process is that the inside of the ribbon in contact with the roller and the outside in contact with the atmosphere are in different states. Accelerated surface crystallization may be observed on both sides of the ribbon, but cases of preferential crystallization on the outside or on the side in contact with the disk have been reported.[1,2] The reasons for this effect have not yet been fully clarified. The main cause of accelerated crystallization on the outside of the ribbon is obviously the slower rate of cooling during quenching, but the specific physical factors responsible for this process have not been completely identified. The situation on the inside of the ribbon is far more complicated, many different viewpoints are held,[1,2] and further experimental investigations are required to clarify this aspect.

Meanwhile, surface crystallization is of major practical importance for various applications of amorphous alloys. For instance, crystallization of the surface layers affects the catalytic activity and corrosion resistance of amorphous alloys and the properties of magnetically soft materials.[1,3,4] In this context, we investigated some characteristics of the surface crystallization of amorphous alloys, paying particular attention to the influence of the chemical composition of the surface layers on the crystallization process, i.e., a factor which, judging by the published data,[1,5–7] may have a very significant influence on the crystallization behavior. We first investigated how the surface crystallization is influenced by the distribution of excess free volume over the cross section of the ribbon. We have already shown[8] that amorphous alloys obtained by quenching from a melt have excess free volume in the form of pores with dimensions of tens of nanometers, which substantially influences the physicomechanical properties of the alloys.

1. MATERIALS AND EXPERIMENTAL METHOD

We mainly investigated the crystallization of an $Fe_{58}Ni_{20}Si_9B_{13}$ alloy obtained in the form of a 42 μm thick ribbon by quenching a melt on the outside of a rapidly rotating copper roller in vacuum.

The crystallization was investigated by x-ray diffraction analysis using a DRON-3 diffractometer with FeK_α monochromatic radiation. The alloys were heat-treated in sealed capsules in a resistance furnace with the temperature maintained to within ± 1K. An x-ray analysis was made after successive annealing for different times in the temperature range 593–673 K.

The chemical composition of the surface layers was analyzed by electron Auger spectroscopy using an LN-11 device. The vacuum in the preparation chamber was $P \equiv 10^{-8}$ mbar. The energy scanning range of the spectrum was 50–1050 eV, the modulation amplitude was 0.5–1 eV, and the ion beam energy 3 keV. The scanning area varied between 1×1 and 0.4×0.4 cm. The standard rate of sputtering of the surface by Ar ions was $\approx$1 nm/min.

The excess free volume in the amorphous alloys was investigated by small-angle x-ray scattering using a small-angle system with Kratky collimation and MoK_α radiation. The parameters of the system allowed us to determine inhomogeneities of between a few and hundreds of nanometers.

2. EXPERIMENTAL RESULTS

An analysis of the annealed samples revealed that in the cases studied the crystallization is more intensive on the contact side of the ribbon. The activation energies of these processes were determined by investigating the times before the onset of crystallization on both surfaces and in the bulk.

It should be noted that in all cases, surface crystallization begins slightly before the bulk process. Figure 1 gives the times before the onset of crystallization for the bulk and for the outside (*1*) and contact (*2*) surfaces of $Fe_{58}Ni_{20}Si_9B_{13}$ alloy plotted as a function of the reciprocal temperature. The unfilled symbols correspond to the maximum annealing time at which ''amorphous'' reflexes are observed, while the filled symbols correspond to the minimum annealing time at

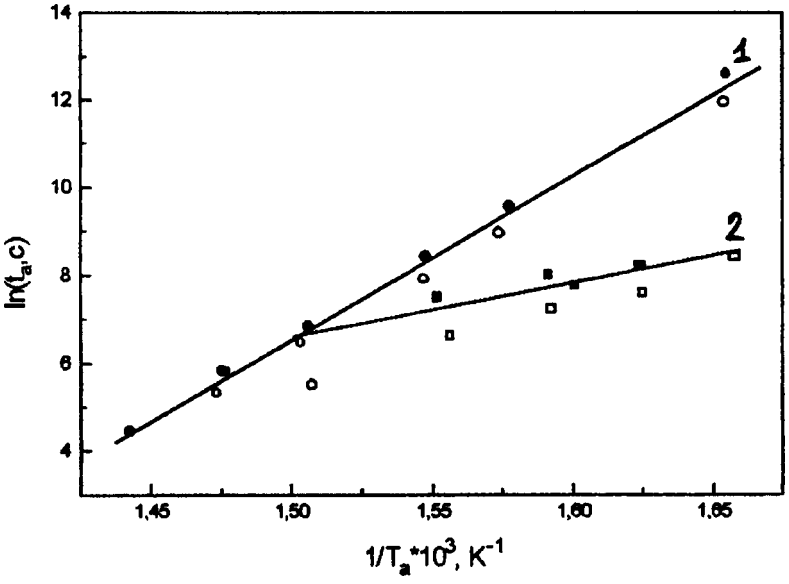

FIG. 1. Time before onset of crystallization of amorphous alloy versus isothermal holding temperature: *1*—bulk crystallization, *2*—crystallization of the contact (inner) surface of the ribbon.

which reflexes are observed from the crystals. The activation energy for the processes preceding crystallization on the outer surface and in the bulk of the material was the same to within experimental error, 310 kJ/mol. Crystallization of the contact surface takes place with a lower activation energy (125 kJ/mol) and is observed at lower temperatures than the bulk crystallization. As the temperature increases, the crystallization of the outer and inner surfaces of the ribbon observed by the x-ray technique begins almost simultaneously.

A characteristic feature of the crystallization of the contact surface is that the crystalline formations parallel to the plane of the ribbon are oriented along the most closely packed planes. An indication of this is that only peaks assigned to these planes are present on the diffraction patterns.

In order to identify the reasons for the preferential crystallization of the contact side of the ribbon, electron Auger spectroscopy was used to analyze the chemical composition of the surfaces of the ribbon during argon etching of layers to a depth of $\approx$100 nm. It was found that the contact surface is severely depleted in silicon and the boron content (around 10 at.%) corresponds to the lower concentration limit of the range of existence of the amorphous state, which can easily explain the reduced activation energy of the processes preceding crystallization. For $Fe_{85}B_{15}$, for example, this energy is 170 kJ/mol (Refs. 9 and 10). In our view, mention should also be made of the reduced relative content of nickel in the surface layers, Ni/Fe$\approx$1:3.5, whereas in the bulk this ratio is 1:2.8.

Investigations of the distribution of excess free volume by small-angle x-ray scattering revealed that in many amorphous alloys (including $Fe_{58}Ni_{20}Si_9B_{13}$) there are two or three fractions of pores.[2] The largest fraction is $\cong$100 nm. Gradually removing the surface layers by polishing revealed that this largest fraction of pores is concentrated mainly in a thin outer layer of the ribbon. Figure 2 gives the indicatrices of the small-angle scattering from the initial sample (*1*) and from the outer side after polishing (*2*) plotted as ln(I) versus φ^2. It was found that almost no large pores remained after a layer $\cong$2–3 μm thick had been removed. Estimates show that the specific surface area of these pores is $\cong 10^3$ cm^{-1}

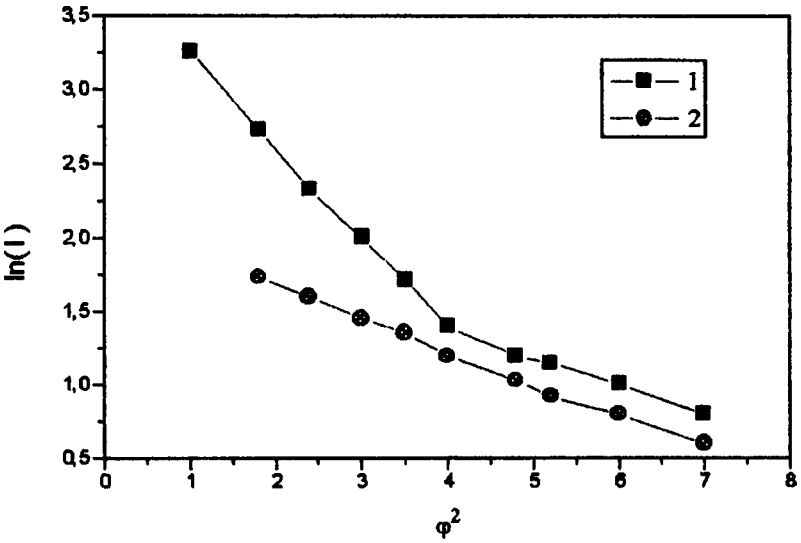

FIG. 2. Indicatrices of x-ray scattering from samples of $Fe_{58}Ni_{20}Si_9B_{13}$ amorphous alloy: *1*—initial state and *2*—after removal of a surface layer 2–3 μm thick (outside).

(the total surface area of the pores per unit volume). Note that no characteristics of a porous structure were observed on the inner surface.

We also obtained preliminary data indicating that the excess free volume concentrated in the surface layers influences the mechanical properties of the amorphous alloy. We found that after removing an outer layer 2–3 μm thick, the tensile strength of the amorphous alloy increased by 10–15%.

3. DISCUSSION OF RESULTS

These investigations of the surface crystallization process and structure of $Fe_{58}Ni_{20}Si_9B_{13}$ alloy have revealed the following results. On both surfaces crystallization is initiated earlier than in the bulk. However, the activation energy of this process is the same for the outer surface as for the bulk, whereas it is substantially lower for the inner surface (this is particularly noticeable at high temperatures). An analysis of the experimental data shows that one of the major factors that speeds up the crystallization on the outer surface is that the surface layers $\approx$2–3 μm thick contain an appreciable free surface area of pores. This conclusion shows good agreement with the reasoning put forward in Ref. 11, whereby the elastic energy decreases as a result of a change in volume during crystallization if this process takes place near the free surface. Note that we observed an increased density of $\approx$100 nm pores for four types of amorphous alloys, which suggests that the effect observed is a general one. There is obviously a small difference between the activation energies of the crystallization process for the outer surface and the bulk, but this is within experimental error.

The results of Auger spectroscopy have shown that for $Fe_{58}Ni_{20}Si_9B_{13}$ the concentrations of the main elements at the outer surface are similar to those in the bulk, whereas a reduced concentration of boron and especially silicon is observed at the inner surface. This is clearly responsible for the faster surface crystallization on the contact side of an amorphous ribbon of $Fe_{58}Ni_{20}Si_9B_{13}$ alloy, since the presence of Si (and also B) in amorphous Fe–Ni–B alloys substantially improves the stability of the amorphous state.[9,10] Significantly, Auger spectroscopy was also used to study the surface of other amorphous alloys ($Fe_5Co_{59}Ni_{10}Si_{11}B_{15}$, $Fe_{61}Co_{20}Si_5B_{14}$). These revealed no significant boron or silicon depletion of the contact side and no accelerated crystallization.

To sum up, we can draw the following conclusions, at least for the alloy studied. Accelerated crystallization of the outer surface of an amorphous alloy obtained by quenching from a melt is to a considerable extent attributable to the excess free volume present in the surface layer, whereas accelerated crystallization of the inside is caused by a change in the chemical composition of these layers.

The authors are grateful to the Russian Fund for Fundamental Research for financial support (Grant No. 97-02-17412).

[1] *Metastable and Nonequilibrium Alloys*, edited by Yu. V. Efimov [in Russian], Metallurgiya, Moscow (1988), 382 pp.
[2] Z. Metall. **75**, 5 (1984).
[3] N. B. Kekalo and F. Lefter, Fiz. Met. Metalloved. **68**(2), 280 (1989).
[4] A. P. Potapov, I. V. Dmitrieva, and A. A. Glazer, Fiz. Met. Metalloved. **79**(2), 51 (1995).
[5] H. S. Chen and A. Inoue, J. Non-Cryst. Solids **61–62**, 805 (1984).
[6] U. Köster, Mater. Sci. Eng. **97**, 233 (1988).
[7] Yu. A. Pustov, Yu. V. Baldokhin, V. Yu. Labutin *et al.*, Poverkhnost' **11**, 130 (1989).
[8] V. I. Betekhtin, A. M. Glezer, A. G. Kadomtsev, and A. Yu. Kipyatkova, Fiz. Tverd. Tela (St. Petersburg) **40**(1), 85 (1998) [Phys. Solid State **40**, 74 (1998)].
[9] K. Sudzuki, Kh. Fudzimori, and K. Khasimoto, *Amorphous Metals* [in Russian], Metallurgiya, Moscow (1987), 328 pp.
[10] M. Scott, *Rapidly Quenched Metals* [Russ. transl.], Metallurgiya, Moscow (1983), pp. 106–117.
[11] H. J. Güntherode and H. Beck, *Glassy Metals* (Springer-Verlag, Berlin, 1981; Mir, Moscow, 1983, 376 pp.).

Translated by R. M. Durham

Vibroelectronic emission

Kh. N. Vezirov

Research Institute of Photoelectronics, Baku
(Submitted June 11, 1998)
Pis'ma Zh. Tekh. Fiz. **24**, 65–69 (December 12, 1998)

A newly discovered effect in which electrons are emitted from a vibrating silver–oxygen–cesium photocathode is described. [S1063-7850(98)01212-9]

Several emission effects are known in which electrons are emitted by solids under the action of various internal and external factors. These include thermionic, photoelectronic, secondary electron, field electron, exoelectronic, and explosive electron emission.[1–3]

During an investigation of the properties of Ag–O–Cs films (so-called silver–oxygen–cesium photocathodes), the author observed what is apparently yet another emission effect, involving the emission of electrons from a vibrating photocathode.

The apparatus is shown schematically in Fig. 1. A silver–oxygen–cesium photocathode *3* approximately 30 nm thick was deposited on one surface of a quartz resonator *1* with metal film contacts *2* in a vacuum of 10^{-6}–10^{-7} Pa. This vacuum vessel also contained another electrode (anode) consisting of a layer of phosphor *5* deposited on glass *4*, coated with a thin aluminum layer *6* which was transparent to electrons but completely opaque to light. A forward potential difference (i.e., positive at the anode) was created between the anode and the photocathode by means of a supply unit *7*. In the dark, a thermionic emission current of approximately 0.1 nA flowed in the vacuum gap between the anode and the photocathode (the photocathode had an area of 3 cm^2 and was at room temperature). When the photocathode was illuminated by visible light, a photoelectronic emission current appeared. The overall sensitivity of the photocathode reached 70 μA/lm and the long-wavelength photoemission threshold was 1.7 μm. In this case the photocurrent could be measured by recording the voltage across a resistance box *8* and feeding this signal to an oscilloscope *9* or a selective voltmeter V6-4.

Radiation at wavelengths longer than 1.7 μm induced no photoemission.

An rf voltage, at a frequency of the order of 3 MHz, was then applied to the cavity *1* from a special generator *10* causing rf oscillations (vibrations) of the photocathode. In this situation, electrons were emitted from the photocathode in the dark and an rf emission current of 0.02 μA flowed to the anode, i.e., this current was more than two orders of magnitude greater than the thermionic emission current. Its frequency was the same as the resonator vibration frequency. This experiment was carried out in the dark, i.e., there was no photocurrent. Note that the observed effect is not simply modulation of the thermionic current, since the number of charges (electrons) transferred per unit time would be the same in this case and when the thermionic current was collected without any vibration of the photocathode, whereas in the experiments these values differed by two orders of magnitude.

The photocathode was then exposed to infrared radiation at wavelengths beyond the long-wavelength photoemission limit (i.e., greater than 1.7 μm). This radiation did not induce photoemission by itself, but when the resonator was vibrating, it amplified the electron emission (Fig. 2). This dependence of the vibroelectronic emission on the wavelength (energy) of the incident radiation is most likely attributable to the band structure of this photocathode[4] and its optical properties.

The generator *10* was then switched off, the measuring system was disconnected by means of a switch *11*, and a high forward voltage (5–15 kV) was applied to the anode from a high-voltage supply unit *12*. In this case, illumination of the photocathode resulted in the appearance of photoelectronic emission from its surface. The electrons emitted by the photocathode entered the electric field, where they were accelerated to 5–15 keV and then bombarded the phosphor, causing it to luminesce, which was observed through the glass *4*.

The photocathode illumination was then switched off (the photocurrent and the luminescence of the phosphor disappeared) and the rf generator *10* was again switched on in the dark (i.e., without any photocathode illumination) with the high voltage applied to the anode. When the generator was switched on, the phosphor began to luminesce again, which indicated that electrons were being emitted from the photocathode, since the phosphor can only luminesce under electron bombardment.

Strange as it may seem, an analysis of these results yields the conclusion that the rf vibrations of the photocathode cause it to emit electrons.

No experiments were carried out at different frequencies because of the limitations of the apparatus.

However, it should be noted that general experiments with rf vibrations of various films have already been carried out, such as experiments using quartz thickness meters. In these experiments measurements were made of the mass and therefore the thickness of films deposited in vacuum, i.e., in all the experiments the films were made to vibrate. However, no currents were observed in these numerous investigations. Nevertheless, electron emission is observed when a silver–oxygen–cesium photocathode vibrates.

An explanation for this effect should clearly be sought in

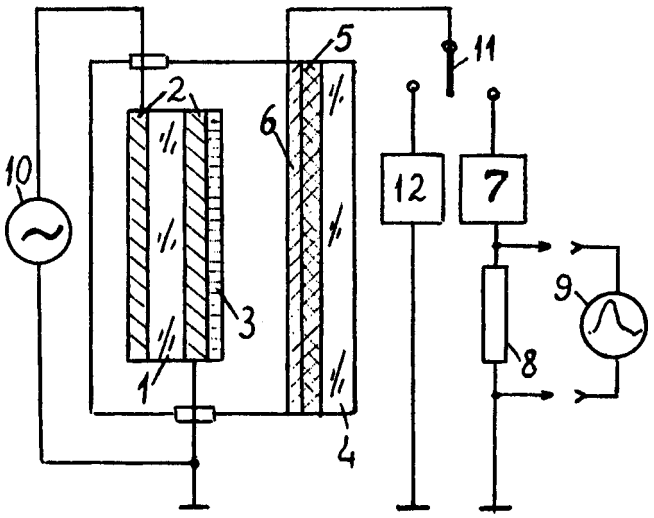

FIG. 1. Schematic diagram of experiment.

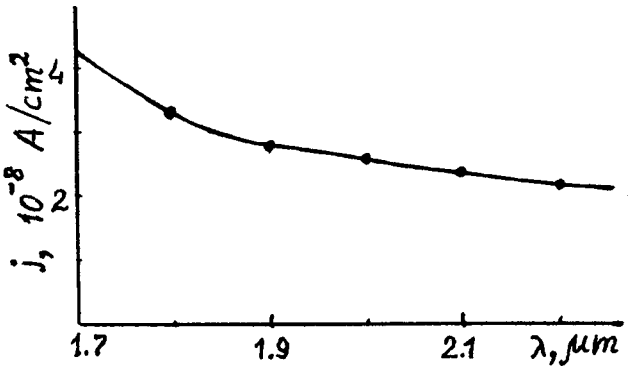

FIG. 2. Vibroelectronic emission current density as a function of wavelength in the range above the photoemission threshold.

the emission (surface) properties of this film. We know[5] that of all known films, a silver–oxygen–cesium photocathode has the lowest electron work function. This work function (more accurately the electron affinity, i.e., the energy spacing between the bottom of the conduction band and the energy level of a free electron in vacuum) may be less than 0.2–0.3 eV, and in some microscopic sections of the order of 100 Å distributed uniformly over the entire surface of the photocathode, could even be zero (so-called zero electron affinity),[4,6] which is more than an order of magnitude less than the average work function of other well-known materials (3–5 eV). Thus, it becomes more or less clear, albeit qualitatively, why this effect is observed specifically in a silver–oxygen–cesium photocathode.

It is thought that this effect should show up clearly in photocathodes with negative electron affinity[7] and should be useful for studying films having a low work function.

[1] R. L. Sproull, *Modern Physics*, Wiley, New York (1956); Nauka, Moscow (1974), 592 pp.
[2] E. Rabinowicz, Sci. Am. **236**(1), 74 (1977).
[3] G. A. Mesyats, *Generation of High-Power Nanosecond Pulses* [in Russian], Sovetskoe Radio, Moscow (1974), 256 pp.
[4] B. M. Gugel', A. E. Melamid, and B. M. Stepanov, Radiotekh. Elektron. **22**(7), 1466 (1977).
[5] V. S. Fomenko, *Handbook of Emission Properties of Materials* [in Russian], Naukova Dumka, Kiev (1981), p. 223.
[6] A. A. Zhigare and G. G. Shamaeva, *Electron-Beam and Photoelectronic Devices* [in Russian], Vysshaya Shkola, Moscow (1982), 463 pp.
[7] *Optical and Infrared Detectors*, edited by R. J. Keyes (Springer-Verlag, New York, 1977; Radio i Svyaz', Moscow, 1985, p. 153).

Translated by R. M. Durham

Estimate of the potential relief (rippling) of a surface associated with adsorption of *d*-metal atoms on *d*-substrates

S. Yu. Davydov

A. F. Ioffe Physicotechnical Institute, Russian Academy of Sciences, St. Petersburg
(Submitted June 19, 1998)
Pis'ma Zh. Tekh. Fiz. **24**, 70–74 (December 12, 1998)

A cohesion approach developed previously by Davydov and Tikhonov to describe adsorption properties [Surf. Sci. **371**, 157 (1997)] is used to calculate the ripple parameter $\Omega = E_{\rm dif}/E_{\rm des}$ (where $E_{\rm dif}$ and $E_{\rm des}$ are the activation energy of surface diffusion and the adsorption energy) for atoms of *d*-metals adsorbed on a W(110) surface. The results of the calculations show good agreement with the experimental data. © *1998 American Institute of Physics.* [S1063-7850(98)01312-3]

The potential relief of an adsorption system (Fig. 1) can be estimated quantitatively by the ripple parameter Ω (Ref. 1), defined as the ratio of the activation energy of surface diffusion $E_{\rm dif}$ to the desorption energy $E_{\rm des}$:

$$\Omega = E_{\rm dif}/E_{\rm des}. \tag{1}$$

To calculate Ω an approach which can describe both desorption and diffusion from a unified viewpoint is indicated. The most popular approach so far is the embedded atom method (see Refs. 2–4 and the literature cited). Based on a local density functional method and a representation of the total energy of the system as a sum of the so-called embedding energy (which depends only on the local electron density) and the short-range electrostatic energy, the embedded atom method requires a fitting procedure to determine the characteristic parameters of the method. However, this method does have some disadvantages and occasionally gives qualitatively incorrect results.[4] In Ref. 5 the cohesion approximation to calculate the adsorption properties of atoms of *d*-metals adsorbed on *d*-substrates was used to propose an approach to calculate the desorption energy and activation energy of surface diffusion without using fitting and computer calculations. Here the cohesion approximation is used to calculate the ripple parameter Ω.

In Ref. 5, an experimentally observed correlation between the desorption energy of transition metal atoms on W(110) and the cohesion energy of crystals formed between the atoms was used as the basis to suggest that the desorption energy could be described as the cohesion energy of a ''renormalized atom'' or adatom. It was also shown that for atoms of transition metals adsorbed on *d*-substrates, charge transfer can be neglected and direct allowance need only be made for interaction between an adatom and the nearest substrate atoms whose number n naturally depends on the surface structure and the position of the adsorbed atom. We took as our starting point the cohesion theory developed by Harrison and Wills,[6] where the electron density of a metal is represented as a superposition of quasifree states and *d*-states with allowance for their hybridization and electron–electron interaction described by the Thomas–Fermi model. The following expression was obtained for the energy $E_{\rm coh}$:

$$E_{\rm coh}(n) = E_s - E_b(n) - E_c(n), \tag{2}$$

$$E_s = \frac{3}{4} Z_s \frac{\hbar^2 \pi^2}{m d^2}(1-a), \tag{3}$$

$$E_b(n) = -\frac{1}{2} Z_d (1 - Z_d/10)(30.9)\sqrt{n}\,\frac{\hbar^2 r_d^3}{m d^5}, \tag{4}$$

$$E_c(n) = Z_d n (11.40)\frac{\hbar^2 r_d^6}{m d^8}. \tag{5}$$

Here $Z_{s(d)}$ is the occupancy of the s (d)-band ($Z_s + Z_d = Z$, where Z is the number of valence electrons per atom), $a = (4/5)(3Z_s/2\pi)^{2/3}$ for fcc and hcp lattices, $a = (6/5) \times (3Z_s/4\pi)^{2/3}$ for a bcc structure, n is the number of nearest neighbors, d is the distance between nearest neighbors in the crystal, r_d is the radius of the d states, m is the electron mass, and $\hbar$ is Planck's constant. Equation (3) describes the contribution of quasifree electrons to the cohesion energy, Eq. (4) gives the contribution of the *d*-band, and Eq. (5) describes the shift of the center of gravity of the *d*-band. Thus, the desorption energy $E_{\rm des}$ of a *d*-metal atom adsorbed at the center of a W(110) surface cell is $E_{\rm coh}$ ($n_c = 4$).

We shall analyze the following simplified pattern proposed in Ref. 5 to calculate the activation energy of surface diffusion. We assume that during hopping from one surface cell to another (neighboring) one, the length of the adsorption bond remains the same. This is shown in Fig. 2 for a

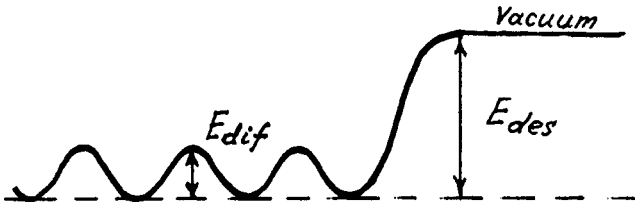

FIG. 1. Potential relief of adsorption system.

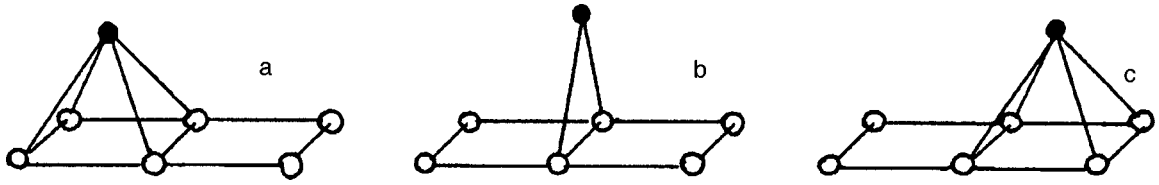

FIG. 2. Schematic of diffusion pattern: a — initial position of adatom, b — position of adatom on crossing the boundary between neighboring surface cells (b-type diffusion), c — final position of adatom.

W(110) surface cell and diffusion hopping of an adatom across the boundary between neighboring cells, i.e., for b (bridge) diffusion. At the initial and final stages of the hopping (Figs. 2a and 2c), the adatom has four nearest neighbors ($n_c=4$). At the instant of transition between cells (Fig. 2b) this number is $n=n_b=2$. In this case, the activation energy of surface diffusion is

$$E_{\mathrm{dif}}=E_{\mathrm{coh}}(4)-E_{\mathrm{coh}}(2). \tag{6}$$

Thus, we obtain

$$\Omega=1-\frac{E_{\mathrm{coh}}(2)}{E_{\mathrm{coh}}(4)}. \tag{7}$$

The results of calculating Ω are given in Table I. The values of d were taken from Ref. 7 and r_d from Ref. 8. For the calculations we used two methods of determining the parameters d, r_d, Z_d, and $Z_d(1-Z_d/10)$ of the adsorption system, geometric and arithmetic averaging (for further details see Ref. 5). As in Refs. 5, 6, and 8 we took $Z_s=1.5$ for all cases except Cu, Ag, and Au, where we assumed $Z_s=2$. It can be seen from Table I that for geometric averaging the parameter Ω has a weakly defined maximum for the third element of the d series, whereas for arithmetic averaging Ω decreases slightly from the beginning to the end of the d series.

We shall compare the calculated values of the ripple parameter with the available experimental results,[1,5,9–11] which are unfortunately few and far between, even though adsorption and diffusion of transition metal atoms on W(110) have been studied more comprehensively than for other adsorption systems. Consider the $3d$ series. For titanium Seebauer and Allen[1] give $E_{\mathrm{dif}}=0.95$ eV, whereas our calculations give 0.88 and 1.03 eV for geometric and arithmetic averaging, respectively. For E_{des}, Seebauer and Allen[1] only quote an approximate value of 5.64 eV (no corresponding experimental value is available) which gives $\Omega=0.17$. This value seems rather exaggerated to us. For nickel these authors give $\Omega=0.11$, and for copper[1,5] $\Omega=0.15$. Our values are far lower, which can be attributed to the characteristics of the calculations of E_{des} for Cu, Ag, and Au (see the discussion of this topic in Ref. 5). For the $4d$ series Seebauer and Allen[1] give $\Omega=0.11$, 0.11, and 0.095 for Rh, Pd, and Ag, respectively which agrees well with our estimates. For tantalum Seebauer and Allen[1] give $\Omega=0.10$, 0.11, whereas from Ref. 5 we have $\Omega=0.10-0.13$. For tungsten Seebauer and Allen[1] give $\Omega=0.087$, 0.11, 0.15; for rhenium[1,5] $\Omega=0.10$, and for iridium values of 0.12 and 0.13 are obtained from Ref. 1 and $\Omega=0.10-0.13$ from Ref. 5. For platinum we find $\Omega=0.12$ (Ref. 1) and $\Omega=0.10-0.12$ (Ref. 5), and for gold $\Omega=0.13$.

Thus, with the exception of copper and gold our results show good agreement with the available experimental data. For Cu, Ag, and Au, arithmetic averaging works considerably better than geometric; for the other transition metal atoms both approximations give almost the same results. Note that despite the appreciable changes in the desorption energy and diffusion activation energy in d series, the ripple parameter varies only slightly. This indicates that a correlation exists between the changes in E_{des} and E_{dif}. An analysis reveals that this correlation is based on variation of the parameter $Z_d(1-Z_d/10)$, which indicates that the d band plays a dominant role in the formation of the adsorption characteristics.

This work was carried out as part of the program ''Surface Atomic Structures.''

TABLE I. Calculation of the ripple parameter Ω for adsorption of d-metal atoms on W(110).

	Ω			Ω			Ω	
Adatom.	geom.	arith.	Adatom	geom.	arith.	Adatom	geom.	arith.
Sc	0.10	0.12	Y	0.11	0.13	Lu	0.11	0.13
Ti	0.12	0.12	Zr	0.12	0.13	Hf	0.12	0.13
V	0.14	0.12	Nb	0.13	0.12	Ta	0.13	0.13
Cr	0.12	0.12	Mo	0.12	0.12	W	0.12	0.12
Mn	0.11	0.11	Tc	0.12	0.12	Re	0.12	0.12
Fe	0.10	0.11	Ru	0.11	0.12	Os	0.10	0.11
Co	0.09	0.10	Rh	0.07	0.10	Ir	0.09	0.10
Ni	0.07	0.09	Pd	0.06	0.09	Pt	0.08	0.09
Cu	0.03	0.08	Ag	0.03	0.08	Au	0.01	0.08

[1] E. S. Seebauer and C. E. Allen, Prog. Surf. Sci. **49**(1), 265 (1995).
[2] C. L. Liu, J. M. Cohen, J. B. Adams, and A. F. Voter, Surf. Sci. **253**, 334 (1991).
[3] C. M. Chang, C. M. Wei, and S. P. Chen, Phys. Rev. B **54**, 17 083 (1996).
[4] P. J. Feibelman, J. S. Nelson, and G. L. Kellogg, Phys. B **49**, 10 548 (1994).
[5] S. Yu. Davydov and S. K. Tikhonov, Surf. Sci. **371**, 157 (1997).
[6] J. M. Wills and W. A. Harrison, Phys. Rev. B **29**, 5486 (1984).
[7] C. Kittel, *Introduction to Solid State Physics*, 5th ed. (Wiley, New York, 1976; Nauka, Moscow, 1978, 792 pp.).
[8] J. M. Wills and W. A. Harrison, Phys. Rev. B **28**, 4363 (1983).
[9] A. G. Naumovets and Yu. S. Vedula, Surf. Sci. Rep. **4**, 365 (1985).
[10] T. T. Tsong, Rep. Prog. Phys. **51**, 659 (1988).
[11] R. Gomer, Rep. Prog. Phys. **53**, 917 (1990).

Translated by R. M. Durham

Spectropolarimetry of multimode quartz fibers in the infrared

D. A. Dmitriev and V. T. Prokopenko

St. Petersburg Institute of Precision Mechanics and Optics (Technical University)
(Submitted September 16, 1997; resubmitted April 20, 1998)
Pis'ma Zh. Tekh. Fiz. **24**, 75–80 (December 12, 1998)

Results are presented of experimental spectropolarimetric investigations of multimode fiber-optic waveguides with core diameters between 65 and 404 μm in the infrared (0.8, 1.3, and 1.55 μm). A theoretical explanation is proposed for the results. © *1998 American Institute of Physics.* [S1063-7850(98)01412-8]

Multimode fiber-optic waveguides are considerably inferior to single-mode fibers in terms of wide-band parameters and optical losses, but they have undoubted advantages when used in short-distance data transmission and processing systems such as on-board and on-chip applications. Advantages of multimode fibers include efficient coupling of radiation in and out of the fiber, the efficient fabrication of microscopic devices using these, and also their low cost. Before multimode fibers can be fully utilized in practice, we need to know their polarization characteristics in the 0.8–1.55 μm infrared region, which corresponds to the lowest radiation losses in quartz fibers and the operating wavelengths of high-power semiconductor light sources. Important results on the polarization properties of multimode fibers have been obtained in various theoretical and experimental studies.[1–7] Until recently, however, no systematic spectropolarimetric investigations of multimode fibers had been made over a broad section of the infrared. Here we present results of measurements of the depolarizing properties of multimode fibers in the 0.8–1.55 μm range and suggest a theoretical interpretation of the results.

The apparatus used for the spectropolarimetric investigations of multimode fibers is shown schematically in Fig. 1. Linearly polarized infrared radiation is coupled into the fiber by means of a microscope objective *7*. The degree of polarization of the radiation at the fiber exit is measured by a conventional technique involving rotating an analyzer *12*. The samples were quartz multimode fibers with a stepped refractive index profile, and were between 16.4 and 1098 cm long. The fiber core between 65 and 400 μm in diameter was made of borosilicate glass, the relative refractive index difference between the core and the cladding was 0.3–0.5%, and the numerical aperture of the fibers was 0.30–0.55.

Experiments confirmed that the position of the azimuth of the preferential linear polarization of partially polarized light at the fiber exit is uniquely determined by the polarization azimuth of the input radiation. In the experiments we actually measured the integrated degree of polarization P of the output radiation, obtained by averaging the polarization parameters of the fiber modes over its total cross section. The polarization of the light at each point in the cross section of a multimode fiber is the result of a superposition of numerous (several hundred) guided vector modes of the fiber.

A rigorous theoretical description of these complex wave fields involves using a formalism of random functions which characterize the Stokes parameters of the radiation in different parts of the fiber cross section. Here we analyze the degree of polarization P using the experimentally established fact that when a multimode fiber is excited by linearly polarized light, virtually all the radiation modes at the fiber exit exhibit linear partial polarization.[8] If the polarized component of the radiation within an isolated mode possesses elliptic polarization with the ellipticity parameter

$$\gamma=(1-e^2)/(1+e^2),$$

where e is the ratio of the minor and major semiaxes of the polarization ellipse, the measured quantity is $P=\gamma P_R$, where P_R is the real degree of polarization. According to Snopko,[4] the ellipticity parameter in multimode fibers is $\gamma\approx 1$ and thus the experimentally measured value of P determines at least the lower limit of the real degree of polarization P_R.

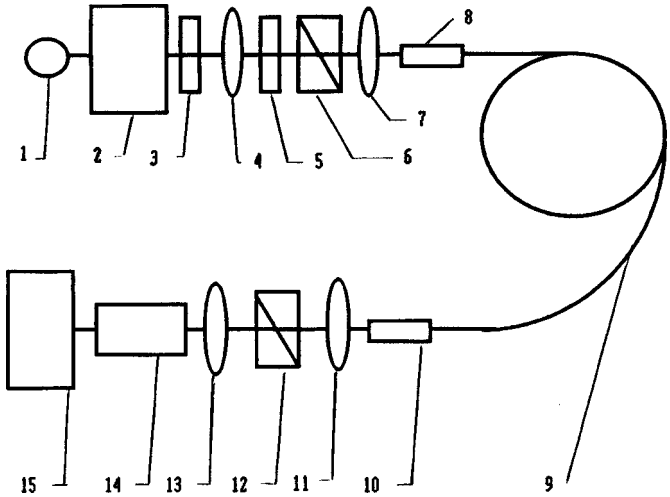

FIG. 1. Schematic of measuring system for spectropolarimeteric investigations of fiber-optic waveguides: *1* — light source, *2* — monochromator, *3* — light beam modulator, *4* — collimating lens, *5* — infrared light filter which cuts out the second order, *6* — linear polarizer (Glan prism), *7* — microscope objective (for coupling in radiation), *8* — adapter (mounted on micropositioner), *9* — fiber-optic waveguide, *10* — adapter, *11* —microscope objective, *12* — analyzer (Glan prism), *13* — focusing lens, *14* — photodetector (germanium photodiode with electronic preamplifier), and *15* — meter for input signal level.

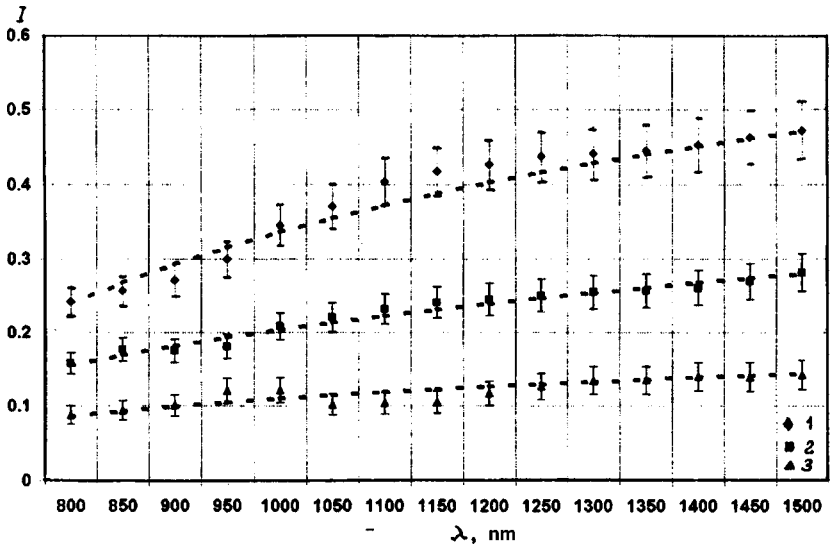

FIG. 2. Experimental and calculated dependences of the degree of polarization I on the wavelength for 165 mm long fibers of different diameter. The calculated curves are shown by the dashed lines. The experimental data correspond to *1* — 65 μm, *2* — 187 μm, and *3* — 318 μm.

The experimental spectral dependence of the degree of polarization of the radiation at the exit of various types of multimode fibers (165 mm long) excited by linearly polarized light from a thermal source is plotted in Fig. 2. When the measurements were repeated, the experimental data showed good reproducibility. Most of the fiber samples typically show a tendency for the degree of polarization of the radiation at the fiber exit to increase with wavelength. The fact that the curve $P(\lambda)$ is not strictly monotonic indicates that the formation of the polarization structure in multimode fibers is a complex process in which interaction between guided modes caused by structural defects and scattering of radiation in the bulk of the fiber core should play an important role.

To a first approximation, the increased degree of polarization with increasing wavelength may be explained using the following simple model of the depolarization of light in a fiber. The change dI in the power of the completely polarized radiation component over the fiber length dL is proportional to the variations ΔN in the number of guided fiber modes:

$$dI \sim -I\ \Delta N\ dL. \tag{1}$$

Assuming that the well-known relation $\Delta N \equiv \sqrt{N}$ is satisfied for the thermal radiation, where the number of modes is $N=(NA)^2(2\pi^2a^2)/\lambda^2$ (NA is the numerical aperture of the fiber, a is the core radius, and λ is the wavelength of light), the degree of polarization P of the light leaving a fiber of length L is

$$P = C_1 \exp\left\{ -C_2 \frac{\pi a \sqrt{2}}{\lambda} (NA) \right\} + C_3, \tag{2}$$

where C_1, C_2, and C_3 are constants. The dashed curves in Fig. 2 give the calculated functions $P(\lambda)$, as given by formula (2), plotted for the experimental values of a, A, and I. The constants C_1, C_2, and C_3 are given in Table I. Quite clearly, formula (2) correctly describes the trend of the degree of polarization to increase with the wavelength λ. A more detailed theoretical analysis of the depolarization of light in multimode fibers will allow us to determine how the coefficients C_1, C_2, and C_3 depend on the geometric parameters of the fiber and on the wavelength, using a more accurate approximation which should give better agreement between the experimental and calculated results.

Another interesting topic is the influence of the degree of coherence of the light source on the depolarization of the radiation in a multimode fiber. Measurements were made of the degree of polarization of the radiation at the exit of a fiber excited by linearly polarized light from semiconductor lasers at wavelengths of 0.85, 1.32, and 1.52 μm. The relative spectral line width of the sources was between 10^{-2} and 10^{-3}. Table II gives the relevant experimental data for a 16.5 cm long fiber. The degree of polarization of light at the exit of multimode fibers excited by a narrow-band laser source is usually higher than that under the action of a thermal source at the same wavelength. The differences in the degree of polarization are more pronounced for the fiber with a comparatively large core diameter. An increase in the degree of polarization with increasing wavelength is observed at relatively short wavelengths (0.85–1.35 μm). A possible

TABLE I. Values of the coefficients C_1, C_2, and C_3 for various types of optical fibers.

	65 μm	187 μm	318 μm
C_1	3.15	0.64	0.5
C_2	0.002	0.002	0.00039
C_3	−2.39	−0.154	−0.280

TABLE II. Degree of polarization of light at the exit of multimode fiber-optic waveguides excited by semiconductor laser radiation (fiber length 16.5 cm).

Wavelength, μm	Diameter of fiber core, μm			
	65	187	318	404
0.85	0.26	0.18	0.04	0.03
1.32	0.54	0.54	0.31	0.21
1.53	0.47	0.48	0.05	0.20

reason for this is the spectral dependence of the ellipticity parameter for the different fiber modes.

A detailed analysis of the influence of the coherence of the light sources on the depolarization of light in multimode fibers merits independent investigations. Studies of the transformation of the polarization in multimode fiber-optic waveguides over a wide range of wavelengths will extend the ranges of application of these fibers in data transmission and processing systems and in devices for measuring the parameters of physical fields.

[1] A. W. Snyder and J. D. Love, *Optical Waveguide Theory* (Methuen, London, 1984; Radio i Svyaz, Moscow, 1987).

[2] W. A. Shurcliff, *Polarized Light: Production and Use* (Harvard University Press, Cambridge, Mass., 1962; Mir, Moscow, 1965, 64 pp.).

[3] A. M. Bykov, I. S. Volkov, A. V. Volyar *et al.*, Opt. Spektrosk. **61**(1), 190 (1986) [Opt. Spectrosc. **61**, 123 (1986)].

[4] V. N. Snopko, *Polarization Characteristics of Optical Radiation and Methods of Measuring Them* [in Russian], Nauka i Tekhnika, Minsk (1992), p. 336.

[5] O. I. Kotov, O. L. Marusov, V. M. Nikolaev *et al.*, Opt. Spektrosk. **70**(4), 924 (1991) [Opt. Spectrosc. **70**, 540 (1991)].

[6] L. M. Kuchikyan and A. V. Volyar, Ukr. Fiz. Zh. **22**, 1658 (1977).

[7] A. M. Bykov, A. V. Volyar, M. E. Kondakov *et al.*, Opt. Spektrosk. **53**(3), 517 (1982) [Opt. Spectrosc. **53**, 304 (1982)].

[8] R. M. A. Azzam and N. M. Bashara, *Ellipsometry and Polarized Light* (North Holland, Amsterdam, 1977; Mir, Moscow 1981).

Translated by R. M. Durham

GaAsN/GaAs and InGaAsN/GaAs heterostructures grown by molecular beam epitaxy

A. Yu. Egorov, A. E. Zhukov, A. R. Kovsh, V. M. Ustinov, V. V. Mamutin, S. V. Ivanov, V. N. Zhmerik, A. F. Tsatsul'nikov, D. A. Bedarev, and P. S. Kop'ev

A. F. Ioffe Physicotechnical Institute, Russian Academy of Sciences, St. Petersburg
(Submitted July 2, 1998)
Pis'ma Zh. Tekh. Fiz. **24**, 81–87 (December 12, 1998)

Molecular beam epitaxy was used to fabricate GaAsN/GaAs and InGaAsN/GaAs heterostructures, and the influence of the growth regimes on their characteristics was studied. It is shown that implantation of nitrogen causes a substantial long-wavelength shift of the radiation. The possibility of obtaining 1.4 μm radiation at room temperature was demonstrated using $In_{0.28}Ga_{0.72}As_{0.97}N_{0.03}$/GaAs quantum wells. © *1998 American Institute of Physics.* [S1063-7850(98)01512-2]

INTRODUCTION

A light source emitting in the range 1.3–1.55 μm is extremely promising for applications in fiber-optic communication lines. However, this important direction of research and development remains outside the scope of modern GaAs-based laser technology because of the fundamental constraint on the emission wavelength attainable in GaAs/InGaAs heterostructures ($\sim$1.1 μm) as a consequence of the large difference in the lattice constants. Semiconductor structures for optoelectronics devices in the optical range are now being synthesized using InGaAsP/InP materials. A shortcoming of lasers using these structures is the low thermal stability of the characteristics at room temperature as a result of the inadequate electron confinement. In addition, the quality of InP substrates is substantially inferior and the cost far higher than those of GaAs substrates. It was recently shown that the four-component compound InGaAsN and InGaAsN/GaAs heterostructures may be extremely promising for improving the characteristics of lasers for fiber-optic communication lines, since these can substantially increase the emission wavelength of GaAs heterostructures and improve the thermal stability of lasers emitting near 1.3 μm (Refs. 1–3). We now report the growth of InGaAsN/GaAs heterostructures on GaAs substrates by molecular beam epitaxy. These structures emit at 1.4 μm at room temperatures and contain 3% nitrogen in the four-component compound.

EXPERIMENT

The structures were grown by molecular beam epitaxy on semi-insulating GaAs(100) substrates in an ÉP-1203 system fitted with a Leybold-Heraeus turbomolecular pump with a pumping speed of 560 l/s. During this study we used standard solid-state Ga, In, and As sources. An Astex electron-cyclotron-resonance microwave gas discharge source with an operating frequency of 2.45 GHz created a flux of active nitrogen radicals to the growth surface. Layers of GaAsN 0.2 μm thick and InGaAsN/GaAs quantum wells were grown on a 0.1 μm thick GaAs buffer layer. The quantum-well structures terminated with a 0.1 μm thick GaAs covering layer. The GaAs growth rate in our experiments was 0.5–1.0 μm/h. The GaAs growth rate was calibrated by measuring the oscillation period of the peak intensity on the reflection high-energy electron diffraction (RHEED) pattern, and the InAs growth was calibrated from the appearance of the typical diffraction pattern of island growth on the GaAs surface. The samples were grown in an As-enriched environment with an As flux approximately twice that required that a 2×4 RHEED pattern be sustained during GaAs growth. Luminescence was excited by an Ar^+ laser ($\lambda=514.5$ nm, $P=0.4$ W) and recorded by a germanium photodiode.

RESULTS AND DISCUSSION

During this study we investigated the influence of the operating regime of the nitrogen source and the growth rate (determined by the Ga flux) on the implantation of nitrogen in epitaxial GaAsN layers. We established that by using relatively high microwave discharge powers ($\sim$150 W), nitrogen can be efficiently implanted into the growing layer and high nitrogen concentrations (up to $\sim$12 %) can be obtained at the growth rates used. However, during the growth process the RHEED pattern typical of planar GaAs growth gradually changes to a pattern consisting of points distributed at the main peaks, which corresponds to the formation of a microscopically rough surface. When the baffles to the sources of the third group of elements were shut, the RHEED pattern corresponding to ($\times4$) surface reconstruction changed to a pattern with ($\times3$) reconstruction, which is typical of the formation of a surface layer with a high nitrogen content. At low microwave powers supplied to the source ($\sim$25 W) and a growth rate of 0.7 μm/h, growth took place under ($\times4$) surface reconstruction conditions and the nitrogen concentration in the epitaxial layers decreased to 2%. When the sources of the group III elements were shut off, the RHEED pattern remained the same. We observed that a reduction in the growth rate from 0.7 to 0.4 μm/h ($P=25$ W) doubled the nitrogen content in the layers (to 4%) while the As flux remained the same. This result clearly indicates that there are

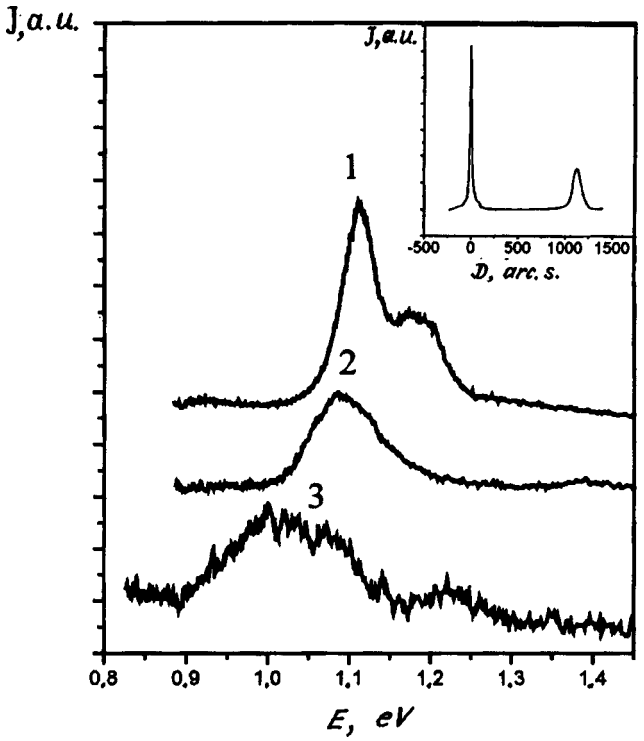

FIG. 1. Photoluminescence spectra of $GaAs_{1-x}N_x$ layers 0.2 μm thick grown on GaAs(100) substrates. The inset shows the x-ray rocking curve (near the 004 reflection) for $GaAs_{1-x}N_x$, $x=0.02$: D is the diffraction angle; *1* — $x=0.02$, 77 K, *2* — $x=0.02$, 300 K, and *3* — $x=0.04$, 77 K.

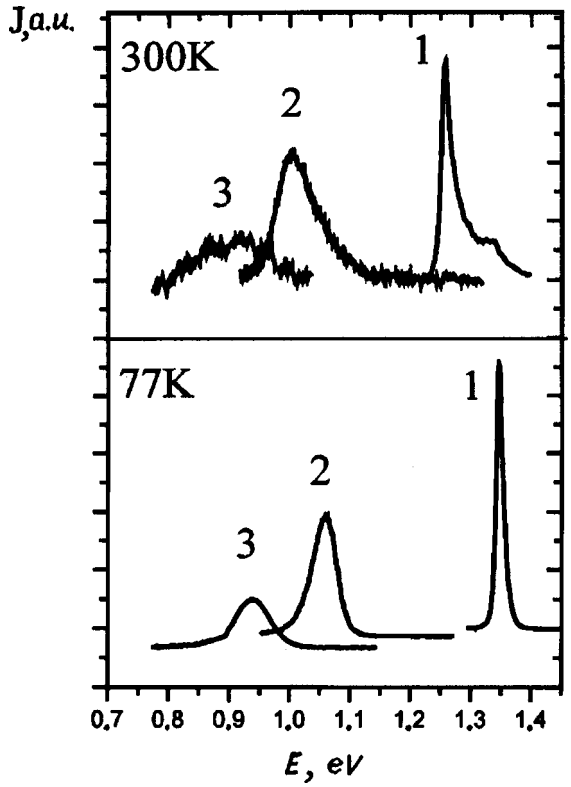

FIG. 2. Photoluminescence spectra of $In_yGa_{1-x}As_{1-x}N_x$/GaAs quantum wells at 300 and 77 K. *1* — $y=0.20$, $x=0$, quantum-well width 10 nm, *2* — $y=0.20$, $x=0.02$, 10 nm, and *3* — $y=0.28$, $x=0.03$, 7 nm.

substantial differences in the mechanisms for implantation of N and As atoms in GaAsN epitaxial layers grown by molecular beam epitaxy.

Figure 1 shows the photoluminescence spectra of the GaAsN layers studied here. The $GaAs_{0.98}N_{0.02}$ layer exhibits a high photoluminescence intensity at room temperature and liquid-nitrogen temperature. The presence of two peaks (1.11 and 1.18 eV) in the spectrum measured at 77 K may be attributed to variability in the distribution of the solid-solution composition, i.e., local regions enriched in nitrogen. This interpretation is also supported by the presence of only one peak in the spectra measured at room temperature and at 77 K after the sample was annealed in the growth chamber in an As flux at 700°C.

Despite these variations, the material exhibits fairly high structural perfection, as is illustrated by the x-ray rocking curve (inset to Fig. 1). The maximum of the rocking curve peak corresponding to the GaAsN layer is positioned at 1130 arc s from the substrate peak and has a half-width of 97 arc s. An increase in the nitrogen concentration in the solid solution reduces the photoluminescence intensity (Fig. 1), no photoluminescence signal can be recorded in the $GaAs_{0.96}N_{0.04}$ layer at room temperature, and the $GaAs_{0.88}N_{0.12}$ layer exhibits no photoluminescence even at low temperatures. The behavior is evidently caused by the formation of mismatch dislocations in an elastically strained layer of thickness exceeding the critical value. Thus, the longest emission wavelength that can be obtained from GaAsN layers at room temperature is 1.12 μm, which agrees with the data given by Francoeur *et al.*[4]

By using InGaAsN/GaAs quantum wells, the emission wavelength can be increased appreciably compared with GaAsN layers.[2] Here we investigate the contribution of N and In to the long-wavelength shift of the emission from an InGaAsN solid solution and we demonstrate that the wavelength can be increased to 1.4 μm (300 K) by using quantum wells based on InGaAsN solid solutions. Figure 2 shows photoluminescence spectra of heterostructures with $In_{0.20}Ga_{0.80}As_{0.98}N_{0.02}$ (100 Å), $In_{0.28}Ga_{0.72}As_{0.97}N_{0.03}$ (70 Å), and $In_{0.20}Ga_{0.80}As$ (100 Å) quantum wells at room temperature and liquid-nitrogen temperature.

It can be seen that the addition of 2% N to an $In_{0.20}Ga_{0.80}As$ solid solution can increase the emission wavelength of the quantum well to 286 meV (77 K) and 257 meV (300 K). The large half-width of the peaks of the four-component solid solutions and the weaker temperature dependence of the energy position of the peak are clearly caused by the presence of states associated with local inhomogeneities in InGaAsN. A simultaneous increase in the In and N content in the solid solution can shift the emission even further in the long-wavelength range and yield a photoluminescence signal with a maximum at 1.4 μm (300 K).

The photoluminescence intensity of structures with InGaAsN quantum wells decays rapidly as the nitrogen content increases and is considerably inferior to (In, Ga)As structures, so that further work is required to optimize the growth regimes of InGaAsN/GaAs structures to reduce the concentration of defects and nonradiative recombination centers. However, the relatively high photoluminescence intensity of

a thick GaAsN layer with a 2% nitrogen content and also the results of x-ray measurements indicate that the structural quality of the grown solid solution is fairly high. Thus, one method of further increasing the emission wavelength of nitrogen-containing heterostructures grown on GaAs substrates and also of enhancing the intensity of the luminescence signal is to use GaAs–GaAsN–GaAsInN–GaAsN–GaAs heterostructures, in other words, to insert GaInAsN quantum wells in a GaAsN matrix containing no more than 2–3% nitrogen.

CONCLUSIONS

Molecular beam epitaxy has been used to grow GaAsN/GaAs and InGaAsN/GaAs heterostructures. The influence of the microwave power of the nitrogen source and the growth rate on the characteristics of GaAsN layers has been studied. It has been demonstrated that 1.4 μm emission can be obtained at room temperature, which is extremely promising for the fabrication of GaAs devices for fiber-optic communication lines.

This work was supported by the ''Physics of Solid-State Nanostructure'' Program of the Ministry of Science and Technology of the Russian Federation.

[1] M. Kondow, K. Uomi, A. Niwa, T. Kitatani, S. Watahiki, and Y. Yazawa, Jpn. J. Appl. Phys. **35**, 1273 (1996).
[2] H. P. Xin and C. W. Tu, Appl. Phys. Lett. **72**, 2442 (1998).
[3] K. Nakahara, K. Kondow, T. Kitatani, Y. Yazawa, and K. Uomi, Electron. Lett. **32**, 1585 (1997).
[4] S. Francoeur, G. Sivaraman, Y. Qiu, S. Nikishin, and H. Temkin, Appl. Phys. Lett. **72**, 1857 (1998).

Translated by R. M. Durham

Temperature–composition–degree of compositional ordering phase diagram of lead scandoniobate–scandotantalate solid solutions

I. P. Raevskiĭ, V. V. Eremkin, V. G. Smotrakov, E. S. Gagarina, and M. A. Malitskaya

Research Institute of Physics, Rostov State University, Rostov-on-Don
(Submitted May 14, 1998)
Pis'ma Zh. Tekh. Fiz. **24**, 88–93 (December 12, 1998)

It was established that the temperature of the ferroelectric phase transition in crystals of compositionally ordered solid solutions of lead scandoniobate—scandotantalate with high and low degrees of ordering S depends linearly on the composition x. These data were used to calculate the $T-x-S$ phase diagram of these solid solutions for the first time. © *1998 American Institute of Physics.* [S1063-7850(98)01612-7]

Solid solutions of ternary oxides in the perovskite family, which possess ferroelectric properties, form the basis of numerous functional materials, including piezoelectric, capacitor, pyroelectric, electrostrictive, electrocaloric, and electrooptic.[1–4] In some ternary oxides of the $PbB^{3+}_{0.5}B^{5+}_{0.5}O_3$ type (B^{3+} = Sc, In, Yb, Lu, Tm; B^{5+} = Nb, Ta), in addition to ferroelectric phase transitions, compositional order–disorder phase transitions also occur at high temperatures[1,5] ($T_i = 1000-1500\,^\circ$C). Above T_t ions of trivalent and pentavalent elements are distributed randomly over intraoctahedral lattice sites, whereas below this temperature the ordered state is in equilibrium (compositional or crystal-chemical ordering). Since any change in the degree S of compositional ordering is achieved by diffusion, fairly rapid cooling of the sample after annealing may ''freeze'' the high-temperature state and produce a material with an intermediate degree of ordering.

This opens up very extensive possibilities for controlling the properties of materials (which depend very weakly on S) by varying the preparation conditions without changing their composition. However, no data are available on the properties of solid solutions of compositionally ordered oxides as a function of S. In particular, the temperature (T)–composition (x) phase diagrams constructed for several systems of these solid solutions,[3,4,6,7] cannot be considered to be reliable since compositions with different x had different values of S. Any change in the sample preparation conditions or subsequent heat treatment leads to substantial changes in the $T-x$ diagrams.[3,7] It is therefore of interest to construct $T-x$ phase diagrams of compositionally ordered solid solutions allowing for the dependence of the phase transition temperatures on S ($T-x-S$ diagrams). Our aim was to obtain these data for a binary system of mutual solid solutions of lead scandoniobate $PbSc_{0.5}Nb_{0.5}O_3$ (PSN) and lead scandotantalate $PbSc_{0.5}Ta_{0.5}O_3$ (PST), which are promising for many applications.[1–3]

Unlike previous investigations of compositionally ordered solid solutions which were only carried out for ceramic samples, here we study crystals because the scope for variation of S in crystals is considerably greater than that in ceramics.[8,9] The method of growing and investigating $PbSc_{0.5}(Nb_{1-x}Ta_x)_{0.5}O_3$ crystals was described in Ref. 10. Dielectric and optical investigations of crystals with high values of S ($S = 0.90-0.95$) showed that the temperature T_C of the ferroelectric–paraelectric phase transition depends approximately linearly on x (Fig. 1). Changing the value of S

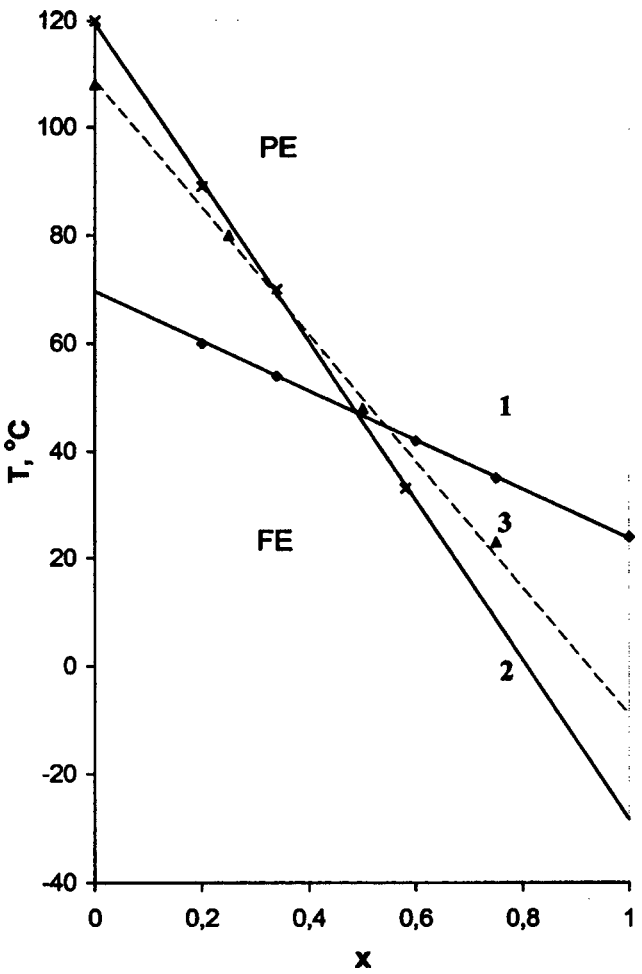

FIG. 1. $T-x$ phase diagrams of $PbSc_{0.5}(Nb_{1-x}Ta_x)_{0.5}O_3$ solid solutions constructed using data for crystals (*1*, *2*) and ceramic samples (*3*): FE — ferroelectric phase, PE — paraelectric phase; *1* — ordered crystals ($S = 0.90-0.95$), *2* — disordered crystals ($S < 0.2$), and *3* — disordered ($S < 0.2$) ceramic samples (data from Refs. 2 and 5).

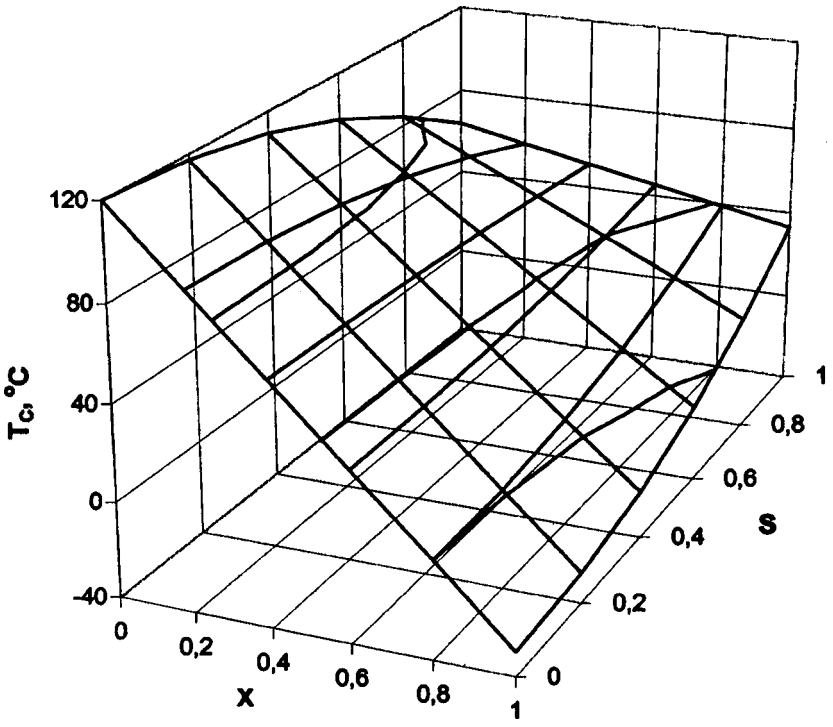

FIG. 2. $T-x-S$ phase diagram of $PbSc_{0.5}(Nb_{1-x}Ta_x)_{0.5}O_3$ solid solutions constructed using data from Fig. 1.

for the crystals by high-temperature annealing revealed that for solid solutions with large and small x, the dependence $T_c(S)$ is the same as that for the corresponding end components: $dT_C/dS>0$ for $x>0.6$ and $dT_C/dS<0$ for $x<0.4$. The dependence $T_C(x)$ plotted for the most disordered crystals ($S<0.2$) is also close to linear (Fig. 1). This agrees with the behavior of $T_C(x)$ for ceramic samples constructed using data[2] for several compositions of PSN–PST solid solutions annealed above T_t (Fig. 1).

Extrapolating the curve $T_C(x)$ for crystals to $x=1$ gives $T_C=-30$°C for disordered PST, which is lower than the values quoted in the literature,[5,8,11] although these cannot be regarded as sufficiently reliable. The accuracy of our $T-x$ diagrams constructed for ordered and disordered PSN–PST solid solids is evidenced by the fact that they intersect at $x<0.5$. Since compositions on either side of the point of intersection x_0 have different signs of dT_C/dS, T_C for a composition with $x=x_0$ should not depend on S. Data given by Chen *et al.*[2] indicate that T_C for a ceramic with $x=0.5$ increases as S increases from 0 to 0.7, although this change is very small. This suggests that x_0 is slightly less than 0.5, which agrees well with our results. Thus, unlike other known systems of solid solutions of compositionally ordered ternary perovskites, where $T_C(x)$ has a minimum,[4,6,7,12] the values of T_C for disordered and ordered PSN–PST solid solutions vary approximately linearly with x. This difference may arise because PSN and PST are ferroelectric in the disordered and ordered states, whereas other compositionally ordered ternary perovskites are ferroelectrics in the disordered state and antiferroelectrics in the ordered state.[12]

The thermodynamic model[13] indicates that T_C for compositionally ordered ferroelectrics depends quadratically on S, $T_C(S)=T_c(0)-AS^2$, where A is a phenomenological parameter and $T_C(0)$ is the value of T_C for $S=0$. These results were used to determine the values of A for various compositions and to construct the dependence $T_C(x,S)$, i.e., the $T-x-S$ phase diagram for PSN–PST solid solutions (Fig. 2).

These relationships can be used to predict changes in the $T-x$ phase diagrams of compositionally ordered solid solutions as a function of S and can appreciably reduce the number of experimental investigations required to optimize the preparation regimes of new materials.

This work was partially supported by the Russian Fund for Fundamental Research, Project No. 96-02-17 463.

[1] L. E. Cross, Ferroelectrics **76**, 241 (1987).
[2] Zhili Chen, N. Setter, and L. E. Cross, Ferroelectrics **37**, 619 (1981).
[3] L. A. Shebanov, E. H. Birks, and K. J. Borman, Ferroelectrics **90**, 165 (1989).
[4] V. A. Isupov, E. N. Isupova, N. Yu. Sokolova *et al.*, Neorg. Mater. **20**, 825 (1984).
[5] C. G. F. Stenger and A. J. Burgraaf, Phys. Status Solidi A **61**, 653 (1980).
[6] I. M. Danilenko, E. D. Politova, and Yu. N. Venevtsev, Neorg. Mater. **23**, 1192 (1987).
[7] A. A. Bokov, I. P. Raevskiĭ, and V. Yu. Shonov, Neorg. Mater. **26**, 2371 (1990).
[8] I. P. Raevskiĭ, V. G. Smotrakov, A. A. Bokov *et al.*, Neorg. Mater. **22**, 807 (1986).
[9] A. A. Bokov, I. P. Rayevskii, V. G. Smotrakov *et al.*, Phys. Status Solidi A **93**(2), 411 (1986).
[10] V. Eremkin, V. Smotrakov, E. Gagarina *et al.*, J. Phys. III **32**, S1597 (1998).
[11] L. S. Kamzina, N. N. Kraĭnik, L. M. Sapozhnikova *et al.*, Pis'ma Zh. Tekh. Fiz. **14**, 1760 (1988) [Sov. Tech. Phys. Lett. **14**, 764 (1988)].
[12] A. A. Bokov and I. P. Rayevsky, Ferroelectrics **144**, 147 (1993).
[13] A. A. Bokov, I. P. Raevskiĭ, and V. G. Smotrakov, Fiz. Tverd. Tela (Leningrad) **25**, 2025 (1983) [Sov. Phys. Solid State **25**, 1168 (1983)].

Translated by R. M. Durham

Field reconstruction of close-packed atomic complexes at the surface of tungsten

T. I. Mazilova

Research and Design Institute of Vacuum Machine Construction, Kharkov, Ukraine
(Submitted April 27, 1998)
Pis'ma Zh. Tekh. Fiz. **24**, 1–6 (December 26, 1998)

The observation of low-temperature reconstruction of atomic clusters at a close-packed metal face using field ion microscopy is reported. An analysis is made of the configuration of nonclose-packed zigzag atomic chains formed as a result of the decay of clusters.
 [S1063-7850(98)01712-1]

The phenomenon of low-temperature evaporation of metals in strong electric fields is used to form sharp microtips for scanning tunneling microscopes, atomic force microscopes, and other types of scanning probe microscopes.[1,2] Field evaporation is used to produce tips with an ideal, atomically smooth surface and local radii down to a few nanometers at the apex, which can give atomic resolution and stable emission characteristics. Detailed information on the configuration of atomic complexes at the apex of tips, where the tunnel emission is localized, is required to ensure reliable interpretation of atomic probe images and reproducible operating parameters for nanotechnological devices based on them. In particular, difficulties in the determination of surface atoms may be associated with surface relaxation and reconstruction effects. These effects have been studied fairly comprehensively at the surface of macroscopic objects by low-energy electron diffraction,[3] but virtually no information is available on the specific nature of atomic relaxation in surface nanoclusters. The present paper reports an investigation of the low-temperature reconstruction of atomic complexes at the {110} close-packed face of tungsten microcrystals in strong electric fields.

The investigations were carried out using a two-chamber field ion microscope with liquid-hydrogen and liquid-nitrogen cooled samples. The residual gas pressure in the working chamber was $10^{-7}-10^{-6}$ Pa. Helium at pressures of $10^{-3}-10^{-2}$ Pa was used as the imaging gas. Samples oriented in the [110] direction, having radii of curvature between 4.5 and 50 nm, were prepared by electrochemical etching and subsequent field evaporation. Field evaporation was achieved by applying a positive dc potential or a pulsed potential in the range 1–25 kV. The pulse length was 0.25 μs and the rise time was 0.05 μs. The rate of evaporation in the dc regime was 0.1–0.01 atomic layers (110) per second. Pulsed evaporation at a rate of 10^5-10^7 sheet/s was achieved at a field strength 12–14% higher than the threshold for evaporation in the dc regime.

The rate of evaporation of atoms from steps of the (110) faces of microcrystals with radii of curvature at the apex greater than 15 nm increased sharply as the size of the atomic complex decreased. Figure 1 (curve *1*) gives the reduced rate of evaporation ν/ν_0 as a function of the number of atoms N in the complex at the (110) face of a microcrystal of radius 22 nm. The instantaneous ν and initial ν_0 rates of evaporation are defined as dN/dt, where t is the time. The rate ν_0 was measured directly after evaporation of the previous atomic layer.

Note that when these nanocomplexes evaporate, the high packing density, which shows up particularly clearly in the absence of atomic resolution and variations in the contrast of the image at the inner sections of the faces, still remains. The number of atoms in the complexes was calculated from the surface area occupied by them. The geometric model of surface formation by field evaporation[4] directly indicates that the rate of field evaporation may increase as the step radius of the face decreases, but it is easy to show that the geometric effect is at least an order of magnitude smaller than the observed effect.[5] A similar effect was observed as a result of pulsed evaporation of microcrystals having radii of curvature in the range under study, 15–50 nm.

As a result of the sharp increase in the rate of evaporation, no field evaporation could be identified in any of one thousand experiments after the nanocomplex had reached a size of around ten atoms. This appreciably limits the attainable localization of the interaction between the working part of the microtip of a scanning tunneling microscope and the surface being studied or treated. However, when the radii of the tips were reduced to 12–15 nm, this accelerated evaporation under application of a dc voltage disappeared almost completely: only a relatively small increase in ν/ν_0 was observed as the size of the complex decreased (Fig. 1, curve *2*) as a result of the constraint that the evaporated surface remained spherical. In the pulsed regime, accelerated field evaporation was observed (Fig. 1, curve *3*) over the entire range of radii of curvature, 4.5–50 nm.

During evaporation of tips of less than 10 nm radius in the dc regime, voltage dumping during visual monitoring of the process produced atomic complexes of small dimensions, down as far as monatomic. After the size of the complexes had reached around ten atoms during evaporation, the complexes became unstable, and initially circular, close-packed groups of atoms (Fig. 2a) decayed into zigzag chains (Fig. 2b). An analysis of the configurations of the zigzag chains revealed that they have a constant width of 0.32 ± 0.05 nm. The average chain width was determined by calculating the radius of curvature for the section between the exits of the $\langle 110\rangle$ and $\langle 321\rangle$ poles, and the linear dimensions of the

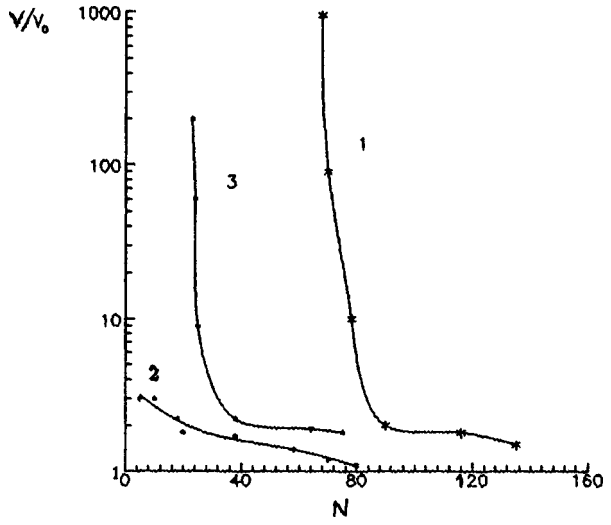

FIG. 1. Reduced rate of evaporation versus number of atoms in complex at 78 K. Microcrystals having radii of curvature $R=22$ nm (*1*) and $R=11$ nm (*2*) were evaporated at dc voltage; microcrystals with $R=12$ nm (*3*) were evaporated in a pulsed regime.

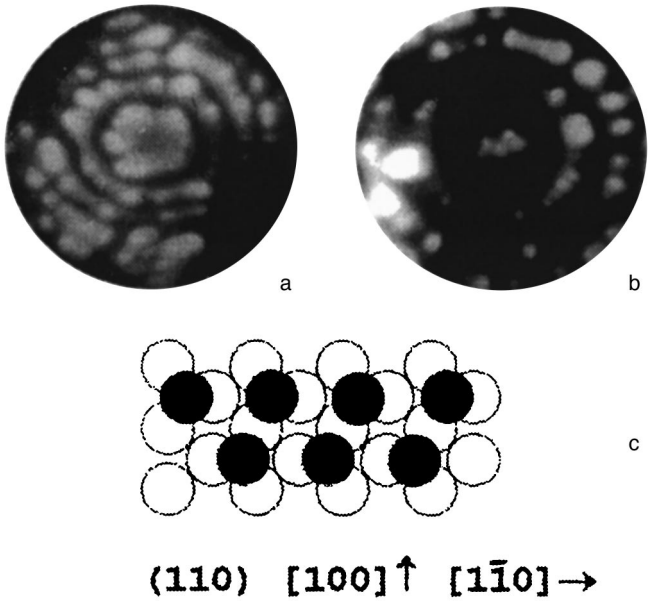

FIG. 2. Formation of zigzag atomic chains during field evaporation of the {110} face (a, b) and configuration of atoms in chain (c).

chains on the image were compared with the distances between the opposite poles of the {211} faces. In the pulsed regime no conversion of close-packed clusters into chains was observed, regardless of the sizes of the crystallites.

The configuration of the chains corresponded to the complexes observed previously at {110} faces, which were formed as a result of the combined action of heat and field.[6] An analysis of configurations of the order of 10° zigzag chains revealed that the links are formed by pairs of atoms. The angles between neighboring links are directly determined with an accuracy of less than 10° because of the partial overlap of the atomic images. However, the angles can be calculated with allowance for the width, length, and number of atoms in the zigzag chains. These calculations show that the angles between neighboring links (pairs of atoms) on the ion-microscope images vary continuously as the chain length decreases. The links of chains of 9–10 atoms are oriented in the $\langle 113\rangle$ directions to within measurement error. As evaporation proceeds and the chains become shorter, the angle between neighboring atoms increased continuously and reached $(60\pm5)°$. The continuous change observed in the angles between neighboring atomic dumbbells on the ion-microscope images cannot reflect the real distribution of metastable positions of atoms on the close-packed {110} face.

Muller and Tsong[4] showed that in strong electric fields, atoms can migrate from sites in the bulk crystal lattice to metastable positions which correspond to the configuration of a surface atom above a triangle of lower-lying atoms. The continuous variation of the angles on the ion-microscope images is caused by a nonuniform local increase above nonaxisymmetric protrusions on the surface. As the chain length decreases, the principal radii of curvature of the perturbed section of the effective electron surface become equalized and the anisotropy of the microscope magnification decreases.[7] The results of an analysis of ion-microscope images of nonaxisymmetric samples[7] indicate that the angle between pairs of atoms on the images increases, approaching the real angle between the links of the zigzag chains. Figure 2c shows the configuration of atoms in this type of complex. The observation of the formation of nonclose-packed atomic complexes up to 20 K indicates that the atoms may undergo a shift essentially without activation over distances substantially greater than the shortest distance between the stable and metastable positions of the surface atoms.[4] This effect may be caused by electric-field-induced dipole–dipole repulsion of atoms[3] near nanocluster steps.

In conclusion, the author would like to than I. M. Mikhaĭlovskiĭ for interest in this work and useful discussions.

[1] S. N. Magonov and M.-H Whangbo, *Surface Analysis with STM and AFM* (Springer-Verlag, Berlin, 1996, 450 pp.).
[2] V. A. Ksenofontov, J. M. Mikhailovskij, V. M. Shulaev *et al.*, in *Physics, Chemistry, and Application of Nanostructures*, edited by V. E. Borisenko *et al.* (Belarussian State University of Informatics and Radioelectronics Press, Minsk, 1995), pp. 244–245.
[3] M. A. Vasil'ev, *Stucture and Dynamics of the Surface of Transition Metals* [in Russian], Naukova Dumka, Kiev (1988), 245 pp.
[4] E. W. Muller and T. T. Tsong, *Field Ion Microscopy* (Elsevier, New York, 1969; Metallurgiya, Moscow, 1972, 360 pp.).
[5] I. M. Mikhaĭlovskiĭ, Zh. I. Dranova, V. A. Ksenofontov *et al.*, Zh. Éksp. Teor. Fiz. **76**(4), 1309 (1979) [Sov. Phys. JETP **49**, 664 (1979)].
[6] S. Nishigaki and S. Nakamura, Jpn. J. Appl. Phys. **14**, 769 (1975).
[7] I. M. Mikhaĭlovskiĭ and V. S. Geĭsherik, Radiotekh. Elektron. **19**(7), 1490 (1974).

Translated by R. M. Durham

Influence of the step height of the vicinal surface of germanium on the formation of antiphase boundaries in a gallium-arsenide–germanium–gallium-arsenide(001) system

A. K. Gutakovskiĭ, A. V. Katkov, M. I. Katkov, O. P. Pchelyakov, and M. A. Revenko

Institute of Semiconductor Physics, Siberian Branch of the Russian Academy of Sciences, Novosibirsk
(Submitted April 16, 1998)
Pis'ma Zh. Tekh. Fiz. **24**, 7–12 (December 26, 1998)

An investigation was made of the formation of antiphase boundaries in a GaAs/Ge/GaAs(001) system using accurately oriented substrates and substrates misoriented by 3° and 5° in the [110] direction. It was shown that growth of germanium on a misoriented gallium arsenide surface leads to the formation of diatomic steps of height $a_0/2$ and therefore results in the absence of any antiphase boundaries in a GaAs film grown on this surface. Conditions required to obtain a vicinal Ge surface consisting of monatomic steps of height $a_0/4$, whose presence leads to the formation of antiphase boundaries during GaAs growth, are determined.
 [S1063-7850(98)01812-6]

The ability to grow structurally perfect films of polar III–V semiconductors on nonpolar germanium and silicon substrates can substantially improve various semiconductor devices and can also solve the technological problem of matching III–V optoelectronic devices with silicon technology. For instance, an almost ideally (0.07%) lattice-matched GaAs/Ge heterosystem can be used to fabricate a new type of solar cell[1] and also for fabricating heterobipolar transistors.[2] The main structural defects during epitaxial growth of pseudomorphic layers of gallium arsenide on a Ge(001) surface are antiphase boundaries,[3] but although a fair amount of literature has been published the mechanism for their formation is not completely understood. The aim of the present study is to investigate the influence of submonolayer gallium coatings on the step height on the vicinal Ge(001) surface and also to examine the influence of the step height on the concentration of antiphase boundaries in gallium arsenide grown on a misoriented Ge(001) surface.

In order to investigate the formation of antiphase boundaries in a GaAs/Ge/GaAs(001) system, we grew Ge films on GaAs(001) substrates misoriented by 3° and 5° in the [110] direction, and then grew a GaAs film on the Ge by molecular beam epitaxy. The GaAs and Ge layers were grown using standard effusion-type molecular sources. The GaAs growth rate was 0.5 μm/h and the Ge growth rate 0.2–0.3 μm/h. The substrate temperature was varied between 200 and 600 °C. The growth process was monitored by 30–40 keV high-energy electron diffraction. The GaAs was grown using arsenic to stabilize the surface and giving a 2×4 reconstruction. The change in the step height (Fig. 1) during growth on misoriented GaAs(001) substrates was recorded by observing the splitting of the peak on the diffraction pattern in the azimuth parallel to the direction of the steps.[4] A flux of gallium atoms with flux density $\sim5\times10^{11}\,\mathrm{cm^{-2}\,s^{-1}}$ was supplied to the germanium surface during growth in order to investigate the influence of the Ga molecular beam on the step height of the vicinal face. The structure of the GaAs films was investigated by transmission electron microscopy using a JEM-4000 EX electron microscope. The samples were prepared in the form of thin foils parallel to the growth surface using a standard chemical jet etching technique.

After the Ge molecular source had been opened for a time sufficient to grow approximately one Ge monolayer on exactly (001) oriented GaAs substrates, a 2×2 surface reconstruction was observed. This is interpreted as a mixed 2×1 and 1×2 reconstruction, which arises because the surface consists of steps of monatomic height $a_0/4$ (Ref. 5). Before growth of GaAs on Ge was initiated, the sample was heated to the epitaxy temperature ($T\approx550$ °C) in an As_4 beam. The onset of gallium arsenide growth was characterized by the rapid establishment of the 4×4 reconstruction, which is a mixture of 2×4 reconstructions, typical of the existence of antiphase domains.[3,5] This reconstruction was maintained throughout the entire growth process. The observation of 4×4 reconstruction may indicate that the GaAs film contains a mixture of 2×4 and 4×2 domains and thus indicates the presence of antiphase domains. This conclusion is confirmed by transmission electron microscopy. In Fig. 2 these domains resemble closed regions of arbitrary geometry separated by antiphase boundaries which exhibit a striped black–white contrast, typical of inclined interfaces.

The growth of Ge on the misoriented GaAs substrates was accompanied by the formation of steps of height $a_0/2$, which was deduced from observing the splitting of the principal peaks of the diffraction pattern in the azimuth parallel to the steps (Figs. 1a and 1b). Since after the onset of germanium growth the separation between the split peaks remained the same in our case, we can conclude that the height of the germanium steps corresponds to $a_0/2$. Calculations of the terrace width from the splitting of the peaks for substrates misoriented by 5° also gave ~3 nm, which agrees with the calculations made using the angle of misorientation for a step height of $a_0/2$. It should be noted that the surface of the

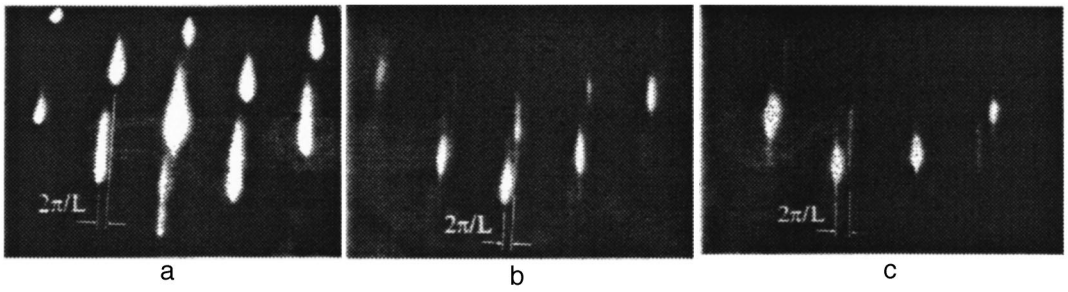

FIG. 1. Changes in the splitting of the peaks of the high-energy electron diffraction pattern in the ⟨100⟩ azimuth: a — GaAs, b — Ge on GaAs, c — Ge on GaAs after deposition of Ga; L is the distance between the edges of the steps.[4]

growing germanium film clearly contains both diatomic and monatomic steps and the fraction of these depends on the growth temperature. This is also indicated by the fact that a 1/2 fractional peak was always observed in the 110 azimuth perpendicular to the steps, whereas in the [110] azimuth the intensity of the 1/2 fractional peak decreased appreciably with increasing growth temperature. This shows good agreement with the data reported by Pukite *et al.*[4]

The growth of GaAs on the germanium surface formed by steps of height $a_0/2$ started immediately with the formation of a 2×4 reconstruction, which was maintained throughout the entire growth process. This indicated that no antiphase boundaries were formed. Investigations carried out using transmission electron microscopy also reveal no antiphase boundaries in the gallium arsenide film grown on the germanium surface consisting of $a_0/2$ steps. It should also be noted that in this case, unlike in Ref. 3, the growth of gallium arsenide on germanium was accompanied by rotation of the 2×4 surface reconstruction through 90° relative to the substrate.

We also observed that when a submonolayer coating of gallium atoms was present on the surface, the step height changed from $a_0/2$ to $a_0/4$ during the germanium growth. In our case, when germanium was grown on a misoriented GaAs substrate, a transition from diatomic steps to predominantly monatomic ones was observed after the Ga flux had been supplied for around 20–40 s. In this case, the substrate temperature was 400 °C. The change in the step height was identified from the diffraction pattern in the [110] azimuth parallel to the steps. Figure 1c shows that the formation of monatomic steps resulted in the distance between the split peaks being doubled. When the Ge growth was then terminated and the sample cooled, the monatomic steps remained on the surface. The possibility of obtaining a vicinal Ge(001) surface consisting of monatomic or diatomic steps allows us to determine how the step height influences the concentration of antiphase boundaries in the GaAs film during its subsequent growth on germanium. Growth of germanium on a vicinal germanium surface consisting of monatomic steps resulted in the formation of antiphase boundaries. In this case, the pattern of antiphase domains observed by transmission electron microscopy is similar to that shown in Fig. 2, but the average size of the domains was several times smaller than that during the growth of a singular surface. The density of the antiphase boundaries was thus several times higher.

FIG. 2. Image of antiphase boundaries in a GaAs/Ge/GaAs(001) system obtained by transmission electron microscopy.

From this reasoning we can conclude that the antiphase boundaries in a GaAs/Ge/GaAs(001) system form mainly because of the presence of $a_0/4$ steps on the germanium surface. It has been shown that when germanium grows on GaAs substrates misoriented by 3° and 5° in the [110] direction, diatomic steps form and gallium arsenide grows subsequently without the formation of antiphase boundaries. A transition from diatomic to monatomic steps was identified when an additional Ga flux was applied during growth. A transmission electron microscope analysis of gallium arsenide grown on a germanium surface consisting of monatomic steps reveals a high density of antiphase boundaries, whereas growth on a misoriented germanium surface consisting of diatomic steps results in no antiphase boundaries in the gallium arsenide film.

The investigations were carried out as part of the ''Astronomy: Fundamental Space Research'' (Epitaxy Project) and ''Physics of Solid-State Nanostructures'' State Programs of the Ministry of Science (Projects Nos. 97-20-25 and 3-011/4).

[1] S. P. Tobin, S. M. Vernon, and C. Bajgar, IEEE Electron Device Lett. **9**, 256 (1988).
[2] S. Strite, M. S. Unlu, and A. L. Demirel, J. Vac. Sci. Technol. B **10**, 675 (1992).
[3] S. Strite, D. Biswas, K. Adomi, and H. Morkoç, J. Appl. Phys. **67**, 1609 (1990).
[4] P. R. Pukite, P. I. Cohen, and S. Batra, in *Reflection High-Energy Electron Diffraction and Reflection Imaging of Surfaces*, edited by P. K. Larsen and P. J. Dobson (Plenum Press, New York, 1988).
[5] S. Strite, D. Biswas, N. S. Kumar *et al.*, Appl. Phys. Lett. **56**, 244 (1990).

Translated by R. M. Durham

Influence of desorption on the composition of high-temperature superconducting thin films during magnetron sputtering

A. K. Vorob'ev, S. V. Gaponov, M. N. Drozdov, E. B. Klyuenkov, V. I. Luchin, and D. V. Masterov

Institute of Microstructure Physics, Russian Academy of Sciences, Nizhniĭ Novgorod
(Submitted July 6, 1998)
Pis'ma Zh. Tekh. Fiz. **24**, 13–18 (December 26, 1998)

Results are presented of investigations to study how desorption caused by interaction between the surface of condensation and the plasma particles affects the composition of thin films of Y–Ba–Cu–O high-temperature superconductors during magnetron sputtering. An analysis of the current–voltage characteristics of Langmuir probes was used to determine the floating potential of the substrate at various working gas pressures. Electron Auger spectroscopy was used to determine the atomic composition of films obtained at various substrate bias voltages. It was established that during magnetron sputtering of Y–Ba–Cu–O films the formation of the condensate composition may be strongly influenced by selective desorption of components from the substrate and the surrounding structural elements as a result of bombardment by plasma ions accelerated in the floating potential field. [S1063-7850(98)01912-0]

An important trend in the technology of high-temperature superconducting thin films is to enhance their homogeneity. Inhomogeneities on 0.01–1 μm scales are caused by the presence of nonsuperconducting secondary-phase particles in the films, which are highly undesirable for most applications. Secondary-phase particles appear in superconducting films during *in situ* growth as a result of deviations of the condensate composition from stoichiometry. It is known[1] that during magnetron sputtering of multicomponent materials, the transfer of the composition from the target to the substrate may be impaired for the following reasons: 1) changes in the composition of the multicomponent target as a result of diffusion of the components from the bulk to the modified surface layer; 2) selective scattering of sputtered atoms by the working gas; and 3) selective desorption of components from the surface of condensation.

Preliminary investigations show that during *in situ* growth of thin films of Y–Ba–Cu–O (YBCO) high-temperature superconductors in an inverted magnetron sputtering system, the composition of the condensate is substantially influenced by all three processes.[2] Here we report results of investigations to study how desorption caused by interaction between the surface of condensation and the plasma particles influences the formation of the composition of YBCO thin films during magnetron sputtering. We investigated YBCO films around 20 nm thick obtained at various substrate bias voltages. The design and operating characteristics of the inverted magnetron sputtering system were described in detail in Ref. 3. In order to eliminate the influence of thermal activation of desorption examined in detail by Drozdov *et al.*[4] the films were sputtered without being heated to the epitaxy temperature.

The atomic composition of the films was determined by electron Auger spectroscopy using an ÉSO-3 spectrometer. For each film we recorded the composition of the layer at a depth of 10 nm after steady-state conditions had been reached during a layer-by-layer Auger analysis when the films were sputtered by 500 eV argon ions at an angle of 46°. We used the Y (126 eV), Ba (600 eV), Cu (920 eV), and O (512 eV) Auger lines and we analyzed the relative changes in the Cu/Y, Cu/Ba, and Ba/Y atomic ratios.

The substrates were 10×10 mm stainless steel plates to which a bias voltage was applied relative to the reference electrode, which was the casing of the device. One of the substrates was used as a planar Langmuir probe to determine the floating potential of the substrate. The plasma temperature near the substrate was determined using a 14×0.1 mm double Langmuir probe.

Figure 1 gives the current–voltage characteristics of the planar Langmuir probe at various working gas pressures. These characteristics are broadly typical and are similar to those described by Raĭzer.[5] The upper kink on the characteristic identifies the plasma potential ($V_s = +1.2$ V relative to the reference electrode). At a certain negative potential, V_f between -1.0 and -1.5 V relative to the plasma potential, the current to the probe disappears. This potential (floating potential) is acquired by an isolated body inserted in the plasma. As the pressure increases from 25 to 47 Pa, the floating potential increases from -1.0 to -1.5 V. In Langmuir probe theory, the increase in the floating potential is attributed to the influence of collisions in the transition regime.[6] An analysis of the characteristics of the double Langmuir probe gives electron temperatures of 0.28, 0.48, and 0.46 eV for pressures of 25, 38, and 47 Pa, respectively.

Figure 2 gives the atomic ratios of the components of YBCO films obtained at a working gas pressure of 38 Pa and various substrate bias voltages. The atomic ratios are normalized to the peaks, which are taken to be the stoichiometric ratios. This method of representing the data can obviate the need to use a standard and allow for changes in the composition caused by the preferential sputtering during a layer-by-layer Auger analysis. Figure 2 shows that at voltages be-

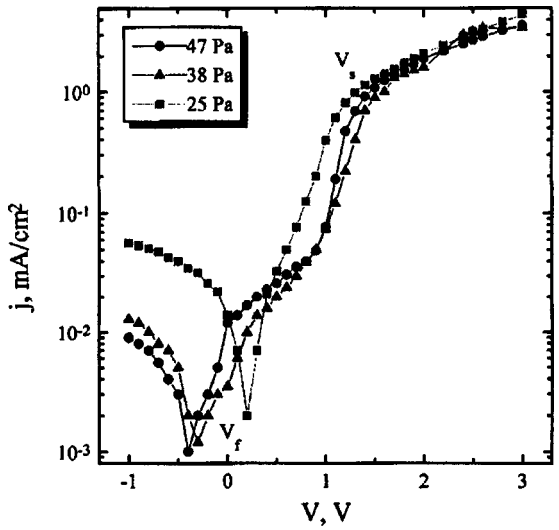

FIG. 1. Current–voltage characteristics of planar Langmuir probe at various working gas pressures.

tween +1.0 and +1.5 V relative to the reference electrode, which correspond to the plasma potential V_s in Fig. 1, the atomic ratios are highest. At these voltages there is no potential difference between the surface of condensation and the adjacent plasma regions. Only thermal ions and electrons reach the growing film. At negative potentials relative to the plasma (to the left of the peaks in Fig. 2), a positive space charge region forms around the substrate. The thermal ions entering this region are accelerated toward the surface of condensation to energies corresponding to the potential difference between the substrate and the adjacent regions of unperturbed plasma. The changes in the composition of the YBCO films (up to 40%) observed in Fig. 2 are evidently caused by selective desorption of copper and barium adatoms from the surface of condensation as a result of bombardment by plasma ions accelerated in the substrate field. Desorption is also caused by the surface of condensation

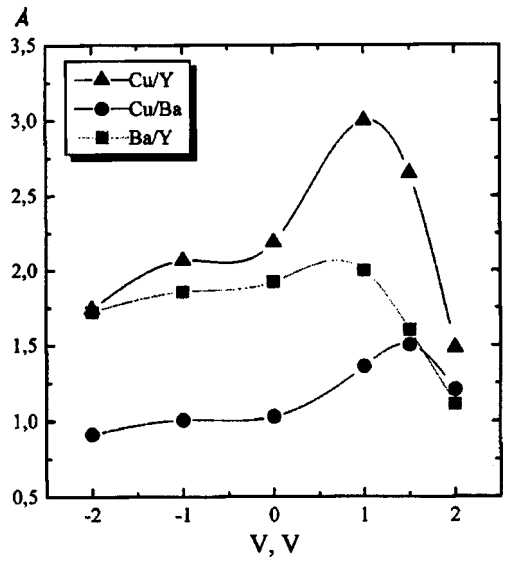

FIG. 2. Atomic ratios (A) of the components of YBCO films obtained at various substrate bias voltages.

being bombarded by electrons accelerated in the substrate field at positive potentials relative to the plasma (to the right of the peaks in Fig. 2), which is confirmed by data presented by Terada *et al.*[7] The main changes in the Cu/Y and Cu/Ba atomic ratios take place at bias voltages up to 0.5 V relative to the plasma potential, which is substantially below the sputtering threshold (17 eV from data given by Maissel and Glang[1]) and corresponds to the binding energy of copper adatoms on a glass substrate (0.14 eV according to Chopra[8]). This confirms our hypothesis that desorption of adatoms influences the formation of the composition of YBCO films during magnetron sputtering.

During *in situ* growth of YBCO films on various dielectric substrates in the presence of a nonequilibrium plasma the surface of condensation is always charged to the floating potential (between −1.0 and −1.5 V in our case). Growth of the films is accompanied by bombardment with plasma ions accelerated in the floating potential field. One of the effects of this bombardment is the selective desorption of adatoms of the components, which substantially changes the composition of the condensate. Moreover, in real sputtering systems various structural elements (components of the substrate holder and parts of the heater) are located in the immediate vicinity of the substrate. These elements may be made of dielectric materials or may be coated with a thick, poorly conducting YBCO film. As a result, the structural surface becomes charged to the floating potential and becomes a source of nonstoichiometric fluxes of desorbed YBCO components which reach the substrate.[2]

To sum up, during magnetron sputtering of thin films of high-temperature superconductors the formation of the condensate composition may be strongly influenced by selective desorption of components (in our case, copper and barium) from the substrate and the surrounding structural elements as a result of bombardment by plasma ions accelerated in the floating potential field.

This work was carried out as part of the ''Topical Directions in the Physics of Condensed Media'' (''Superconductivity'' Project No. 98064) program of the State Committee on Science and Technology and was supported by the Russian Fund for Fundamental Research (Grant No. 96-02-19283).

[1] *Handbook of Thin Film Technology*, edited by L. I. Maissel and R. Glang (McGraw-Hill, New York, 1970; Sov. Radio, Moscow, 1977).
[2] Y. N. Drozdov, S. V. Gaponov, S. A. Gusev *et al.*, in *Extended Abstracts of the International Superconductive Electronics Conference, ISEC'97*, Berlin, 1997, Vol. 2, p. 49.
[3] A. K. Vorob'ev, E. V. Klyuenkov, V. V. Talanov *et al.*, Pis'ma Zh. Tekh. Fiz. **19**(17), 12 (1993) [Tech. Phys. Lett. **19**, 479 (1993)].
[4] Yu. N. Drozdov, S. V. Gaponov, S. A. Gusev *et al.*, IEEE Trans. Appl. Supercond. **7**(2), 1642 (1997).
[5] Yu. P. Raĭzer, *Gas Discharge Physics*, Springer, New York (1991); Nauka, Moscow (1987).
[6] R. H. Kirchhoff, E. W. Peterson, and L. Talbot, Raket. Tekh. Kosmonav. No. 9, 30 (1971).
[7] N. Terada, H. Ihara, J. Masatoshi *et al.*, Jpn. J. Appl. Phys., Part 2, **27**, L639 (1988).
[8] K. L. Chopra, *Thin Film Phenomena* (McGraw-Hill, New York, 1969; Mir, Moscow, 1972).

Translated by R. M. Durham

X-ray optical parameters of a microcapillary lens

Yu. I. Dudchik, N. N. Kol'chevskiĭ, and F. F. Komarov

Belarus State University, Minsk
(Submitted July 3, 1998)
Pis'ma Zh. Tekh. Fiz. **24**, 19–23 (December 26, 1998)

An analysis is made of the possibility of focusing x-rays using a new element in x-ray optics, termed a microcapillary x-ray lens.
[S1063-7850(98)02012-6]

X-ray optics devices which can produce microbeams of x-rays with a photon energy of 10–30 keV are of particular interest for the development of synchrotron technology and high-power microfocus tubes with transmissive or rotating anodes. Snigirev *et al.*[1] suggested that x-rays could be focused by a set of coaxial ordinary biconcave refracting microlenses fabricated from a low atomic number (low-*Z*) material (carbon, polymers). Studies reported in Refs. 1–3 showed that 14 keV and 30 keV x-ray beams from a synchrotron could be focused to a spot a few micrometers in size. The design of these x-ray lenses opens up a whole range of technical realizations: in Refs. 1–3 these lenses were made by drilling 30–40 holes 0.5–1 mm in diameter in an aluminum or polymer plate. The ''necks'' between the holes functioned as the microlenses. However, although a gain of 100 or more is theoretically possible for this type of lens, in practice the gain was only 2–6, which makes it promising to search for other technical realizations for the design of a refracting x-ray lens.

Here we examine a possible design of an x-ray lens (Fig. 1) and calculate its x-ray optical parameters.

We know[4] that a droplet of liquid such as water inserted in a glass microcapillary has the form of a biconcave lens. The surface quality of this lens is fairly high and it can transmit the image of objects in the visible wavelength range. The biconcave shape of the droplet means that it can be used to focus x-rays and by using many such droplets, it is possible to reduce the focal length of the system to around 1 m. The gain G of this system defined as the ratio of the photon flux density of given energy incident on the lens to the flux density at the focus, depends on the capillary radius R and the thickness of the lens (the parameter d in Fig. 1). The shape of the droplet surface in the capillary depends on the surface tension forces at the liquid–glass interface, and to a first approximation can be taken as spherical.

We fabricated a system for focusing x-rays which contained microlenses of various industrial adhesives formed inside a glass capillary. Figure 2 shows a photograph of the lens for which we used two types of adhesive, epoxy adhesive and BF-6 (Ref. 5).

The technology used to fabricate the lens included forming a thin layer of adhesive on the inner surface of the capillary. When the thickness of the film reached a certain value, the spontaneous formation of microdroplets was observed in the capillary. These droplets were distributed fairly regularly. This method can be used to produce 50 or more microlenses in a single capillary.

We established experimentally that for microlenses fabricated by this method using epoxy adhesive (Fig. 2a) there is a relationship between the parameter d and the capillary radius R, which can be approximated by the linear dependence $d=kR+d_0$, where $k=3$, $d_0=-60$ μm.

This dependence $d(R)$ can be used to calculate the x-ray optical parameters of a lens made of epoxy adhesive.

Calculations were made of the size $2f$ of the focal spot (Fig. 1), the transmission of the lens T, which is equal to the ratio of the photon flux at the exit of the lens to that at the entrance, and the gain $G=(0.6R/f)^2T$. The calculations were made by means of a numerical simulation of the trajectories of the x-rays propagating in the system. We assumed that a monochromatic x-ray beam with an angular divergence of 0.01 mrad was incident on the lens and that a diaphragm with an aperture radius of $0.6R$ was placed ahead of the lens to reduce the aberration of the system. The number of lenses was selected to give the focal length $F=1$ m using the following relation from Snigirev *et al.*:[1] $N=R/(2\delta F)$, where δ is the real part of the refractive index of the x-rays in the lens material. The calculations were made for 15 keV photons and various values of the capillary radius R. The coefficient of absorption of the x-rays in the lens material was taken to be 0.82 cm^{-1} and the energy of the electron plasma oscillations was 22 eV.

The results of calculations of the x-ray optical parameters of the microcapillary lens are presented in Table I.

It can be seen that the proposed lens can focus x-rays to a spot of 3–6 μm, amplifying the flux density more than 100 times with a capillary radius of 500–100 μm.

It should be noted that although the gains calculated for

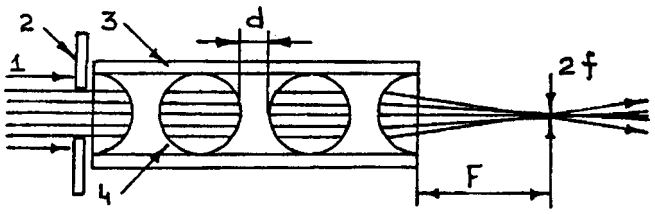

FIG. 1. Schematic of microcapillary x-ray lens: *1* — x-ray beam, *2* — diaphragm, *3* — glass microcapillary, *4* — adhesive, F — focal length of lens, and $2f$ — size of focal spot.

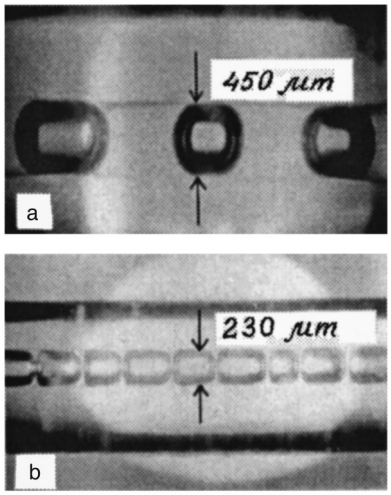

FIG. 2. Photographs of microcapillary x-ray lens made of: a — epoxy adhesive (epoxy resin and hardener); b — BF-6 adhesive (alcohol solution of polyvinylbutyral and resin).

a system containing microlenses fabricated of epoxy adhesive are fairly high, when BF-6 adhesive (Fig. 2b) or another adhesive consisting of an alcohol solution of resin and polymer is used, these gains can also be achieved for 3–5 keV photons. This is because the thickness of the microlens for this case becomes appreciably less than R, as can be seen from Fig. 2b, which increases the transmission T. However, calculations for this case present considerable difficulties because it is impossible to determine the shape of the microlens surface at this stage of the investigations. We plan to consider the results of experimental investigations for this case in a separate publication.

TABLE I.

R, μm	200	150	100	50
N	91	69	46	23
d, μm	540	390	240	90
T, %	1	9	38	83
$2f$, μm	12	9	6	3
G	5	38	150	331

This work was partially supported by the Belarus Fund for Fundamental Research (Grant No. F97-036).

[1] A. Snigirev, V. Kohn, I. Snigireva *et al.*, Nature (London) **384**, 49 (1996).
[2] A. Snigirev, V. Kohn, I. Snigireva *et al.*, Appl. Opt. **37**(4), 1 (1998).
[3] P. Elleaume, J. Synchrotron Radiat. No. **5**, 1 (1998).
[4] L. D. Landau and E. M. Lifshitz, *Fluid Mechanics*, 2nd ed. (Pergamon Press, Oxford, 1986) [Russ. original, 3rd ed., Nauka, Moscow, 1986, 736 pp.].
[5] *Handbook of Adhesives*, edited by G. V. Movsisyan [in Russian], Khimiya, Moscow (1980), 304 pp.

Translated by by R. M. Durham

Nonlinear characteristics of resonators and filters made from high-temperature superconducting films

I. B. Vendik, S. A. Gal'chenko, M. N. Gubina, V. V. Kondrat'ev, S. Leppyavuori, and E. Yakku

St. Petersburg State Electrotechnical University
(Submitted July 7, 1998)
Pis'ma Zh. Tekh. Fiz. **24**, 24–29 (December 26, 1998)

The behavior of planar superconducting resonators and filters under the action of an elevated-power microwave signal is described. A phenomenological model is proposed to provide an adequate description of the nonlinear properties of the surface resistance of a superconducting film. This model is used to derive an analytic expression to calculate the intrinsic Q factor of the resonator for various input power levels. The model uses a single phenomenological parameter whose value depends on the quality of the superconducting film and its capacity to sustain power. A temperature dependence is proposed for this parameter, which can reduce the results of measurements at different temperatures to a single value and allows the nonlinear properties of these film samples to be compared quantitatively. © *1998 American Institute of Physics.* [S1063-7850(98)02112-0]

High-temperature superconducting (HTSC) films on a dielectric substrate have been successfully used to fabricate planar band-pass microwave filters with the lowest losses in the pass band yet recorded. However, because of the nonlinearity of the surface resistance with respect to a microwave current, the characteristics of the filters are distorted when a microwave of fairly large amplitude propagates through the filter.

We investigated two filter configurations made from YBCO films on an $LaAlO_3$ substrate with a permittivity of 23.7 (PRIMA TEC films, $R_{sur}=0.6$ mΩ at temperature $T=77$ K and frequency $f=10$ GHz, film thickness 400–500 nm). The films were grown on substrates of different thickness, 0.45 and 1.0 mm. The filters were designed for the same frequency 1.75 GHz, the same 4% pass band, and the measurements were made at the same temperature $T=77$ K. The tenth-order filter consisted of an array of coupled half-wave microstripe resonators using exciting elements in the form of a T-shaped structure (Fig. 1a) on a 0.45 mm thick substrate (film No. 1). The filter characteristics at various input powers are shown in Fig. 1b. At an input power of 29 dBm (0.8 W) the characteristics become distorted as a result of the appearance of nonlinear effects.

A second ninth-order filter also consisted of an array of coupled half-wave resonators using coupled lines as exciting elements (Fig. 2a) on a 1 mm thick substrate (film No. 2). The relative position of the half-wave resonators was modified to improve the amplitude–frequency characteristic. The use of a thicker substrate presupposed a reduction of the rf current in the resonators and thus an increase in the nonlinearity threshold. The filter characteristics at different power levels are shown in Fig. 2b. The characteristics become distorted at an input power of 31 dBm (1.26 W), which barely exceeds the threshold power for the filter on a thinner substrate. The absence of any significant increase in the nonlinearity threshold for filter No. 2 is possibly due to the different quality of the films. Further investigations were carried out to obtain quantitative estimates of the nonlinear properties of the films.

Since these band-pass filters were based on coupled half-wave resonators, the nonlinear properties of the filters are determined by the nonlinear behavior of the resonators. Thus, an experimental investigation was made of half-wave resonators fabricated on the same substrates from the YBCO films used for the filters. The experimental results were assessed using the following model concepts.

The surface impedance of high-temperature superconductors as a function of frequency and temperature is reliably described by the linear approximation of the phenomenological model.[1] At high microwave powers a nonlinear increase in the surface resistance is observed, which may be expressed as a function of the magnetic field strength in a section of the line:[2]

$$R_{sur}(x,t)=R_{sur,0}\left(1+\frac{H_m^2}{H_0^2}f^2(t,x)\right), \tag{1}$$

where $R_{sur,0}$ is the surface resistance of the superconductor in the linear approximation, H_m is the amplitude of the magnetic field strength in a section of the HTSC transmission line, $f(t,x)$ is a function which allows for the dependence of the magnetic field on the time and position, and H_0 is the phenomenological parameter of the model.

The parameter H_0 can be estimated as

$$H_0 \approx j_c \lambda_L, \tag{2}$$

where j_c is the critical current density and λ_L is the London depth of penetration of the field in the superconductor.

The nonlinear properties of HTSC resonators are estimated from the change in the Q factor as the microwave input power is increased:[2]

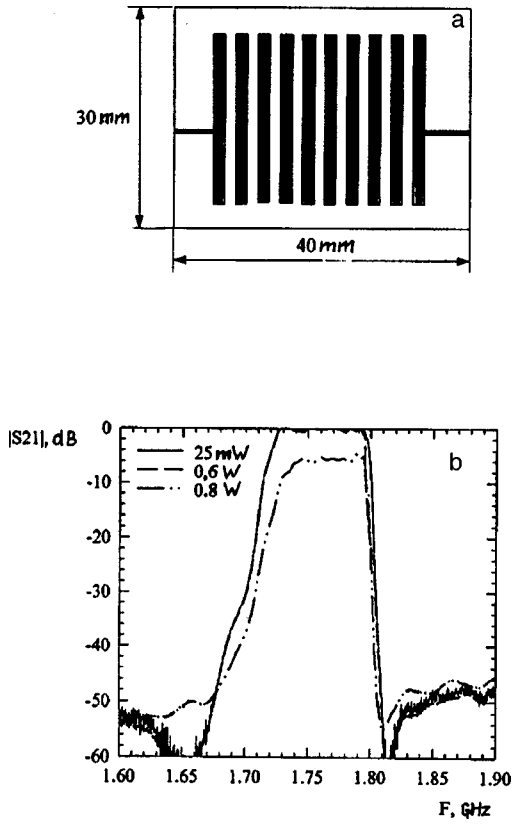

FIG. 1. Topology of a tenth-order filter (a) and its amplitude–frequency characteristic at various powers (b).

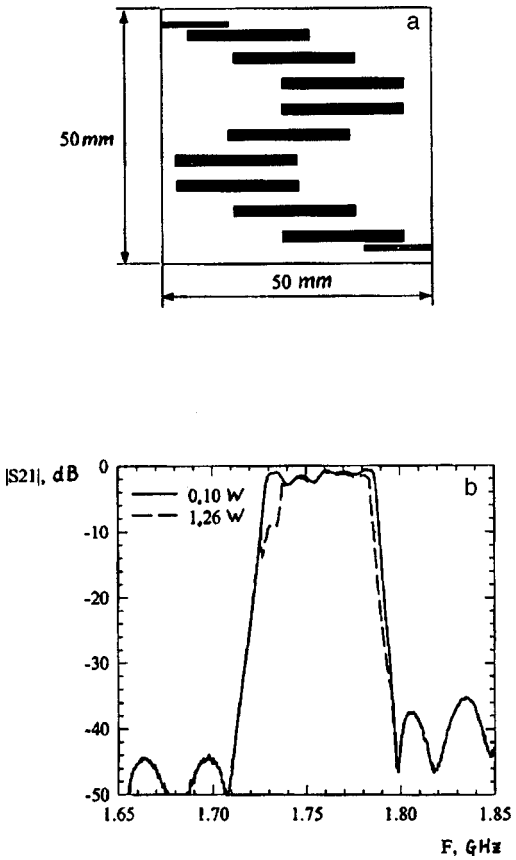

FIG. 2. Topology of a ninth-order filter (a) and its amplitude–frequency characteristic at various powers (b).

$$\frac{Q_0}{Q_{0,\mathrm{eff}}} = 1 + \frac{9}{4\pi}\frac{P_{in}}{P_0}\frac{Q_E}{\left(1+\dfrac{Q_E}{Q_{0,\mathrm{eff}}}\right)^2}. \tag{3}$$

Here Q_0 is the intrinsic Q factor of the resonator in the linear approximation, $Q_{0,\mathrm{eff}}$ is the effective Q factor of the resonator as a function of the input power P_{in}, Q_E is the external Q factor of the resonator, which is determined by the coupling between the resonator and the external circuits, and P_0 is the characteristic power defined as the microwave power in the resonator assuming that the magnetic field strength in it is H_0. The parameter P_0 is a quantitative measure of the capacity of the HTSC film forming part of a resonator to withstand a high microwave power level without nonlinear distortions. As P_0 increases, the nonlinearity threshold of the film increases.

In the nonlinear regime we investigated two half-wave microstripe resonators on two different substrates. Figure 3 gives the results of measurements of the normalized intrinsic Q factor of a resonator formed by YBCO film No. 1 on a thin substrate plotted as a function of the input microwave power at $T=60$ K. The Q factor was normalized to that measured in the linear regime at low input microwave power. Also plotted is the calculated characteristic (3) obtained for $P_0=23$ W. The nonlinear characteristics were measured at different temperatures. In accordance with expression (2), P_0 depends on temperature, since the critical current and the London penetration depth depend on temperature. Using the typical temperature dependence of the critical current and the temperature dependence of the London depth given by the model,[1] we proposed the following temperature dependence for the parameter P_0:

$$P_0(T) = P_0(0)\left(1-\left(\frac{T}{T_c}\right)^2\right), \tag{4}$$

where $P_0(0)$ is determined at $T=0$ by extrapolating the experimental results.

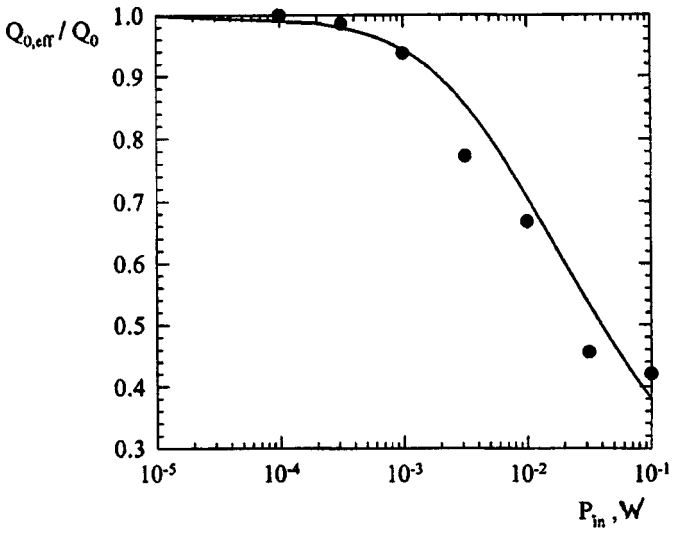

FIG. 3. Normalized intrinsic resonator Q factor versus input power.

For the second resonator, formed by film No. 2 on a thick substrate, the measurements were made at the same temperature $T=77$ K. Reducing the results of the measurements of the nonlinear resonator characteristics to the same temperature (77 K) using expression (4), we find $P_0=12$ W for film No. 1 and $P_0=2$ W for film No. 2, which suggests that the films are of different quality in terms of their nonlinear characteristics: film No. 2 on the thick substrate has a lower nonlinearity threshold in a microwave field than film No. 1.

Investigations of the nonlinear characteristics of the films show complete agreement with the measurements of the nonlinearity parameter for the half-wave resonators, which confirms that the parameter P_0 is suitable for estimating the nonlinear properties of planar HTSC filters.

This work was carried out under Project No. 98063 of the State Scientific and Technical Program in the ''Superconductivity'' category of ''Topical Problems in the Physics of Condensed Media'' and received financial support from the Nokia Foundation.

[1] O. G. Vendik, I. B. Vendik, and D. I. Kaparkov, IEEE Trans. Microwave Theory Tech. **46**, 469 (1998).
[2] O. G. Vendik, I. B. Vendik, and T. B. Samoilova, IEEE Trans. Microwave Theory Tech. **45**, 173 (1997).

Translated by R. M. Durham

Dispersion of a charged bubble in a liquid dielectric in a electrostatic field

S. O. Shiryaeva and A. N. Zharov

P. G. Demidov State University, Yaroslavl
(Submitted June 29, 1998)
Pis'ma Zh. Tekh. Fiz. **24**, 30–35 (December 26, 1998)

It is predicted that the size and charge of daughter bubbles emitted in an electrostatic field from different tips of a charged parent bubble will differ.
[S1063-7850(98)02212-5]

It has been shown that when a charged gas bubble in a liquid dielectric disperses in an electrostatic field, the number, size, and charge of daughter bubbles formed at the opposite tips of the parent bubble differ substantially.

The breakup of bubbles in a dielectric liquid in an external electrostatic field is an interesting phenomenon for various branches of technical physics, geophysics, and chemical technology.[1,2] It is therefore interesting to identify the basic laws governing the breakup of a charged bubble in an electrostatic field; this may be performed by analogy with the analyses made for a droplet.[3,4]

Let us assume that a uniform electrostatic field of strength **E** is created in a liquid dielectric containing a spherical gas bubble of radius R with surface charge Q and surface tension σ at the interface. Under the action of the field **E**, the bubble is pulled along **E** into a spheroid of revolution having eccentricity e, and the gas pressure therein becomes equal to P. If the charges at the surface of the bubble possess fairly high mobility, for large **E** the bubble becomes unstable and small charged daughter bubbles begin to break away from the opposite tips of the bubble.

As daughter bubbles break away from the parent, they change their volume from V_{ij}^0 to V_{ij} as the pressures equalize, and the gas pressure in these bubbles becomes P_{ij} (here the first subscript indicates the tip of the parent bubble: $i=1$ for a bubble emitted from a tip whose polarization charge has the same sign as the bubble's own charge Q; $i=2$ for the second tip, and the second subscript j indicates the number of the bubble in the emission process). The daughter bubbles, becoming separated from the parent bubble under the action of electric repulsion forces, form two groups at a distance $L=ma$ from the two tips of the parent bubble (a is the major semiaxis and m is a numerical parameter).[1] In our model calculations, the electric field of the group of daughter bubbles, which opposes the separation of the next bubble, is replaced by the field of a point charge positioned on the axis of symmetry of the system at the distance L from the tip of the mother bubble.

We shall assume that at a certain time $n-1$ daughter bubbles are emitted from the first tip of the parent bubble and $l-1$ emissions have taken place from the second tip. As a result of the emission, daughter bubbles with charges $q_{ij} \ll (Q+ER^2)$ and radii $r_{ij} \ll R$ are formed. The time required to separate a daughter bubble is assumed to be of the order of the period of the capillary oscillations of its dominant mode $\sim (r_{ij})^{3/2}$. Thus, over the time taken for one large daughter bubble to break away from the second tip, k small bubbles become detached from the first tip, where k will subsequently be defined as $k=(r_{2l}/r_{in})^{3/2}$. The daughter bubbles in the total electric field will have the form of ellipsoids of revolution with the eccentricities[5] e_{ij} which will be determined by iteration.

Assuming that the liquid and gas temperatures are constant, we can easily find the change in the potential energy of the system as a result of the next emission of two daughter bubbles from opposite tips of the parent bubble

$$\begin{aligned}\Delta U_{ij} &= 4\pi\sigma r_{ij}^2 A(e_{ij}) + q_{ij}^2 \frac{B(e_{ij})}{2r_{ij}} \\ &\quad - 2q_{ij}\frac{B(e)}{R}\left[Q - \sum_{j=1}^{n-1} q_{1j} - \sum_{j=1}^{l-1} q_{2j}\right] \\ &\quad + q_{ij}\frac{K(\nu_{ij})}{R}\left[Q - \sum_{j=1}^{n-1} q_{1j} - \sum_{j=1}^{l-1} q_{2j}\right] \\ &\quad + (-1)^{i+1} ERq_{ij}\Omega(\nu_{ij}) + \frac{q_{ij}}{L}\sum_{j=1}^{n(i)-1} q_{ij} \\ &\quad - \frac{4\pi}{3}V_{ij}P_{ij}\ln\left[\frac{V_{ij}}{V_{ij}^0}\right] - \frac{4\pi}{3}P_{at}[V_{ij}^0 - V_{ij}], \qquad (1)\end{aligned}$$

$$A(e_{ij}) = \frac{1}{2}\left((1-e_{ij}^2)^{1/2} + \frac{\arcsin e_{ij}}{e_{ij}}\right)(1-e_{ij}^2)^{-1/6},$$

$$B(e_{ij}) = \frac{(1-e_{ij}^2)^{1/3}}{e_{ij}}\operatorname{arctanh}(e_{ij}),$$

$$K(\nu_{ij}) = \frac{(1-e^2)^{1/3}}{e}\operatorname{arctanh}\left(\frac{e}{\nu_{ij}}\right), \quad \nu_{ij} = \left(1+\frac{\xi_{ij}}{a^2}\right)^{1/2},$$

$$\Omega(\nu_{ij}) = \frac{e(\nu_{ij}-1) - \nu_{ij}\operatorname{arctanh}[e(\nu_{ij}-1)(\nu_{ij}-e^2)^{-1}]}{(1-e^2)^{1/3}(\operatorname{arctanh} e - e)},$$

$$n(i) = \begin{cases} n, & \text{if } i=1, \\ l, & \text{if } i=2, \end{cases}$$

ξ_{ij} are the spheroidal coordinates of the daughter bubbles at the instant of detachment from the parent bubble and P_{at} is atmospheric pressure. In Eq. (1) the first term describes the

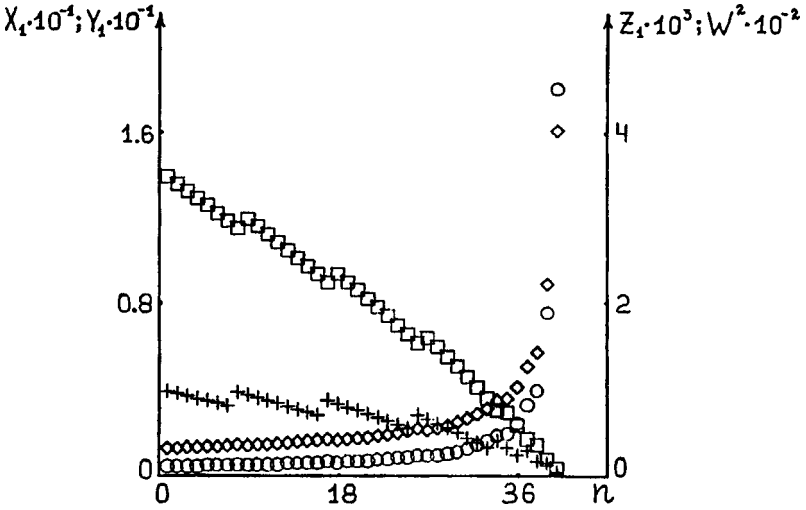

FIG. 1. Dependences of the following dimensionless parameters on the bubble number n: the radii X_1 (calculated points denoted by ◇), charges Y_1 (calculated points denoted by 0), and specific charges Z_1 (calculated points denoted by □) for daughter bubbles carrying charge of the same sign as the intrinsic charge of the parent bubble, and also the Rayleigh parameter W^2 for the parent bubble (calculated points denoted by +) for $w^2=0.06$, $W^2=0.01$, $e^2=0.7$, $\alpha_1=0.9$, $m=1$, $\beta=0.75$, and $\eta_1=0.6$ (the parameters $\alpha_{1j}=\alpha_1$, $\eta_{1j}=\eta_1$ were taken to be independent of the bubble number n).

surface energy of the daughter bubbles, the second and third describe the change in the intrinsic electrostatic energy of the bubbles, the fourth describes the change in the energy of electric interaction between the charges of the daughter bubbles and the charge of the parent bubble, the fifth term describes the change in the energy of interaction between the daughter bubbles and the polarization charge of the parent bubble, the sixth term describes the energy of interaction between the daughter bubble and the group of previously emitted bubbles, and the seventh and eighth terms describe the work performed by the gas in isothermally changing the volume of the daughter bubble.

The emission of daughter bubbles will continue as long as the Coulomb force responsible for detaching a daughter bubble exceeds the Laplacian force $2\pi\sigma r_{ij}^*$ responsible for confining the bubble, where r_{ij}^* is the radius of the neck. Assuming that the field strength at the point of detachment is determined by the field of the parent bubble, and also by the field of previously detached daughter bubbles, we obtain the conditions for detachment of daughter bubbles from different tips of the parent bubble:

$$\frac{\alpha_{ij}X_{ij}(1-e_{ij}^2)^{1/6}}{8} \leqslant Y_{ij}(w+W)^2\left\{\left[\frac{W}{w+W}-\sum_{j=1}^{n-1}Y_{1j}-\sum_{j=1}^{l-1}Y_{2j}\right]C(\nu_{ij}) + (-1)^{i+1}\frac{w}{w+W}T(\nu_{ij})-\frac{(1-e^2)^{2/3}}{m^2}\sum_{j=1}^{n\langle i\rangle-1}Y_{ij}\right\}, \quad (2)$$

$$T(\nu_{ij})=1-\frac{\operatorname{arctanh}(e\,\nu_{ij}^{-1})-e\,\nu_{ij}(\nu_{ij}^2-e^2)^{-1}}{\operatorname{arctanh}(e)-e},$$

$$C(\nu_{ij})=\frac{(1-e^2)^{2/3}}{(\nu_{ij}^2-e^2)},$$

$$\alpha_{ij}=\frac{r_{ij}^*}{b_{ij}}, \quad Y_{ij}=\frac{q_{ij}}{(Q+ER^2)}, \quad X_{ij}=\frac{r_{ij}}{R},$$

$$W^2=\frac{Q^2}{16\pi\sigma R^3}, \quad w^2=\frac{E^2R}{16\pi\sigma},$$

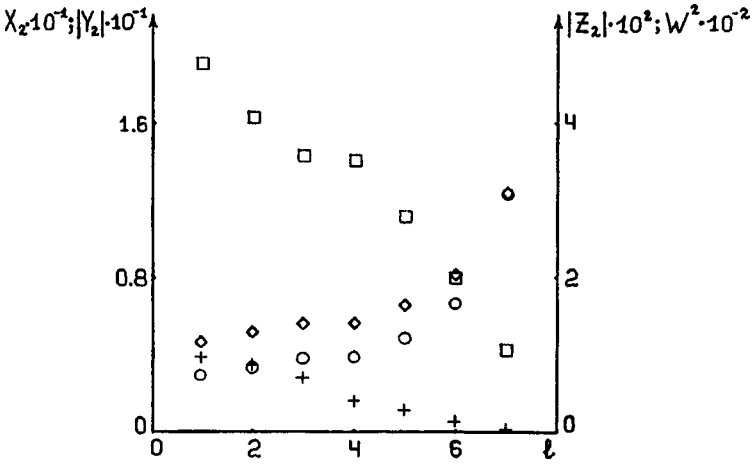

FIG. 2. Dependences of the following dimensionless parameters on the bubble number l: the radii X_2 (calculated points denoted by ◇), the absolute values of the charges $|Y_2|$ (calculated points denoted by 0), and the absolute values of the specific charges $|Z_2|$ (calculated points denoted by □) for daughter bubbles carrying charge of sign opposite that of the intrinsic charge of the parent bubble, and also the Rayleigh parameter W^2 for the parent bubble (calculated points denoted by +) for $w^2=0.06$, $W^2=0.01$, $e^2=0.7$, $\alpha_2=0.9$, $m=1$, $\beta=0.75$, and $\eta_2=0.6$ (the parameters $\alpha_{2j}=\alpha_2$, $\eta_{2j}=\eta_2$ were taken to be independent of the bubble number l).

where X_{ij} and Y_{ij} are the dimensionless radii and charges of the daughter bubbles, and b_{ij} are the minor semiaxes of the daughter bubbles. In Eq. (2) the first and second terms in braces describe the electric field strength created by the intrinsic and polarization charges of the parent bubble at the point of detachment of the daughter bubble, and the third term gives the electric field strength at the same point produced by the total charge of the groups of previously emitted bubbles.

We impose the constraint that because of the Onsager principle of least energy scattering, the change in the potential energy is extremal, i.e., the conditions $\partial(\Delta U_{ij})/\partial q_{ij}=0$, $\partial(\Delta U_{ij})/\partial r_{ij}=0$ are satisfied.[6] This gives, in addition to Eq. (2), another four equations to find the unknowns X_{ij}, Y_{ij}, and ν_{ij}.

$$Y_{ij}\frac{B(e_{ij})}{X_{ij}}+\left[\frac{W}{w+W}-\sum_{j=1}^{n-1}Y_{1j}-\sum_{j=1}^{l-1}Y_{2j}\right][K(\nu_{ij})-B(e)]$$
$$-(-1)^{i+1}\frac{w}{w+W}\Omega(\nu_{ij})+\frac{(1-e^2)^{1/3}}{m}\sum_{j=1}^{n(i\rangle-1}Y_{ij}=0, \tag{3}$$

$$X_{ij}=A(e_{ij})-(W+w)^2Y_{ij}^2\frac{B(e_{ij})}{X_{ij}^2}-\eta_{ij}\beta X_{ij}^2=0, \tag{4}$$

$$\eta_{ij}=\frac{P_{ij}-P_{at}}{P-P_{at}}, \quad \beta=\frac{(P-P_{at})R}{2\sigma}.$$

A numerical analysis of the system (2)–(4) shows that the radii and charges of daughter bubbles emitted from the second tip, the sign of whose polarization charge differs from that of the intrinsic charge of the parent bubble, will be greater than the dimensions and charges of the bubbles emitted from the first tip, whose polarization charge has the same sign as that of the parent bubble, as can be seen from Figs. 1 and 2. These figures also show that the number of daughter bubbles emitted from the first tip is much greater that the number emitted from the second tip.

[1] C. G. Garton and Z. Krasucki, Trans. Faraday Soc. **60**, 211 (1964).
[2] A. I. Grigor'ev, V. A. Koromyslov, and A. N. Zharov, Pis'ma Zh. Tekh. Fiz. **23**(19), 60 (1997) [Tech. Phys. Lett. **23**, 760 (1997)].
[3] A. I. Grigor'ev and S. O. Shiryaeva, J. Phys. D **23**, 1361 (1990).
[4] A. I. Grigor'ev and S. O. Shiryaeva, Zh. Tekh. Fiz. **61**(3), 19 (1991) [Sov. Phys. Tech. Phys. **36**, 258 (1991)].
[5] A. I. Grigor'ev, S. O. Shiryaeva, and E. I. Belavina, Zh. Tekh. Fiz. **59**(6), 27 (1989) [Sov. Phys. Tech. Phys. **34**, 602 (1989)].
[6] S. O. Shiryaeva and A. I. Grigor'ev, Zh. Tekh. Fiz. **65** (1) 25; (2), 11 (1995) [Tech. Phys. **40**, 12, 122 (1995)].

Translated by R. M. Durham

Instability growth rate of an uncharged droplet in a uniform electrostatic field

A. I. Grigor'ev

P. G. Demidov State University, Yaroslavl
(Submitted June 29, 1998)
Pis'ma Zh. Tekh. Fiz. **24**, 36–40 (December 26, 1998)

An interpretation is proposed for an effect in which the spheroidal deformation of a droplet which is unstable against induced charge increases more rapidly than exponential with time.
 [S1063-7850(98)02312-X]

Since the amplitude of the perturbation of a droplet shape which is unstable with in relation to a critical uniform electrostatic field increases nonlinearly, the time evolution of the amplitude of a spheroidal axisymmetric perturbation of its shape is substantially faster than exponential.

The phenomenon of instability of an uncharged droplet of electrically conducting liquid in a uniform electrostatic field **E** is encountered in a wide range of different applications in physics, geophysics, scientific instrument manufacture, engineering, and chemical technology (see Refs. 1–3 and the cited literature). This effect is observed as a rapid increase in the amplitude of the spheroidal deformation of the droplet with time, followed by the ejection of excess polarization charge from the tips in the form of a series of highly dispersed, strongly charged droplets. Nevertheless, some aspects of this instability have been little studied, particularly the growth rate of the spheroidal deformation of an unstable droplet with time. A theoretical analysis of this aspect is also of interest because Inoulett *et al.*[4,5] established experimentally that the growth rate of the spheroidal deformation of an unstable droplet is faster than exponential.

1. From Refs. 6 and 7, the spectrum of capillary oscillations of an isolated droplet of radius R, consisting of an ideal conducting liquid, in a uniform electrostatic field **E** with the surface tension σ is given by

$$\omega_n^2 = -\frac{\sigma}{\rho R^3} n(n-1)(n+2)[1-WA(n)], \quad W = E^2 R \sigma^{-1}, \tag{1}$$

where n is the number of the capillary oscillation mode, ρ is the density of the liquid, and the coefficient $A(n)$ is determined by the mode number n and by the system of physical units used. For the dominant mode $(n=2)$ responsible for the spheroidal deformation we have $A_2^{-1}=2.59$ in Gaussian units. It can be seen from formula (1) that for $W>A_2^{-1}$ the droplet begins to become unstable, and within the limits of validity of linear analysis, the amplitude ζ of the dominant mode of its capillary oscillations begins to increase with time as $\zeta \sim \exp(\chi t)$, where

$$\chi = \sqrt{\frac{8\sigma}{\rho R^3}[1-W(e^2)A_2]} \tag{2}$$

is the instability growth rate.

However, when $W=A_2^{-1}$ holds, the droplet is already unstable against infinitesimal virtual deformations of its surface of the form $\zeta=\zeta_0 P_2(\cos\theta)$. The excitation of this type of deformation could at least be responsible for the thermal motion of the liquid molecules.

2. Let us assume that the field E corresponds to the critical value of the parameter W. The initial equilibrium droplet shape in E is spheroidal with eccentricity e_0. When instability occurs, the droplet departs from equilibrium and its eccentricity begins to increase with time. All this stems from an infinitesimal thermal perturbation of the dominant mode of the type $\zeta=\zeta_0 P_2(\cos\theta)$. The amplitude ζ_0 of the thermal perturbation of the droplet shape is given by $\zeta_0=(\sigma/kT)^{-1/2}$, where k is the Boltzmann constant and T is the absolute temperature of the liquid. For this type of perturbation the major and minor semiaxes of the spheroid are given by $a=R+\zeta_0$ and $b=R-\frac{1}{2}\zeta_0$, since $P_2(0)=1$, and $P_2(\pi/2)=-1/2$.

The square of the eccentricity e^2 of the resulting spheroid is related to the amplitude ζ_0 of the small perturbation to within the first order of smallness with respect to ζ_0/R by

$$e^2 = 1-\frac{(b_0-0.5\zeta_0)^2}{(a_0+\zeta_0)^2} \approx e_0^2 + \frac{3\zeta_0}{R}\left(1-\frac{7}{6}e_0^2\right). \tag{3}$$

3. Thus, thermal excitation of the dominant mode in a spheroidal droplet corresponds to a virtual increase in its eccentricity from e_0 to e, defined by Eq. (3). However, for a spheroid the critical value of the parameter W for instability of the droplet with respect to the polarization charge is a decreasing function of the square of the eccentricity.[6,7] To first order in the square of the eccentricity e^2 this function may be expressed in the form[6,7]

$$WA_2 = [1-\alpha e^2]. \tag{4}$$

The value $WA_2=1$ for $e^2>e_0^2$ will be supercritical for the spheroid, and when $\zeta_0/R \ll 1$ holds classical concepts indicate that the amplitude of the perturbation will begin to increase exponentially with time with the growth rate χ given by Eq. (2). In expression (2) for χ we substitute Eq. (4), which gives

$$\chi = \sqrt{\frac{8\sigma}{\rho R^3}\alpha e^2}. \tag{5}$$

This implies that the amplitude ζ of the perturbation of the spheroidal droplet shape will increase with time as

$$\zeta=\zeta_0 e^{\chi t}=\zeta_0\exp\left(\sqrt{\frac{8\sigma}{\rho R^3}\alpha e^2}\,t\right). \tag{6}$$

However, an increase in the amplitude of the perturbation corresponds to further elongation of the droplet, an increase in its eccentricity, and a reduction in the critical value of the parameter W required for instability, as given by formula (4), and therefore increases the instability growth rate.

4. Writing a series of increasing perturbations at similar times and using Eqs. (2)–(6), we can obtain a nonlinear integral equation to describe the growth of the amplitude ζ with time, as was done[8] for a droplet which was unstable with respect to its own charge:

$$\zeta(\tau)=\zeta_0\exp\left\{\int_0^\tau\left(\alpha_*\frac{\zeta(\tau)}{\zeta_0}\right)^{1/2}d\tau\right\}, \tag{7}$$

$$\tau=\left(\frac{8\sigma}{\rho R^3}\right)^{1/2}t,\quad \alpha_*=3\alpha\frac{\zeta_0}{R}\left(1-\frac{7}{6}e_0^2\right).$$

The solution of Eq. (7) has the form

$$\zeta(\tau)=\zeta_0(1-0.5\alpha_*\tau)^{-2}.$$

To within the dimensionless notation Eqs. (7) and (8) agree with the similar relations describing the temporal increase in the amplitude of the spheroidal perturbation of an initially spherical droplet which is unstable with respect to its own charge.[9] It is easy to see that the time dependence of the amplitude of the spheroidal perturbation (8) is stronger than exponential with the growth rate α_* (Ref. 9), and agrees qualitatively with that determined experimentally.[5]

Assuming that the value of the Taylor parameter W substantially exceeds the critical value for the onset of instability, i.e., $WA_2=1+\eta$, where $\eta\geqslant 0$, the expression for the instability growth rate of the dominant mode will have the form

$$\chi=\sqrt{\frac{8\sigma}{\rho R^3}(\eta+\alpha e^2)},$$

and the integral equation describing the time dependence of the amplitude of the dominant-mode instability will be

$$\zeta(\tau)=\zeta_0\exp\left\{\int_0^\tau\left(\eta_*+\alpha_*\frac{\zeta(\tau)}{\zeta_0}\right)^{1/2}d\tau\right\},\quad \eta_*=\eta+\alpha e_0^2. \tag{8}$$

The solution of Eq. (9) may be written as

$$\tau\eta_*^{1/2}=\ln\left\{\frac{[(\eta_*+\alpha_* X)^{1/2}-\eta_*^{1/2}][(\eta_*+\alpha_*)^{1/2}+\eta_*^{1/2}]}{[(\eta_*+\alpha_* X)^{1/2}+\eta_*^{1/2}][(\eta_*+\alpha_*)^{1/2}-\eta_*^{1/2}]}\right\},$$

$X=\zeta(\tau)/\zeta_0$.

When $\eta_*\gg\alpha_* X$ this relation is reduced to the exponential form to first order in $\alpha_* X$,

$$\zeta(\tau)=\zeta_0\exp(\eta_*^{1/2}\tau).$$

That is to say, in this situation the time evolution of the amplitude of the spheroidal perturbation is characterized by the growth rate $\eta_*^{1/2}$, which describes the degree of supercriticality of the Taylor parameter W.

5. To conclude, when an uncharged droplet of electrically conducting liquid becomes unstable with respect to an external uniform electrostatic field, the elogation of the droplet into a spheroid exhibits different time behavior depending on the conditions for departure from equilibrium.

[1] G. I. Taylor, Proc. R. Soc. London, Ser. A **280**, 383 (1964).
[2] A. I. Grigor'ev and S. O. Shiryaeva, J. Phys. D **23**, 1361 (1990).
[3] A. I. Grigor'ev and S. O. Shiryaeva, Izv. Ross. Akad. Nauk Ser. Mekh. Zhidk. Gaza No. 4, 3 (1994).
[4] I. I. Inoulett and R. Kromann, IEEE Trans. Ind. Appl. **25**, 945 (1989).
[5] I. I. Inoulett, J. M. Floryan, and R. J. Haywood, IEEE Trans. Ind. Appl. **28**, 1203 (1992).
[6] A. I. Grigor'ev and O. A. Sinkevich, Izv. Akad. Nauk SSSR. Ser. Mekh. Zhidk. Gaza No. 6, 10 (1985).
[7] K. J. Cheng, Phys. Lett. A **112**, 392 (1985).
[8] S. O. Shiryaeva, A. I. Grigor'ev, and I. D. Grigor'eva, Zh. Tekh. Fiz. **65**(9), 39 (1995) [Tech. Phys. **40**, 885 (1995)].
[9] S. O. Shiryaeva and I. D. Grigor'eva, Pis'ma Zh. Tekh. Fiz. **20**(6), 1 (1994) [Tech. Phys. Lett. **20**, 214 (1994)].

Translated by R. M. Durham

Interaction of hydroxyapatite with titanium nickelide and titanium

N. A. Shevchenko, V. I. Itin, A. A. Tukhfatullin, M. L. Melikyan, and M. Z. Mirgazizov

Research Institute of Medical Materials and Implants with Shape Memory, Tomsk
(Submitted July 14, 1998)
Pis'ma Zh. Tekh. Fiz. **24**, 41–44 (December 26, 1998)

It has been established that the interaction of hydroxyapatite with titanium nickelide and titanium results in the formation of new phases whose physicomechanical properties and biocompatibility are unknown. After hydroxyapatite has been resorbed, these phases come in contact with tissue and near-tissue fluids and influence the result of the implant.
 [S1063-7850(98)02425-2]

Hydroxyapatite is one of the best materials for osteoreplacement, since when inserted in the body it is resorbed and normalizes osteogenesis.[1] Thus, it is widely used for coating metallic medical implants. The main methods of depositing hydroxyapatite on a metal base are plasma deposition[2,3] and baking.[4] However, interaction of the components at the metal(alloy)–hydroxyapatite interface has been very little studied,[2,3] although this subsequently determines the physicomechanical properties and biocompatibility of the implant with the body tissue.

Here we use thermography, derivative differential thermal analysis (DDTA), and x-ray phase analysis to investigate the interaction of hydroxyapatite with titanium nickelide and titanium, which are widely used as materials for implants in medicine.[5]

The thermal effects were studied using a Q-1500 derivatograph in an argon atmosphere. The x-ray phase analysis was carried out using a DRON-3 device using with radiation and a filter.

Powder of PN55T45 grade titanium nickelide and PTOM grade titanium was thoroughly dried and then mixed in the ratio 1:1 by weight with ''Hydroxyapol'' hydroxyapatite powder manufactured by ''Polikom,'' which complies with the international standard ASTM-F 1185-88 and is licensed for medical use.[6]

Cylindrical samples 10 mm in diameter and 5 mm high were pressed from the mixture and baked in an SNVÉ 1.3.1/16 ICh electrical furnace in a vacuum of 133×10^{-4} Pa using different temperature–time regimes.

The thermogram of pure hydroxyapatite does not exhibit any thermal effects up to 1400 °C, which agrees with Ref. 7. For mixtures of this substance with titanium the curves are almost smooth and there are no thermal effects to indicate any interaction of the components. The thermograms of mixtures of hydroxyapatite and titanium nickelide revealed an endothermic effect at 1145 °C. Heating of weighed batches of titanium or titanium nickelide powder mixed with hydroxyapatite in the temperature range 100–900 °C is accompanied by a negligible reduction in mass (2–3%), which is evidently caused by loss of water or an OH group.

An x-ray phase analysis reveals that the interplanar spacings and the unit cell parameters of the hydroxyapatite powder show good agreement with the ASTM data. After baking at 1150 °C the phase composition is indistinguishable from the initial composition, and only a change in the line intensities can be identified. Heating in the derivatograph to

TABLE I. Phase composition of baked mixtures of hydroxyapatite with titanium nickelide and titanium.

	Phase composition	
Baking regime	Hydroxyapatite–TiNi	Hydroxyapatite–Ti
Initial mixture	$Ca_{10}(PO_4)_6(OH)_2$, TiNi	$Ca_{10}(PO_4)_6(OH)_2$, Ti
$T=800$°C, 2 h	$Ca_{10}(PO_4)_6(OH)_2$, TiNi, Ni_3Ti	$Ca_{10}(PO_4)_6(OH)_2$, Ti
$T=950$°C, 10 min	$Ca_{10}(PO_4)_6OH_2$, TiNi, Ni_3Ti, CaO, $Ca_4P_2O_9$	$Ca_{10}(PO_4)_6(OH)_2$, Ti, CaO, $Ca_4P_2O_9$
$T=950$°C, 2 h	$Ca_{10}(PO_4)_6(OH)_2$, TiNi, Ni_3Ti, $NiTi_2$, CaO, $Ca_4P_2O_9$	Ti, CaO, $Ca_4P_2O_9$
$T=1050$°C, 2 h	Ni_3Ti, $NiTi_2$, $Ca_4P_2O_9$, $Ca_3(PO_4)_2$, $CaTiO_3$, Ti_3P	Ti, $Ca_4P_2O_9$, $Ca_3(PO_4)_2$, $CaTiO_3$, Ti_3P
$T=1150$°C, 2 h	Ni_3Ti, $NiTi_2$, $Ca_4P_2O_9$, $Ca_3(PO_4)_2$, $CaTiO_3$, Ti_3P	$CaTiO_3$, Ti_3P
Heating to 1400°C in derivatograph	$CaTiO_3$, Ti_3P	$CaTiO_3$, Ti_3P

1300 °C results in the appearance of CaO calcium oxide lines. Thus, hydroxyapatite undergoes partial thermal decomposition at lower temperatures than those indicated in the literature.[7]

The phase composition of baked mixtures of hydroxyapatite and titanium nickelide powders is given in Table I. On the x-ray diffraction patterns of the initial mixture of hydroxyapatite and titanium nickelide powders, the position of the x-ray lines and their intensity correspond to those of the components. Baking at 800 °C for 2 h gives rise to Ni_3Ti lines. After baking at 950 °C for 10 min the intensities of the lines assigned to $Ca_{10}(PO_4)_6(OH)_2$ and titanium nickelide are reduced appreciably, and lines of tetracalcium phosphate $Ca_4P_2O_9$ and possibly CaO are also observed. An increase in the baking time to 2 h results in the appearance of $NiTi_2$ lines and a further reduction in the line intensities of the main components, while the lines of the $Ca_4P_2O_9$ and CaO phases remain almost unchanged.

When the temperature is increased further to 1050 °C, the lines ascribed to hydroxyapatite and titanium nickelide disappear and the phases $CaTiO_3$, tricalcium phosphate $Ca_3(PO_4)_2$, and apparently Ti_3P appear. The $Ca_4P_2O_9$, $Ca_3(PO_4)_2$, and CaO phases observed after baking correspond to the decomposition products of hydroxyapatite under heating. The calcium phosphates $Ca_4P_2O_9$ and $Ca_3(PO_4)_2$ in turn decompose to form phosphoric and calcium oxides, P_2O_5 and CaO. The phosphoric oxide is reduced by the titanium to form titanium oxide TiO_2 and titanium phosphide Ti_3P. Subsequent interaction between the calcium oxide and the titanium oxide results in the formation of the $CaTiO_3$ phase. After baking at 1150 °C the phase composition remains almost unchanged and only the line intensities are redistributed. X-ray diffraction patterns of the initial mixture after heating in the derivatograph to 1400 °C only reveal lines of $CaTiO_3$ and titanium phosphide Ti_3P.

A study of the interaction of the components when titanium and hydroxyapatite are baked under the same conditions yields similar results. In the temperature range 950–1150 °C titanium reacts with the hydroxyapatite to form the phases described above (see Table I). These results agree with those reported earlier,[8] where the phases Ti_3P and $CaTi_2O_5$ were observed when hydroxyapatite was deposited on a titanium plate by plasma deposition.

Thus, we have established that interaction of hydroxyapatite with titanium nickelide and titanium at the interface results in the formation of new phases whose physicomechanical properties and biocompatibility are unknown. Since hydroxyapatite is a bioactive ceramic which is gradually resorbed in the body, these phases can substantially influence the result of an implant.

[1] L. N. Lysenok, Nov. Stomat. Spets. Vypusk. No. 6, 61 (1997).
[2] V. N. Lyasnikov and L. A. Vereshchagina, Perspekt. Mater. No. 6, 50 (1996).
[3] V. A. Klimenkov, Yu. F. Ivanov, A. V. Karlov *et al.*, Perspekt. Mater. No. 5, 44 (1997).
[4] F. Watari, A. Yokoyama, F. Saso *et al.*, in *Proceedings of the Third International Symposium on Structural and Functional Gradient Materials*, Switzerland, 1994, pp. 703–708.
[5] V. E. Gyunter, V. I. Itin, L. A. Monasevich *et al.*, *Shape Memory Effects and Their Application in Medicine* [in Russian], Nauka, Novosibirsk (1992), 742 pp.
[6] A. S. Berlyand, A. I. Volozhin, A. Z. Knizhnik *et al.*, Nov. Stomat. No. 3, 9 (1992).
[7] V. P. Orlovskiĭ, Zh. A. Ezhova, G. V. Rodicheva *et al.*, Zh. Neorg. Khim. **35**, 1337 (1990).
[8] I. A. Shchepetkin, Usp. Sovrem. Biol. **115**(1), 58 (1995).

Translated by R. M. Durham

Protection of $YBa_2Cu_3O_{7-\delta}$ films from atmospheric degradation

K. Yu. Kravchenko and V. A. Marchenko

Institute for Problems in Microelectronics Technology and Ultrapure Materials, Russian Academy of Sciences, Chernogolovka

(Submitted July 14, 1998)
Pis'ma Zh. Tekh. Fiz. **24**, 45–49 (December 26, 1998)

Thin (40–80 nm) layers of YSZ deposited on the surface of $YBa_2Cu_3O_{7-\delta}$ films reliably protect the superconductor from atmospheric degradation. The high rate of oxygen diffusion in the protective layer allows further oxidation of the $YBa_2Cu_3O_{7-\delta}$. Processes accompanied by release of oxygen from the $YBa_2Cu_3O_{7-\delta}$ cause the protective properties of the coating to be lost.
 [S1063-7850(98)02512-9]

It is well known that when $YBa_2Cu_3O_{7-\delta}$ (YBCO) films are left in the atmosphere, their electrical characteristics deteriorate: the critical temperature T_c and current density j_c decrease and the resistivity increases.[1,2] Chemical reactions with carbon dioxide and water lead to the formation of amorphous layers on the surface of the samples, while interaction with water reduces the oxygen concentration in the YBCO crystal structure.[1] Degradation takes place particularly rapidly when water condenses on the surface of the films.[2] The deposition of silver[3] and polymer[4] coatings significantly slows this degradation.

For many applications of high-temperature superconducting films, including radio engineering, a dielectric protective coating is required with low losses in alternating electromagnetic fields. From the technological viewpoint, it is desirable for the protective coating to allow oxygen to pass through at the temperatures of 400–500 °C used for oxidizing heat treatment, so that the oxygen concentration in the YBCO film can be corrected.

A suitable material in this respect is zirconium oxide stabilized in the cubic phase with yttrium oxide (YSZ). This YSZ is inert with respect to YBCO and is frequently used as a substrate material for the growth of high-temperature superconducting films. As a result of the presence of structural vacancies in the oxygen sublattice, YSZ has a high ionic conductivity (O^{-2} ion carriers) and a high oxygen diffusion coefficient for simple oxides.[5]

In order to identify the protective properties of YSZ, we used single-crystal *c*-oriented YBCO films 0.15 μm thick, grown by off-axis dc magnetron sputtering of a stoichiometric target on sapphire [1102] substrates with an epitaxial CeO_2 buffer layer. The reaction mixture consisted of argon and oxygen in the ratio 2:1, the total pressure was 30 Pa, and the substrate temperature 710 °C. The parameters of the films obtained under these conditions with optimized cooling were $T_c = 87–89$ K, $\delta T_c \approx 0.8$ K, $j_c(77\ \text{K}) \geqslant 10^6$ A/cm^2 (from resistive measurements), and the ratio $R(300\ \text{K})/R(100\ \text{K}) = 2.9–3$. These films contain copper-enriched particles with maximum sizes up to 1 μm and density $N \approx 2 \times 10^7$ cm^{-2}, which protrude above the surface of the films. Gold contact areas were preliminarily deposited on the substrate and their surfaces were partially masked off during the deposition of YBCO. Tracks 3–5 mm long and 1.5–3 mm wide were scribed onto the films.

In another method, magnetron sputtering of a Zr + 22 wt.%Y metal target in a conventional geometry was used to deposit YSZ films on samples heated to 400 °C in an oxygen environment at $P = 2$ Pa. Directly before deposition of the YSZ, the samples were held for ≈20 min at this temperature and pressure. This deposition regime was selected for the protective coating first, to achieve satisfactory adhesion between the YSZ layer and the YBCO film and second, to remove moisture sorbed by the film at the previous stages of preparation and storage. Fetisov[6] observed that dehydration is most efficient when heat treatment is near the tetra–ortho transition point.

In order to avoid degradation of the film near the electrode as a result of the electromigration of copper and oxygen ions accompanying the passage of electric current,[7] the four-contact resistive measurements were made using an alternating current (240 Hz, 10 μA).

Ivanov *et al.*[8] showed that the resistance of $YBa_2Cu_3O_{7-\delta}$ with a constant oxygen content in the crystal lattice is linear with respect to temperature as far as the melting point and the slope increases with increasing δ. This means that by continuously monitoring the resistance during heat treatment, we can determine whether oxygen enters or leaves the lattice by looking at the deviation from linearity.

When measuring the resistance of the unprotected films as a function of temperature under optimized oxidizing heat treatment, we observed that even a slight amount of moisture causes an appreciable increase in their resistance during heating in dried oxygen (dew point −48 °C) at $T > 240$ °C (curve *1* in Fig. 1). When the films were heated at a rate of 15 deg/min, similar anomalous resistance peaks were observed after holding the film at room temperature for several hours in the laboratory atmosphere. The resistance at lower temperatures, T_c, and δT_c remain unchanged. More pronounced anomalous peaks were observed after the films had been heated from liquid-nitrogen temperatures or held briefly above the surface of boiling water. Heat treatment and storage of the samples in dried oxygen results in a standard temperature dependence of the resistance (curve *2* in Fig. 1). We attribute the anomalous increase in the resistance of the

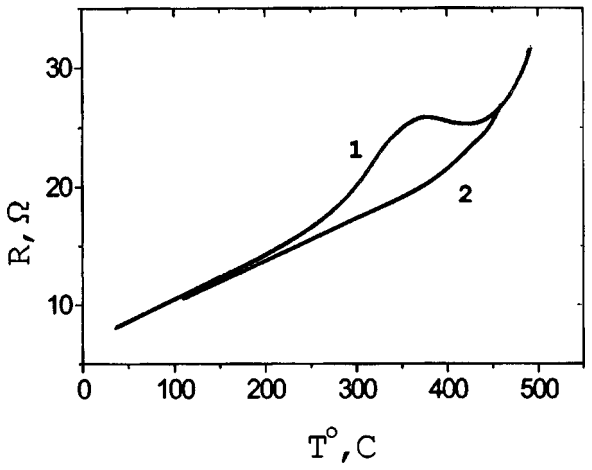

FIG. 1. Electrical resistance of YBCO film heated in dried oxygen: *1* — containing moisture, *2* — previously dehydrated.

films to a reduced oxygen content in the YBCO lattice as a result of a heat-intensified reaction with the water in the compound. We used this sensitivity of the resistance to the presence of moisture traces in the film to estimate the protective properties of the coating.

Protected YBCO films were subjected to treatment in which they were held five times in boiling water vapor and thermal cycling in which they were cooled to liquid nitrogen temperature and then warmed to room temperature. In both cases, moisture condensed on the surface of the samples. The temperature behavior of the resistance remained the same after these treatments and corresponded to curve *2*, while the superconducting parameters $T_c, \delta T_c$, and j_c (77 K) corresponded to the initial values.

These characteristics of YSZ films on high-temperature superconductors provide evidence that they allow oxygen from the atmosphere to pass into the protected YBCO film. The times needed to attain an equilibrium oxygen content at temperatures $T \approx 380\,^{\circ}\mathrm{C}$ for high-temperature superconducting films with and without a 40 nm YSZ protective coating are similar. However, after heating in oxygen above 400° the protective properties of the coatings deteriorated, and after control treatment over boiling water the temperature dependence of the resistance was described by curve *1*. It can be seen from the figure that at these temperatures the resistance increases faster than linear as a result of the reduced oxygen content in the YBCO. The release of oxygen from the high-temperature superconductor causes separation or impairs the continuity of the YSZ film. This behavior may be caused by the presence of a layer (or sections) of chemical reaction products on the surface of the YBCO film, where oxygen may be present in molecular form (Fig. 2).

If the YSZ and YBCO films are in direct contact (central section in Fig. 2), oxygen penetrates into the superconductor

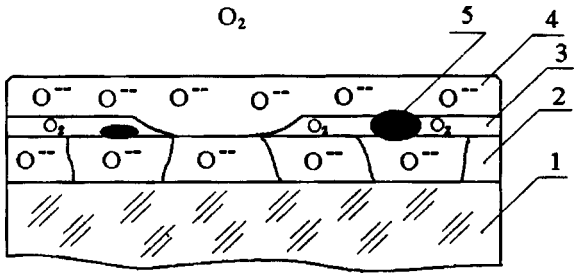

FIG. 2. Layer-by-layer model of structure: *1* — substrate, *2* — YBCO film, *3* — layer of chemical reaction products, *4* — YSZ film, and *5* — copper-enriched particles.

from the atmosphere in several stages (see Ref. 9, for example), i.e., reactions at the outer YSZ surface $O_2 \rightarrow 2O$ (*1*), $2O = 4e^- \rightarrow 2O^{2-}$ (*2*), transport of oxygen ions through the YSZ film, and passage across the interface $O^{2-}(\mathrm{YSZ}) \rightarrow O^{2-}$ (YBCO) (*3*), and subsequent transport through the superconductor. In sections of the structure where there are layers of chemical reaction products with a lower conductivity for oxygen ions, the reverse and forward reactions (*1*) and (*2*) should take place on the upper and lower surfaces of these layers, respectively, accompanied by the generation of molecular oxygen inside the structure. When oxygen leaves the superconductor, the reverse process takes place. In order to achieve a net outward oxygen flux, the pressure of the molecular oxygen inside the structure should be higher than the external pressure, which destroys the protective film.

Tests on protective layers 40 and 80 nm thick revealed no differences in their behavior. Thus, thin YSZ layers effectively protect rough $YBa_2Cu_3O_{7-\delta}$ films from atmospheric degradation. Their performance is maintained in oxidizing processes which do not reduce the oxygen content in the protected superconductor.

[1] V. I. Nefedov and A. N. Sokolov, Zh. Neorg. Khim. **34**, 2723 (1989).
[2] G. Watson, S. A. Holt, R.-P. Zhao *et al.*, Physica C **243**, 123 (1995).
[3] E. A. Protasov, I. V. Sobakin, Yu. P. Skopintsev, and A. A. Ivanov, Pis'ma Zh. Tekh. Fiz. **16**(17), 86 (1990) [Sov. Tech. Phys. Lett. **16**, 679 (1990)].
[4] S. Morohashi, H. Tamura, A. Yoshida, and S. Hasuo, Appl. Phys. Lett. **52**, 1897 (1988).
[5] J. Hladic (Ed.), *Physics of Electrolytes*, Vol. 1 (Academic Press, New York, 1972), Chap. 8.
[6] A. V. Fetisov, Neorg. Mater. **33**, 1360 (1997).
[7] G. N. Mikhaĭlova, V. M. Mukhortov *et al.*, Sverkhprovodimost' (KIAE), **5**(12), 2304 (1992).
[8] V. V. Ivanov, Yu. A. Kotov, G. A. Mesyats, S. N. Paranin, *Electrical Resistance of the High-Temperature Superconducting Ceramic* $YBa_2Cu_3O_{7-\delta}$ *Under Pulsed Microwave Heating.* Series of preprints of scientific reports ''Problems of High-Temperature Superconductivity'' [in Russian], Komi Scientific Center—Sverdlovsk Scientific Center, Urals Branch of the Russian Academy of Sciences, No. 12 (1989), 16 pp.
[9] H. Huang and C. R. M. Grovenor, Physica C **210**, 87 (1993).

Translated by R. M. Durham

Band-pass microstripe filters using high-temperature superconducting films

I. B. Vendik, V. V. Kondrat'ev, A. A. Svishchev, S. Leppyavuori, and É. Yakku

St. Petersburg State Electrotechnical University
(Submitted July 7, 1998)
Pis'ma Zh. Tekh. Fiz. **24**, 50–54 (December 26, 1998)

Results are presented of a simulation and experimental investigation of band-pass filters consisting of coupled microstripe resonators fabricated using high-temperature superconducting films. It was shown that by using reliable models of high-temperature superconducting filter elements and careful design, it is possible to synthesize high-temperature superconducting filters as an integrated circuit without using additional tuning elements. Two filter configurations were investigated at a frequency of 1.75 GHz with a 4% pass band. A significant result is that the calculated and experimental characteristics of both filter configurations show very satisfactory agreement. © *1998 American Institute of Physics.*
[S1063-7850(98)02612-3]

High-temperature superconducting (HTSC) films on a dielectric substrate can be successfully used to fabricate planar microwave filters with the lowest pass-band losses yet recorded. This can be attributed to the extremely low surface resistance of these HTSC films at liquid-nitrogen temperatures ($T=77$ K). Since planar band-pass filters are made from coupled half-wave or quarter-wave resonators, the method of synthesizing these filters is based on a model of multiply connected lines. Here we report results of a simulation and experimental investigation of band-pass filters consisting of coupled microstripe resonators fabricated using YBCO films on an $LaAlO_3$ substrate with a permittivity of 23.7 (PRIMA TEC films, $R_{sur}=0.6$ mΩ at $T=77$ K, $f=10$ GHz, and film thickness 400–500 nm).

The generally held view is that narrow-band, steeply sloping HTSC filters cannot be fabricated without additional tuning. Here we show that by using reliable models of HTSC filter elements and careful design, it is possible to synthesize HTSC filters as an integrated circuit without additional tuning elements. This problem is important for the large-scale application of these filters to mobile communications systems.

We investigated two filter configurations at a frequency of 1.75 GHz with a 4% pass band. One tenth-order filter, No. 1, was fabricated as an array of coupled half-wave microstripe resonators using a T-shaped exciting-element structure (Fig. 1a) on an $LaAlO_3$ substrate 0.45 mm thick and 2 in. in diameter. The 1.1 mm wide half-wave resonators were spaced at different intervals, selected in the design process to ensure the same coupling coefficients as for the prototype filter using lumped L–C elements.[1]

Another tenth-order filter, No. 2, was also fabricated as an array of coupled half-wave resonators (Fig. 1b) on the same substrate using coupled lines as exciting elements. The width of the microstripe resonator lines was the same as that for filter No. 1. The relative position of the half-wave resonators was modified in order to suppress coupling between nonadjacent resonators, which makes the low-frequency slope of the amplitude–frequency characteristic less steep.

The filter characteristics were calculated using various commercial programs (Sonnet, Jomega, MH) and also using our own model of multiply connected lines, which takes into account the surface impedance of the YBCO film and its frequency and temperature dependences. An empirical model of the surface impedance of HTSC films was used.[2]

The filters were investigated experimentally at liquid-nitrogen temperature $T=77$ K using an HP network analyzer. The experimental characteristics of the filters are given in Fig. 2 together with the calculated characteristics. The insertion losses in the pass band are less than 0.5 dB, the

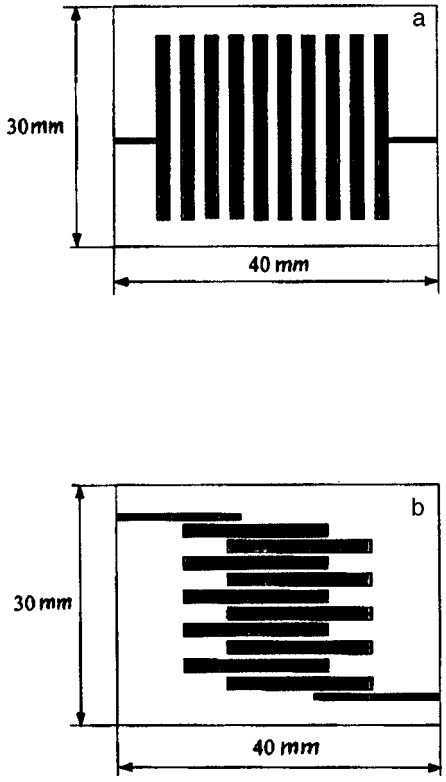

FIG. 1. Topology of the filters studied.

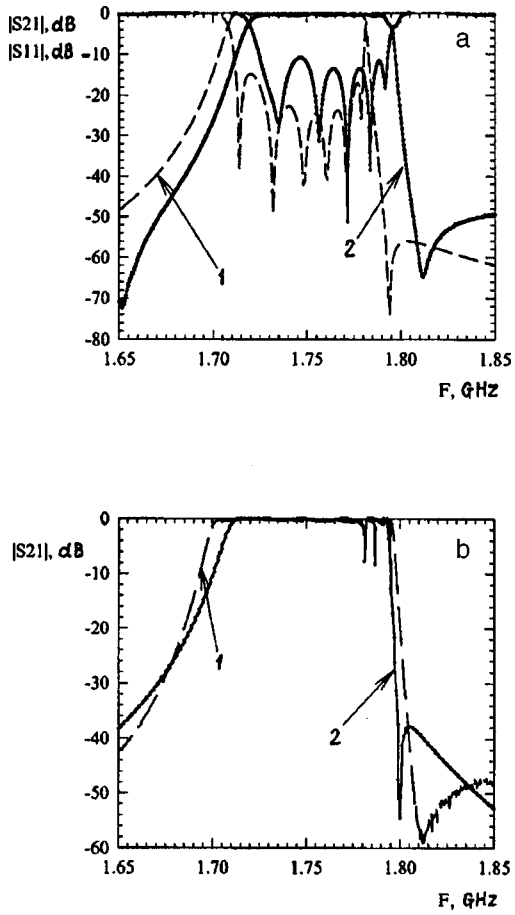

FIG. 2. Experimental and calculated characteristics of filter No. 1 (a) and filter No. 2 (b): *1* — calculations, *2* — experiment.

reflection coefficient is better than 12 dB, and the minimum level of isolation in the stop band is 50 dB. For comparison, Fig. 3 gives the experimental characteristics of filter No. 1 fabricated using YBCO film and its copper analog.

A significant result is that the calculated and experimental characteristics of both filter configurations show very satisfactory agreement. In addition, for filter No. 2 the steepness of the low-frequency slope is increased with the parasitic coupling between nonadjacent resonators partially suppressed. Figure 3 shows that the quality of the HTSC filters is substantially better than that of the copper analog.

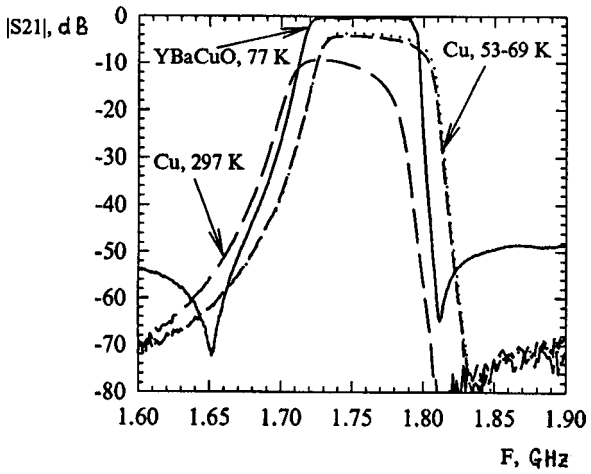

FIG. 3. Experimental characteristics of filter No. 1 fabricated using copper and YBaCuO superconducting film.

This work was carried out under Project No. 98063 of the State Scientific and Technical Program ''Topical Problems in the Physics of Condensed Media'' ''Superconductivity'' and received financial support from the Nokia Foundation.

[1] D. Zhang, G.-C. Liang, C. F. Shin *et al.*, IEEE Trans. Microwave Theory Tech. **43**, 3020 (1995).
[2] G. L. Matthaei and G. L. Hey-Shipton, in *Digest of the International IEEE Microwave Symposium*, Atlanta, GA, 1993, pp. 1269–1272.
[3] O. G. Vendik, I. B. Vendik, and D. I. Kaparkov, IEEE Trans. Microwave Theory Tech. **46**, 469 (1998).

Translated by R. M. Durham

Optimizing the output characteristics of holograms in a $Bi_{12}SiO_{20}$ crystal by selecting the orientation of the crystal and the polarization of the readout light

V. V. Shepelevich and P. P. Khomutovskiĭ

Mozyr State Pedagogical Institute
(Submitted February 4, 1998)
Pis'ma Zh. Tekh. Fiz. **24**, 55–60 (December 26, 1998)

An investigation was made of the orientation angle θ^m for which the diffraction efficiency of a hologram recorded in a $Bi_{12}SiO_{20}$ crystal has a maximum, as a function of the crystal thickness d. It is shown that the optical activity and piezoelectric effect qualitatively alter the behavior of the dependences $\theta^m(d)$. © *1998 American Institute of Physics.* [S1063-7850(98)02712-8]

Topics associated with optimizing the output characteristics of holograms recorded in cubic refractive crystals have been examined in various studies (for example, Refs. 1–8). Petrov *et al.*[1] determined the polarization azimuth of a linearly polarized readout beam which maximizes the diffraction efficiency of a hologram in a $Bi_{12}SiO_{20}$ (BSO) crystal of thickness $d \approx 2$ mm for two orientations of the holographic grating vector: $\mathbf{K} \| [001]$ and $\mathbf{K} \perp [001]$. Mallick *et al.*[2,3] derived analytic expressions for the azimuth of the readout beam for which the hologram gain has the highest values for the same orientations of the holographic grating vector. Shepelevich and Khramovich[4] made an analytic study of the possibility of optimizing the diffraction efficiency of a hologram by correctly selecting the orientation angle.

The first experimental and theoretical study of the photoelastic contribution to the photorefractive effect in cubic crystals was made by Stepanov *et al.*[5] Odoulov *et al.*[6] reported an experimental investigation of the gain in two-wave mixing as a function of the orientation of the holographic grating vector in a cubic GdTe:Ge crystal in order to optimize the energy exchange between the light waves.

Possibilities for optimizing the diffraction efficiency of holograms recorded in cubic optically active piezocrystals were examined by Shepelevich *et al.*,[7,8] who obtained the experimental and theoretical dependence of the maximum diffraction efficiency on the orientation angle.

The aim of the present study is to investigate the maximum diffraction efficiency η^m of a hologram as a function of the BSO crystal thickness, to determine the influence of the optical activity and piezoelectric properties of the crystal on the behavior of this dependence, and also to find the crystal orientations which give the maximum diffraction efficiency.

Let us assume that a noninclined transmission holographic grating is recorded in a (110) cut crystal using a standard two-wave mixing scheme[9] and is read by a reference wave R. In this case, the approach described in Refs. 7 and 8 can be used to determine the orientation angle $\theta = \theta^m$ formed by the vector $\mathbf{K}$ of the holographic grating to the [001] crystallographic direction which gives the maximum diffraction efficiency $\eta = \eta^m$ for a specific fixed azimuth $\psi_0 = \psi_0^m$ of a linearly polarized reference wave.

Figure 1 gives the dependences $\theta^m(d)$ for four cases. Curve *1* ($\theta \approx 53°$) was obtained for a photorefractive crystal which exhibits no piezoelectric effect or optical activity. Curve *2* ($\theta \approx 54°$) allows for a piezoelectric effect (combined with photoelasticity), but no optical activity was taken into account. Curve *3* was plotted with allowance for the optical activity of the crystal but neglecting the piezoelectric effect. Curve *4* describes the case of a real BSO crystal in which all these effects appear simultaneously.

All the calculations were made for the following BSO crystal parameters:[9] photoelastic constants $p_1 = -0.16$, $p_2 = -0.13$, $p_3 = -0.12$, $p_4 = -0.015$, electrooptic coefficient $r_{41} = -5.0 \times 10^{-12}$ mV, coefficients of elasticity $c_1 = 12.96 \times 10^{-10}$ N/m^2, $c_2 = 2.99 \times 10^{-10}$ N/m^2, $c_3 = 2.45 \times 10^{-10}$ N/m^2, refractive index $n = 2.54$, piezoelectric coefficient $e_{14} = 1.12$ C/m^2, and specific rotation $\alpha = 0.372$ rad/mm. It is also assumed that the wavelength of the light used is $\lambda = 0.6328\ \mu$m, the Bragg angle inside the

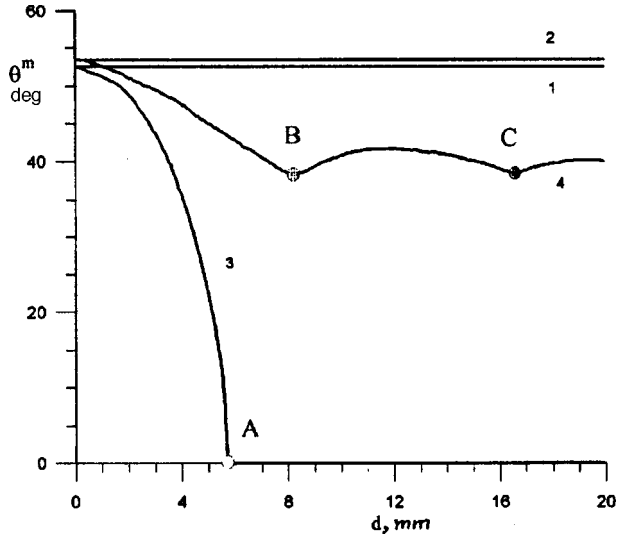

FIG. 1. Orientation angle θ^m versus crystal thickness d: *1* — neglecting the piezoelectric effect and optical activity, *2* — allowing for the piezoelectric effect, *3* — allowing for optical activity, and *4* — allowing for the piezoelectric effect and the optical activity.

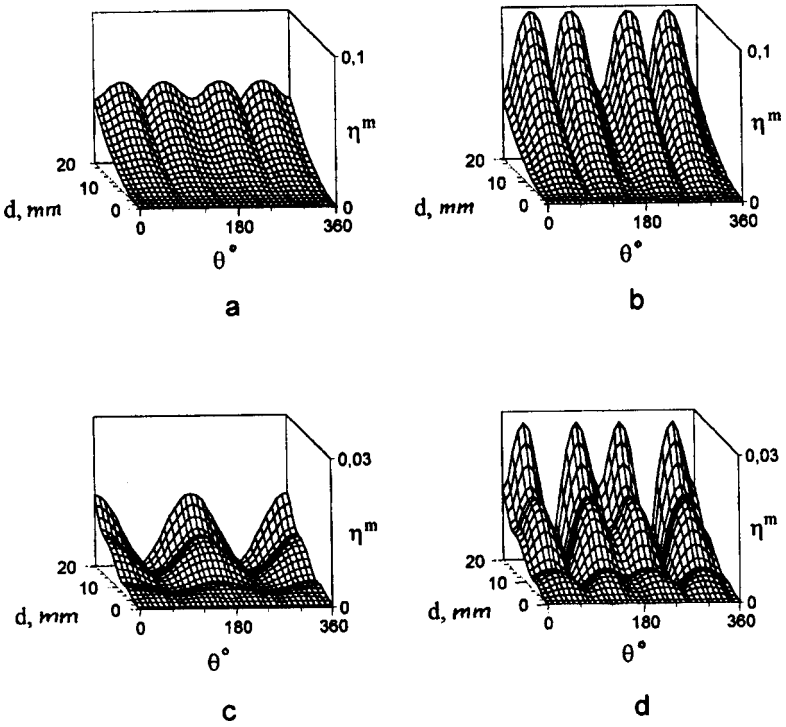

FIG. 2. Dependence of η^m on the orientation angle θ and the crystal thickness d: a — neglecting the piezoelectric effect and the optical activity, b — allowing for the piezoelectric effect, c — allowing for the optical activity, and d — allowing for the piezoelectric effect and the optical activity.

crystal is $\varphi=11°$, and the amplitude of the grating electric field is $E=0.5$ kV/cm.

We can see that allowance for the piezoelectric effect ''shifts'' the value of θ^m toward larger angles. Allowance for the optical activity leads to a sharp drop in the angle θ^m as the crystal thickness increases and at a certain critical thickness ($d\approx 5.7$ mm) θ^m is zero (point A) and remains unchanged as d increases further. Allowance for both the optical activity and the piezoelectric effect causes θ^m to decrease with increasing thickness d, but at point B ($d\approx 8$ mm), which corresponds to rotation of the plane of polarization through 180°, θ^m starts to increase again before decreasing to point C ($d\approx 16$ mm), which corresponds to rotation of the plane of polarization through 360°, and so on.

Since the three-dimensional graphs of the maximum diffraction efficiency as a function of the angle θ and crystal thickness d contain four ''humps'' of the same height, two of which merge into one at $d\approx 5.7$ mm (Fig. 2), it is interesting to plot the dependence $\theta^m(d)$ (Fig. 3) for all four humps.

Note that similar curves can be plotted for values of θ^m which correspond to the maxima relative to the intensity of one of the waves in the two-wave mixing. In this case, the lower and upper series of curves plotted in Fig. 3 will be observed. The two internal series of curves near the angle $\theta=180°$ will correspond to minimum energy exchange from the R to the S wave.

It is easy to show that for small Bragg angles neglecting the piezoelectric effect, these results are the same as those of Ref. 10, where curve *1* corresponds to the [111] direction ($\theta\approx 55°$).

To sum up, we have established that the dependence $\theta^m(d)$ shows substantial qualitative changes under the influence of the piezoelectric effect and optical activity.

The authors are grateful to N. N. Egorov for useful discussions of the results.

We would like to thank the Ministry of Education of the Republic of Belarus for supporting this work.

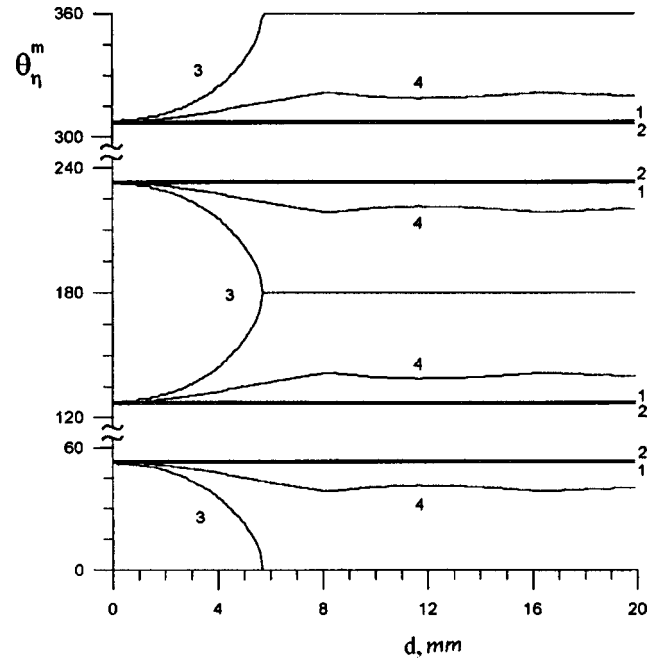

FIG. 3. Orientation angle θ^m versus crystal thickness d: *1* — neglecting the piezoelectric effect and optical activity, *2* — allowing for the piezoelectric effect, *3* — allowing for the optical activity, and *4* — allowing for the piezoelectric effect and the optical activity.

[1] M. P. Petrov, T. G. Pencheva, and S. I. Stepanov, J. Opt. (Paris) **12**, 287 (1981).
[2] S. Mallick and D. Rouede, Appl. Phys. B: Photophys. Laser Chem. **43**, 239 (1987).

[3] S. Mallick, D. Rouede, and A. G. Apostolidis, J. Opt. Soc. Am. B **4**, 1247 (1987).
[4] V. V. Shepelevich, and E. M. Khramovich, Opt. Spektrosk. **65**, 403 (1988) [Opt. Spectrosc. **65**, 240 (1988)].
[5] S. I. Stepanov, S. M. Shandarov, and N. D. Khat'kov, Fiz. Tverd. Tela (Leningrad) **29**, 3054 (1987) [Sov. Phys. Solid State **29**, 1754 (1987)].
[6] S. G. Odulov, S. S. Slusarenko, and K. V. Scherbin, Pis'ma Zh. Tekh. Fiz. **15** (6), 10 (1991) [Sov. Tech. Phys. Lett. **15**, 417 (1991)].
[7] A. E. Mandel', S. M. Shandarov, and V. V. Shepelevich, Pis'ma Zh. Tekh. Fiz. **14**, 2147 (1988) [Sov. Tech. Phys. Lett. **14**, 932 (1988)].
[8] V. V. Shepelevich, S. M. Shandarov, and A. E. Mandel, Ferroelectrics **110**, 235 (1990).
[9] V. V. Shepelevich, N. N. Egorov, and V. Shepelevich, J. Opt. Soc. Am. B **11**, 1394 (1994).
[10] E. M. Khramovich, *Diffraction of Light at Photoinduced Gratings in Cubic Gyrotropic Photorefractive Crystals*, Dissertation for Candidate of Physical-Material Science [in Russian], Minsk, (1990), 170 pp.

Translated by R. M. Durham

Optical properties of an ''anomalous'' droplet

B. A. Bezuglyĭ, S. V. Shepelenok, and N. A. Ivanova

Tyumen State University
(Submitted June 29, 1998)
Pis'ma Zh. Tekh. Fiz. **24**, 61–64 (December 26, 1998)

A varifocal self-centering microlens using light-induced concentration-capillary convection has been developed for the first time. Measurements were made of the focal length as a function of the control beam power. The rates of self-centering and shape rearrangement of the microlens were estimated. © *1998 American Institute of Physics.* [S1063-7850(98)02812-2]

The idea of using liquids to construct optical elements with controllable characteristics goes back to Newton, who suggested using the surface of mercury in a rotating container as a parabolic mirror. Such progress has now been made in this field that liquid metal telescopes with a mirror diameter of 4 m are now operating successfully.[1]

In 1958, Block and Harwit[2] suggested using the thermocapillary-deformed free surface of a liquid as an optical element. The phenomenon of self-focusing of laser radiation observed when an incident beam is reflected from a thermocapillary deformed liquid layer was studied in Refs. 3–6.

Following the discovery of concentration-capillary convection induced by the thermal action of light in thin films of solutions of positively strain-active substances[1)] in highly volatile solvents, it was suggested that the ''anomalous'' droplet[5] formed as a result of this effect could be used as a varifocal liquid lens. Bezuglyi[7] showed that a steady-state anomalous droplet could be achieved, and this was confirmed experimentally[8] using a mixture of acetone and a saturated solution of rhodamine G in water.

In the work reported here an anomalous droplet was obtained using a 7.3 g/l solution of iodine in 96% ethanol, where the strain-active component was the water contained in the ethanol. The experimental solution was pumped into a hermetically sealed cell, which was heated from above to prevent condensation of the vapor.

The control beam used to produce the droplet was formed by an optical system consisting of a light source (HBO-100 mercury lamp), a collector, a mirror, and a condenser. The liquid lens and also the image of the objected constructed by it were observed using a microscope. The optical beam power P was varied between 48 and 200 mW by using neutral light filters.

At powers $P<48$ mW the centripetal flow of liquid almost ceased, the droplet, being no longer confined by the beam, escaped and dispersed.

The shape of the lens surface depended on the beam power. As the radiation power increased, the diameter and focal length f of the lens decreased due to reduction in the radius of curvature of the surface (caused by the increased surface tension) and owing to the reduction in its volume (caused by evaporation of the solvent). However, as the beam power decreased, the diameter of the lens and its focal length f increased as a result of an inflow of solvent via the substrate and an increase in the volume of the lens, and also because of the increased radius of curvature of its surface (because of the lower surface tension). The diameter of the lens varied between 325 and 130 μm when the power P increased from 48 to 200 mW, respectively.

Figure 1 gives f as a function of the beam power P. The focal length f was calculated using the formula

$$f=d'a/(d'+d),$$

where a is the distance between the object (a control grid with square cells) and the liquid microlens, d is the size (side length) of the cell (0.391 mm), and d' is the size of the cell image constructed using the liquid microlens.

Note that this lens possesses self-centering properties. When the beam is displaced over a distance less than its diameter, the lens strives to occupy that position in the beam in which its optic axis passes through the point of maximum beam intensity.

When the beam is displaced abruptly over an appreciable distance (up to twice the beam diameter), the lens becomes distorted during the outflow process in such a way that a pseudopod moves in the direction of the new position of the beam and is rapidly drawn into the beam, entraining the body of the lens. This self-searching of the beam and return of the system to the working state may be called beam ''tracking'' (Fig. 2).

The self-centering time was taken to be the time taken for the droplet to move into the beam as a result of an instantaneous displacement of the beam over a distance equal

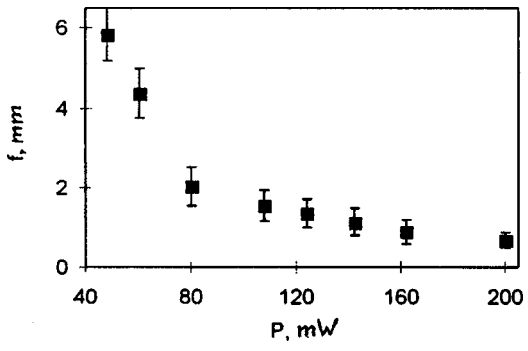

FIG. 1. Focal length of lens versus control beam power.

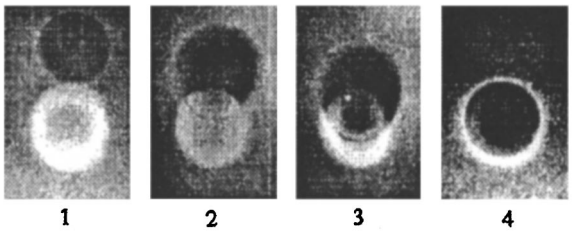

FIG. 2. The light beam is displaced over a distance equal to its diameter (1) and the droplet (2,3) moves in the direction of the new beam position (4).

to its diameter. This was found to be 1–5 s, with the minimum corresponding to a power of 200 mW and the maximum corresponding to 80 mW. The time taken for complete rearrangement of the lens when the optical flux varied between 200 and 142 mW was 3–4 s and did not exceed 10 s when this varied between 200 and 89 mW.

From these experimental results, we can conclude that a liquid microlens fabricated using an iodine : ethanol solution has the following properties:

It has high rates of self-centering and shape rearrangement when the control beam power is varied;

It has smaller dimensions than a liquid lens obtained using a mixture of solutions of rhodamine G in water and rhodamine G in acetone;[6]

It can be used to fabricate an adaptive optical device whose parameters can be controlled by varying the control beam intensity.

This work was supported by Grant No. 15-98 from Tyumen State University.

[1)]A positively strain-active substance is the less volatile component of a solution or mixture with whose increasing concentration the surface tension of the liquid increases.

[1] P. Hickson, E. F. Borra, R. Cabanak *et al.*, Astrophys. J. **436**, L201 (1994).
[2] M. J. Block and M. Harwit, J. Opt. Soc. Am. **48**, 480 (1958).
[3] G. Da Costa and J. Calatroni, Appl. Opt. **18**, 233 (1979).
[4] G. Da Costa, Phys. Lett. **80**, 320 (1980).
[5] B. A. Bezuglyĭ, Candidate's Dissertation [in Russian], Moscow State University, Moscow (1983), 270 pp.
[6] S. F. Viznyuk, and A. T. Sukhodol'skiĭ, Kvantovaya Élektron. (Moscow) **15**, 767 (1988) [Sov. J. Quantum Electron. **18**, 489 (1988)].
[7] B. A. Bezuglyi, in *Proceedings of the First International Symposium on Hydromechanics, Heat/Mass Transfer Microgr*, Perm–Moscow, Russia, July 1991 (Gordon and Breach, Amsterdam, 1992), pp. 335–340.
[8] B. A. Bezuglyi, S. V. Shepelenok, and O. A. Tarasov, *Adaptive Optical Device Based on Liquid Lens*, in *Abstracts of the International Aerospace Congress, IAC'97*, Moscow, 1997 (STC ''Petrovka,'' 1997), Vol. 1, p. 245.

Translated by R. M. Durham

Recording of high-energy cosmic rays by observation of the radio signal reflected from the ionosphere

A. D. Filonenko

East Ukrainian State University, Lugansk
(Submitted August 19, 1997; resubmitted April 8, 1998)
Pis'ma Zh. Tekh. Fiz. **24**, 65–68 (December 26, 1998)

Feasibility is shown for a method of detecting superhigh-energy ($>10^{22}$ eV) cosmic rays on the surface of Antarctica with an event rate acceptable for observation purposes. This situation can be attributed to various favorable circumstances such as 1) the large area of the continent (10^6-10^7 km^2); 2) the location of the vast majority of the ice cap at an altitude of 3–4 km; 3) the low level of atmospheric noise because this area is as far as possible from the equatorial thunderstorm belt; and 4) the effective band of the radio pulse frequency spectrum (0–7 MHz) not exceeding the highest frequencies used. Estimates of the electromagnetic pulse intensity were made using previously published studies.[1–6] [S1063-7850(98)02912-7]

The study of cosmic rays with energies $W_0>10^{20}$ eV is closely tied to the solution of various fundamental problems, although over the entire history of this research the number of detected events with this energy scarcely exceeds ten. This is because of the extremely low intensity of the cosmic rays in this energy range (for $W_0\geqslant 10^{20}$ eV there is approximately one event per square kilometer per century).

This scenario has naturally provided the impetus for the design of enormous detectors with working areas of more than a thousand square kilometers, such as EAS-1000 or the Auger project with an area of 6000 km^2 and costing around 100 million dollars. However, even these giants raise the energy ''ceiling'' only by an order of magnitude. It is therefore appropriate to search for new methods of detecting superhigh-energy cosmic rays. One such method which the present author considers to be promising is the radio detection method, which is not related to the Earth's magnetic field. Estimates show[1–4] that the electron–photon shower produced by a high-energy cosmic particle generates a powerful radio pulse with a broad spatial angular distribution whose amplitude is mainly attributed to the coherent radiation from δ-electrons in this shower. The minimum wavelength $\lambda_{\min}$ of this coherent radiation should be at least twice the path length of the electron–photon shower in the material. It was also noted that particles having energies of the order of $10^{22}-10^{23}$ eV, passing through the surface of the Moon, produce such a powerful radio pulse that this can be reliably detected using a radio telescope on Earth.[5]

Moreover, if the receiving antennas are positioned on artificial lunar satellites, it is possible not only to detect the existence of $10^{20}-10^{23}$ eV cosmic particles but also to determine their direction of incidence.[6] However, it is advisable to carry out preliminary experiments, without going into space, as reported for example, in Ref. 5. There is also another possibility, which derives from the fact that the vast majority of the Antarctic ice cap is located at an altitude of around 3.5 km above sea level. It is easily established that under these conditions, the path covered by a vertical shower having the initial energy $W_0=10^{22}-10^{23}$ eV in the atmosphere is only around 18 t-units (the complete atmosphere is 28 t-units from sea level) and the maximum of a shower of this energy should be located at a depth of 35 t-units, i.e., approximately 2 km below sea level (see Ref. 7, for example).

In other words, even an oblique shower only begins to develop at the surface of the ice ($S\approx 0.7$) with the number of particles at this stage being approximately an order of magnitude lower than that at the maximum, but the effective part of the shower (from the point of view of the number of particles in it) will pass completely through the ice. These estimates hold even when the angle of inclination of the shower is 30°. Elementary estimates also show that the shower path length L_s over which its number of particles varies severalfold is approximately 20 t-units or $L_s\approx 7.5$ m for ice. Neglecting the closeness of the ice surface to the radiation source ($h\sim\lambda$), the length L of an electromagnetic pulse entering the atmosphere (for example, for a vertical shower) will be given by $L=L_s(\sqrt{\varepsilon-\sin^2\alpha}+1)$, where $\varepsilon\approx 3$ is the permittivity of ice,[8] and α is the angle between the direction of emission and the vertical, and for an average angle of $\alpha=45°$ we find $L=20$ m. This implies that coherent reception can be accomplished at wavelengths $\lambda_{\min}>2L>40$ m.

Since at frequencies of the order of a few megahertz the loss tangent for ice[8] is $\tan\delta\approx 0.2$, the refractive index

$$\varkappa=[\varepsilon/2\,(1+\tan^2\delta)^{\frac{1}{2}}-1]^{\frac{1}{2}}$$

is approximately 0.18 and the wave amplitude decays e times over the path length $l\geqslant c/\omega\varkappa\approx 25$ m. This is substantially greater than L_s, so absorption of radiation in the ice can be neglected over this path. The spatial diagram of this radiation is similar to a Hertz dipole diagram[4] and thus waves will be emitted with fairly high intensity at both low and high angles to the horizon. This factor creates favorable conditions for

almost lossless detection of waves reflected from the ionosphere over almost the entire continent. The rest of the radiation will be absorbed by the ice (see above) and is of no interest from the point of view of detecting the particles.

If an initial particle has the energy $W_0 \sim 10^{23}$ eV, the field of the electromagnetic pulse produced by an electron–photon shower at a distance of 1000 km will be around 10^3 mcV/mMHz. This is an extremely high field strength and for comparison it is sufficient to note that, according to data given by several research groups,[9] the experimentally detected electric field strength of a radio pulse produced by the interaction between an extensive air shower and the Earth's magnetic field was only around 10 mcV/mMHz in the frequency range with the highest radiation intensity (~ 30 MHz). When carrying out this type of experiment in which a radio signal reflected from the ionosphere is detected, we need to bear in mind its state in this geographical region and the predicted maximum frequencies used λ_c.

The field strength of the radio signal from cosmic particles having energies of the order $W_0 \geqslant 10^{22}$ eV is ten times lower at the same distance from the source. However, over this area the total flux of cosmic rays having this energy is presumably more than 1.5–2 orders of magnitude greater than that for the energy range $W_0 \sim 10^{23}$ eV. This means that with almost no change in the frequency of events (relative to $W_0 = 10^{23}$ eV), the area to be monitored can be reduced by the same amount, which then necessitates detecting radio pulses whose radiation is directed at a substantially larger angle to the horizon. In this case λ_c is reduced, but even in August, λ_c at these latitudes is 3–4 MHz, i.e., when the radio wave is vertically incident on the ionosphere (see Ref. 10, for instance).

It should be noted in conclusion that the method of detecting ultrahigh-energy cosmic rays by detecting a radio signal reflected from the ionosphere has the same shortcoming as that using a radio telescope,[5] i.e., it is impossible to determine the direction of incidence of a cosmic particle because of the uncontrollable rotation of the plane of polarization of the radiowave caused by its interaction with the plasma in the Earth's magnetic field. This shortcoming is caused by unstable conditions in the upper layers of the atmosphere and evidently cannot be compensated. However, both these methods can give some idea of the energy spectrum of the cosmic rays in this energy range, which is not only useful information in itself but is also required to plan experiments for the detection of superhigh-energy cosmic rays.

[1] P. I. Golubnichiĭ and A. D. Filonenko, Pis'ma Zh. Tekh. Fiz. **20**(12), 57 (1994) [Tech. Phys. Lett. **20**, 499 (1994)].
[2] P. I. Golubnichiĭ and A. D. Filonenko, Pis'ma Zh. Tekh. Fiz. **20**(23), 59 (1994) [Tech. Phys. Lett. **20**, 960 (1994)].
[3] P. I. Golubnichiĭ and A. D. Filonenko, Ukr. Fiz. Zh. **41**, 696 (1996).
[4] P. I. Golubnichiĭ, A. D. Filonenko, and V. I. Yakovlev, Izv. Ross. Akad. Nauk, Ser. Fiz. **58**(12), 115 (1994).
[5] A. D. Filonenko, Izv. Ross. Akad. Nauk, Ser. Fiz. **61**(3) (1997).
[6] A. D. Filonenko, Pis'ma Zh. Tekh. Fiz. **23**(10), 57 (1997) [Tech. Phys. Lett. **23**, 399 (1997)].
[7] S. Z. Belen'kiĭ, *Avalanche Processes in Cosmic Rays* [in Russian], Gostekhizdat, Moscow (1948), 243 pp.
[8] G. W. C. Kaye and T. H. Laby, *Tables of Physical Constants and Chemical Constants and Some Mathematical Functions*, 16th ed. (Longman, New York, 1995) [Russ. transl. of earlier ed., Fizmatgiz, Moscow 1962, 248 pp.).
[9] V. B. Atrashkevich, O. V. Vedeneev, H. R. Allan *et al.*, Yad. Fiz. **29**, 712 (1978) [Sov. J. Nucl. Phys. **29**, 366 (1978)].
[10] M. P. Dolukhanov, *Radiowave Propagation* [in Russian], Svyaz', Moscow (1972), 336 pp.

Translated by R. M. Durham

Increasing in the rate constant for dissociative attachment of electrons to hydrogen molecules by vibrational pumping during flow in a channel

F. G. Baksht and V. G. Ivanov

A. F. Ioffe Physicotechnical Institute, Russian Academy of Sciences, St. Petersburg
(Submitted July 15, 1998)
Pis'ma Zh. Tekh. Fiz. **24**, 69–75 (December 26, 1998)

An investigation is made of the electron–vibrational kinetics in a stream of vibrationally excited hydrogen flowing in a channel. It is shown that for suitably organized flow and a suitable choice of material for the channel walls, the rate constant $\langle K_{\mathrm{DA}}\rangle$ for dissociative attachment of electrons to hydrogen molecules may be increased substantially. The effect is controlled by the mean vibrational energy $\langle E_v^{(0)}\rangle$ of the H_2 molecules entering the channel.
 [S1063-7850(98)03012-2]

1. It has been shown[1] that the rate constant for dissociative attachment $\langle K'_{\mathrm{DA}}\rangle=\Sigma_v f'_v K_v(T'_e)$ can be increased substantially by additional vibrational pumping of H_2 molecules in a hydrogen stream flowing in a channel whose walls are at room temperature T and are made of a material with a high potential barrier for adsorption of H_2. Here f'_v is the vibrational distribution function of the H_2 molecules at the channel exit normalized to unity, $K_v(T'_e)$ is the rate constant for dissociative attachment of an electron to a molecule excited to level v (Refs. 2 and 3), and T'_e is the electron temperature in the chamber into which vibrationally pumped hydrogen flows from the channel. It is assumed that the initial vibrational excitation of H_2 takes place in a low-voltage Cs–H_2 discharge. The parameters of this discharge plasma have been determined fairly accurately theoretically.[4] The channel walls are assumed to be the face of a Cu(111) single crystal for which the probabilities of adsorption[5] and desorption[6–8] of H_2 molecules from the surface have been thoroughly studied. Unlike Ref. 1, the calculations were made assuming a finite coverage Θ of the channel walls by adsorbed H atoms.

2. The distribution of the concentrations N_{H_2} and N_{H} of molecular and atomic hydrogen over the channel length and the vibrational distribution function f_v of H_2 molecules in the channel are determined from Eqs. (2)–(4) and (6) in Ref. 1, where the losses of vibrationally excited and atomic hydrogen to the walls are expressed by N_v/τ_v and $N_{\mathrm{H}}/\tau_{\mathrm{H}}$. Here N_v are the concentrations of vibrationally excited molecules in the channel;

$$\tau_v=\frac{L^2}{\pi^2 D_{\mathrm{sd}}}+\frac{L}{v_{\mathrm{H}_2}}\frac{2-\gamma_v}{\gamma_v}, \tag{1}$$

$$\tau_{\mathrm{H}}=\frac{L^2}{\pi^2 D_{12}}+\frac{L}{v_{\mathrm{H}}}\frac{2-\gamma_{\mathrm{H}}}{\gamma_{\mathrm{H}}} \tag{2}$$

are the effective particle lifetimes,[1,9] D_{sd} and D_{12} are the coefficients of self-diffusion of H_2 molecules and H atoms in H_2 molecules, respectively;

$$\gamma_v(\Theta)=w_v(T)(1-\Theta)^2, \tag{3}$$

$$\gamma_{\mathrm{H}}(\Theta)=w_{\mathrm{H}}(T)\,(1-\Theta)+\sigma_{\mathrm{ER}}^{(\mathrm{eff})}\,\sigma_{\mathrm{H}}\Theta \tag{4}$$

are the fractions of molecules excited to level v and atoms, respectively, which are lost at the surface of the channel walls, as a function of the total number of particles incident on the surface,[6,7,10,11] $w_v(T)$ and $w_{\mathrm{H}}(T)$ are the probabilities of attachment of an H_2 molecule[5] excited to level v and an H atom to the Cu(111) surface at the gas temperature T in the channel, $\sigma_H\cong 1.5\times 10^5\ \mathrm{cm}^{-2}$ is the density of sorption centers at the Cu(111) surface,[12] and $\sigma_{\mathrm{ER}}^{(\mathrm{eff})}\cong 5\,\dot{A}^2$ is the effective cross section for surface recombination by the Eley–Rideal mechanism.[6,7] It was assumed that at $T\cong 300$ K the probability is $w_{\mathrm{H}}\cong 1$ (see Ref. 13). The value of $\sigma_{\mathrm{ER}}^{(\mathrm{eff})}$ used is the result of an analysis of the experimental data[12] made in Ref. 7. For these values of w_{H} and $\sigma_{\mathrm{ER}}^{(\mathrm{eff})}$, we have $\gamma_{\mathrm{H}}(\Theta)\sim 1$ and $\tau_{\mathrm{H}}\cong L^2/\pi^2 D_{12}$, i.e., τ_{H} is almost independent of $\gamma_{\mathrm{H}}(\Theta)$ and w_{H}.

According to Cacciatore and Billing,[5] w_v and $1/\tau_v$ are only nonzero for $v\geqslant 5$. In contrast, desorption of vibrationally excited H_2 molecules from the walls by the Eley–Rideal (ER) mechanism[6] and by the Langmuir–Hinshelwood (LH) mechanism[8] takes place in the range of vibrational numbers $1\leqslant v\leqslant 4$ (for LH desorption the vibrational distribution function is determined from the principle of detailed equilibrium). As a result of the comparatively high populations N_v and frequent transitions to $v\leqslant 4$ lower levels, desorption of vibrationally excited molecules from the walls has little influence on the vibrational distribution function in the channel. This influence was taken into account approximately by assuming that the desorbed molecules are uniformly distributed over the channel width L. The coverage Θ was determined from

$$\left[2\sum_v N_v/\tau_v(\Theta)+N_{\mathrm{H}}/\tau_{\mathrm{H}}\right]L = 2L\,(N_{\mathrm{H}}/\tau_{\mathrm{H}})\,\sigma_{\mathrm{ER}}^{(\mathrm{eff})}\sigma_{\mathrm{H}}\Theta/\gamma_{\mathrm{H}}(\Theta)+2\,\delta_{\mathrm{LH}}\Theta^2. \tag{5}$$

The left-hand side of Eq. (5) gives the number of H atoms adsorbed per unit time on the walls per unit channel length. The right-hand side gives twice the number of H_2 molecules

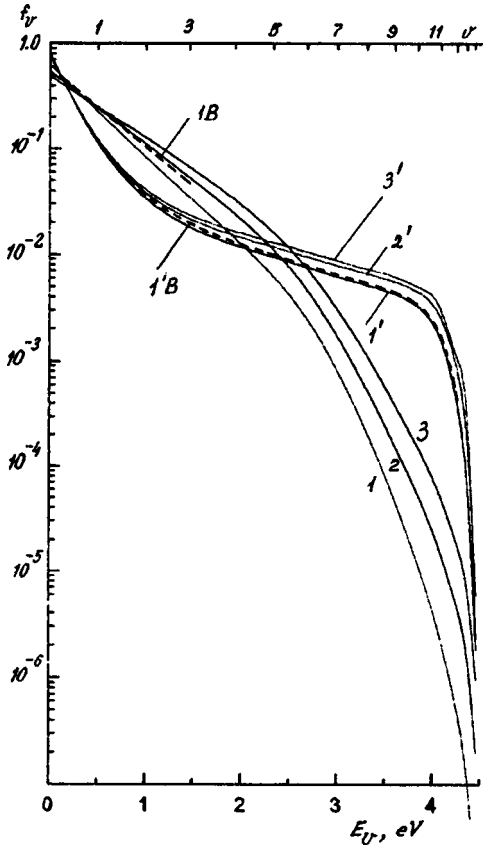

FIG. 1. Vibrational distribution functions of H_2 molecules at the entrance to the channel $f_v^{(0)}$ (*1–3*) and at the channel exit f_v' (*1′–3′*): *1B* and *1′B* — Boltzmann distribution at the channel entrance and corresponding vibrational distribution at channel exit $L=0.3$ cm, $h=3$ cm, $T=0.03$ eV. Discharge parameters: $N_{H_2}^{(0)}=10^{16}\,\mathrm{cm}^{-3}$, $N_{Cs}^{(0)}=10^{14}\,\mathrm{cm}^{-3}$, $T_0=0.06$ eV, $j_s=10\,\mathrm{A/cm}^2$: *1* — $T_e=0.53$ eV, $\langle E_v^{(0)}\rangle=0.303$ eV, $n_e=5.8\times10^{13}\,\mathrm{cm}^{-3}$, $\varphi_1=3.01$ V, $\varphi_2=1.09$ V, $N_H^{(0)}=4.0\times10^{13}\,\mathrm{cm}^{-3}$; *2* — $T_e=0.75$ eV, $\langle E_v^{(0)}\rangle=0.411$ eV, $n_e=7.25\times10^{13}\,\mathrm{cm}^{-3}$, $\varphi_1=6.13$ V, $\varphi_2=2.04$ V, $N_H^{(0)}=1.85\times10^{14}\,\mathrm{cm}^{-3}$; *3* — $T_e=1.0$ eV, $\langle E_v^{(0)}\rangle=0.496$ eV, $n_e=8.8\times10^{13}\,\mathrm{cm}^{-3}$, $\varphi_1=8.96$ V, $\varphi_2=2.91$ V, $N_H^{(0)}=3.43\times10^{14}\,\mathrm{cm}^{-3}$.

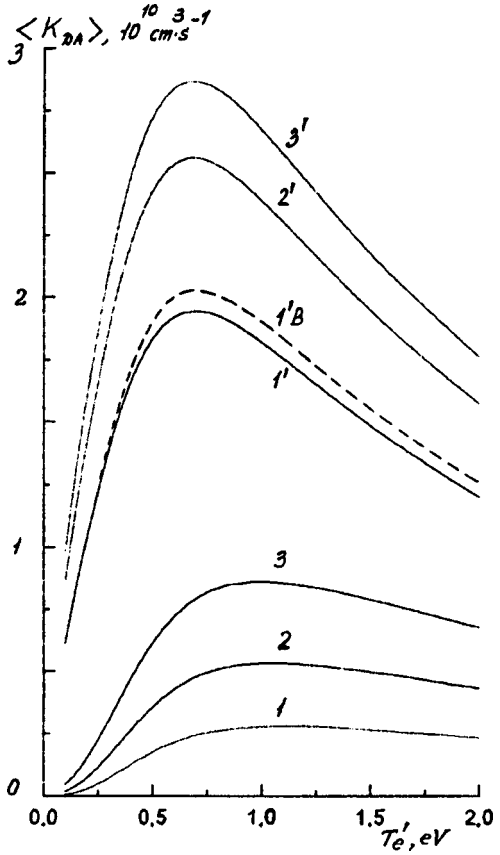

FIG. 2. Rate constants for dissociative attachment versus electron temperature T_e' in chamber: *1–3* — $\langle K_{DA}^{(0)}\rangle$; *1′–3′* — $\langle K_{DA}'\rangle$; *1′B* — value of $\langle K_{DA}'\rangle$ at channel exit corresponding to the initial Boltzmann distribution *1B* in Fig. 1. The discharge parameters are the same as in Fig. 1.

desorbed from both channel walls by the ER and LH mechanisms. The rate constants δ_{LH} for LH desorption were determined using experimental data.[8]

3. Figure 1 shows the vibrational distribution function $f_v^{(0)}$ of H_2 molecules in the discharge, i.e., at the entrance to the channel (curves *1–3*) and the corresponding distribution functions f_v' at the channel exit (curves *1′–3′*). Here $N_{H_2}^{(0)}$, $N_H^{(0)}$, $N_{Cs}^{(0)}$, T_0, and j_s are the concentrations of H_2, and H, the total Cs concentration, the gas temperature in the discharge, and the emission current density, respectively. Curves *1–3* are plotted for different discharge voltages $U=\varphi_1-\varphi_2$ and therefore different electron temperatures T_e and average vibrational energies $\langle E_v^{(0)}\rangle$ of the H_2 molecules.[1] The channel length h was approximately optimum for the largest increase in the dissociative attachment constant $\langle K_{DA}\rangle$. Significantly, we find $h\gg V\overline{\tau_v}$, where $\overline{\tau_v}$ is the characteristic vibrational deexcitation time of the levels and V is the hydrodynamic velocity in the channel. Thus, the system of equations (4) in Ref. 1 which is used to find N_v contains small parameters before the derivatives. This has the result that f_v' does not depend on the initial vibrational distribution function $f_v^{(0)}$ and is determined only by the vibrational energy $\langle E_v^{(0)}\rangle$ at the entrance to the channel (see Ref. 14). In order to demonstrate this, Fig. 1 gives the result of calculations in which the initial vibrational distribution function $f_v^{(0)}$ is replaced by a truncated Boltzmann distribution for $0\leqslant v\leqslant 4$ (curve *1*B) with the same vibrational energy $\langle E_v^{(0)}\rangle$ as for $f_v^{(0)}$ (curve *1*). The vibrational distribution obtained at the channel exit (curve *1′*B) is almost the same as the accurate calculated curve *1′*.

Figure 2 gives the dissociative attachment constants $\langle K_{DA}^{(0)}\rangle=\Sigma_v f_v^{(0)}K_v(T_e')$ (curves *1–3*), corresponding to the initial distribution function $f_v^{(0)}$, and the constants $\langle K_{DA}'\rangle$ at the channel exit (curves *1′–3′*). It can be seen that $\langle K_{DA}'\rangle$ is significantly higher than $\langle K_{DA}^{(0)}\rangle$. Allowance for a finite value of Θ has the result that the ratio $\langle K_{DA}'\rangle/\langle K_{DA}^{(0)}\rangle$ is substantially higher than that obtained in Ref. 1. From this it follows that f_v' and $\langle K_{DA}'\rangle$ only depend on $\langle E_v^{(0)}\rangle$. This is significant because in view of the lack of reliable data on the constants of interlevel transitions for large v, the populations $N_v^{(0)}$ of the H_2 upper levels may be determined with some error. However, the vibrational energy $\langle E_v^{(0)}\rangle$ concentrated in the lower levels is determined fairly reliably. In order to estimate the dependence of the results on the calculated constants, we used the constants for $v-t$ exchange with H atoms from Ref. 15 (unlike the previous calculations, where data from Ref. 16 were used). This produced a substantial increase in $N_v^{(0)}$ for

large v, but barely influenced $\langle E_v^{(0)} \rangle$ and $\langle K'_{\mathrm{DA}} \rangle$, nor $\langle K_{\mathrm{DA}}^{(0)} \rangle$ (only the values of $f_v^{(0)}$ for $v \leqslant 7$–8 are important for the calculations of $\langle K_{\mathrm{DA}}^{(0)} \rangle$).

Thus, we have shown that the rate constant for dissociative attachment $\langle K_{\mathrm{DA}} \rangle$ can be increased substantially with a suitably organized flow of vibrationally excited hydrogen in the channel.

The authors would like to thank S. M. Shkol'nik for useful discussions.

This work was supported by INTAS Grant No. 94-316.

[1] F. G. Baksht and V. G. Ivanov, Zh. Tekh. Fiz. **68**(10), 10 (1998) [Tech. Phys. **43**, 1145 (1998)].
[2] J. M. Wadehra, Phys. Rev. A **29**, 106 (1984).
[3] D. A. Skinner, A. M. Brunetau, P. Berlemont, C. Courteille, R. Leroy, and M. Bacal, Phys. Rev. E **48**, 2122 (1993).
[4] F. G. Baksht, G. A. Djuzhev, L. I. Elizarov, V. G. Ivanov, A. A. Kostin, and S. M. Shkolnik, Plasma Sources Sci. Technol. **3**(2), 88 (1994).
[5] M. Cacciatore and G. D. Billing, Surf. Sci. **232**, 35 (1990).
[6] M. Persson and B. Jackson, J. Chem. Phys. **102**, 1078 (1995).
[7] B. Jackson and M. Persson, J. Chem. Phys. **103**, 6257 (1995).
[8] G. Anger, A. Winkler, and K. D. Rendulic, Surf. Sci. **220**, 1 (1989).
[9] Yu. Z. Ionikh, Opt. Spektrosk. **51**, 76 (1981) [Opt. Spectrosc. **51**, 39 (1981)].
[10] M. A. Pick and K. Sonnenberg, J. Nucl. Mater. **131**, 208 (1985).
[11] P. L. Andrew and A. A. Haasz, J. Appl. Phys. **72**, 2749 (1992).
[12] C. T. Rettner, Phys. Rev. Lett. **69**, 383 (1992).
[13] U. Bischler, P. Sandl, and E. Bertel, Phys. Rev. Lett. **70**, 3603 (1993).
[14] F. G. Baksht, G. A. Dyuzhev, L. I. Elizarov, V. G. Ivanov, A. G. Nikitin, and S. M. Shkol'nik, Pis'ma Zh. Tekh. Fiz. **19**(22), 39 (1993) [Tech. Phys. Lett. **23**, 716 (1993)].
[15] E. Garcia and A. Lagana, Chem. Phys. Lett. **123**, 365 (1986).
[16] G. C. Schatz, Chem. Phys. Lett. **94**, 183 (1983).

Translated by R. M. Durham

Drag and heat exchange of an object in a supersonic flow with a planar source of energy in front of the object

G. A. Luk'yanov

Institute of High-Performance Computations and Databases, St. Petersburg
(Submitted May 20, 1998)
Pis'ma Zh. Tekh. Fiz. **24**, 76–82 (December 26, 1998)

The problem of a steady-state wake behind an energy source in a supersonic gas flow is analyzed and solved. The energy source is a planar gasdynamic discontinuity supplying a given energy to the flow. The parameters behind the source correspond to the weak detonation regime (supersonic combustion). The solution obtained is used to investigate the drag and heat exchange of an object in the wake behind the source. It is shown that the drag and thermal loads of the object may be reduced appreciably when the Mach numbers of the incoming flow are fairly high. An investigation was made of the energy efficiency of this method of reducing the drag and thermal loads of an object. The conditions under which this method is energetically favorable are determined. © *1998 American Institute of Physics.* [S1063-7850(98)03112-7]

Recent years have seen the publication of various studies devoted to the mathematical modeling and experimental investigation of the flow of a supersonic stream around objects when a bulk energy source is located in front of the object.[1–5] It has been shown that under certain conditions (Mach numbers M_∞, shape of object, energy source parameters, and so on) supplying energy to a supersonic flow ahead of an object can substantially reduce (by up to a factor of 2) the aerodynamic drag of the object. The formation of a thermal wake behind the energy source with a reduced dynamic pressure compared with the unperturbed flow is the mechanism responsible for reducing the drag.

In some of the cases considered in Refs. 1–3, the total energy dissipated per unit time in the horizontal motion of the object at constant velocity u_∞, equal to $N_i+F_iu_\infty$ (N_i is the power of the energy source and F_i is the drag of the object when $N_i>0$) is lower than the similar value F_0u_∞ required for motion of the object when $N_i=0$.

The results of Refs. 1–5 indicate that research in this new field of physical gasdynamics holds great promise, possibly laying the foundations for the aerophysics of fundamentally new supersonic aircraft using the principle of energetic action on the incoming gas flow. However, our level of understanding of this problem is far from adequate. Existing results are fairly special and there is no general understanding of the pattern of interaction between a supersonic flow and an energy source or of the flow behind the source. The potential scope for energetic action on a flow over a wide range of determining parameters (Mach numbers M, input energy parameters, and so on) as a method of reducing the drag and thermal loads of an object in a supersonic flow is also by no means clear. This state of affairs arises from the present lack of any suitable theoretical foundation. The development of such a foundation is a matter for immediate action. The present study is a step in this direction. The results described below are presented in greater detail in Ref. 6.

The flow pattern studied is shown in Fig. 1a. A region of energy release having the transverse dimension $2b$ and a short downstream length is positioned in front of an object in a steady-state supersonic flow. Neglecting the flow structure inside the thin layer, we consider a planar gasdynamic discontinuity ($x=0$, $|y|\leqslant b$) supplying a given energy to the gas flowing through the discontinuity as the model energy source. These steady-state flow regimes correspond to weak detonation.[7]

The parameters behind the planar energy source are determined from the mass, momentum, and energy conservation laws, supplemented by the equation of state

$$\rho_i u_i=\rho_\infty u_\infty, \tag{1}$$

$$p_i+\rho_i u_i^2=p_\infty+\rho_\infty u_\infty^2, \tag{2}$$

$$\rho_i u_i\left(\frac{u_i^2}{2}+c_pT_i\right)=\rho_\infty u_\infty\left(\frac{u_\infty^2}{2}+c_pT_\infty\right)+\rho_\infty u_\infty q, \tag{3}$$

$$p=\rho RT. \tag{4}$$

Here ρ is the gas density, p is the pressure, T is the temperature, u is the velocity, R is the gas constant, c_p is the specific heat, q is the energy supplied to the energy source per unit mass of gas per unit time, and the subscripts ∞ and i refer to the parameters in front of and behind the source, respectively.

The solution of the system of equations (1)–(4) for the weak detonation regime (see Ref. 7 for example) has the form

$$\lambda_i=\frac{1}{2(1+\beta)^{1/2}}\left\{\lambda_\infty+\frac{1}{\lambda_\infty}+\left[\left(\lambda_\infty-\frac{1}{\lambda_\infty}\right)^2-4\beta\right]^{1/2}\right\}, \tag{5}$$

$$\varkappa_i=\rho_i/\rho_\infty=\lambda_\infty/\lambda_i(1+\beta)^{1/2}, \tag{6}$$

$$\tau_i=T_i/T_\infty=\beta(1-\lambda_i^2/\epsilon)/(1-\lambda_\infty^2/\epsilon), \tag{7}$$

$$n_i=p_i/p_\infty=\rho_iT_i/\rho_\infty T_\infty. \tag{8}$$

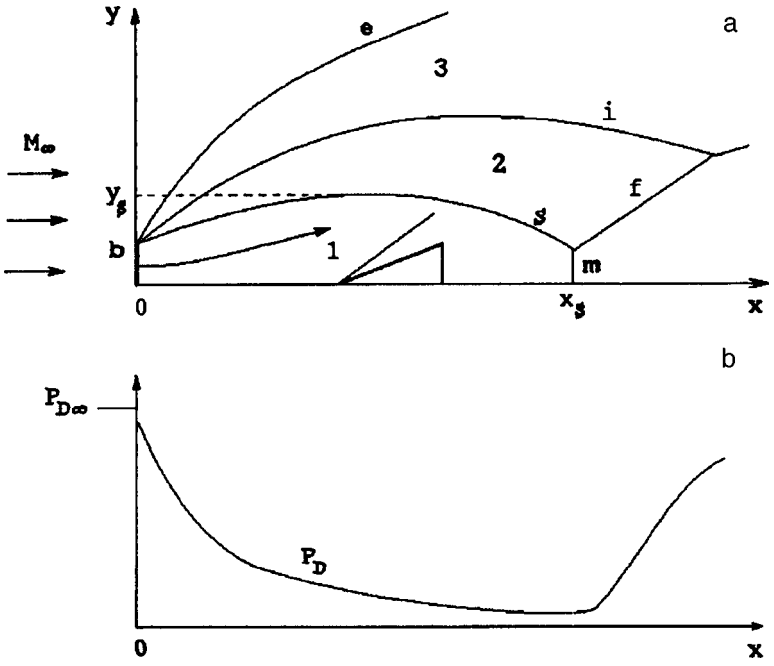

FIG. 1. a — Flow pattern in the wake behind a planar energy source in a supersonic flow and b — change in the dynamic pressure p_D along the axis of the wake.

Here $\lambda = u/u_*$ is the coefficient of velocity, u_* is the critical velocity, $\beta = q/c_p T_{0\infty}$ is the heating parameter, $T_{0\infty}$ is the initial temperature of the incoming flow, $\epsilon = (\gamma+1)/(\gamma-1)$, and γ is the ratio of the specific heats.

The limiting value of β at which thermal crisis occurs and subsequent steady-state heat transfer is impossible corresponds to $\lambda_i = 1$ and is given by

$$\beta_*(M)_\infty = (M_\infty^2 - 1)^2/2(\gamma+1)\left(1 + \frac{\gamma-1}{2}M_\infty^2\right). \quad (9)$$

The corresponding limiting values of $\varkappa_i, \tau_i$, and n_i are given by

$$\varkappa_* = \left[\frac{\gamma+1}{2}M_\infty^2\left(1 + \frac{\gamma-1}{2}M_\infty^2\right)\right]^{1/2} \Big/ (1+\beta_*)^{1/2}, \quad (10)$$

$$\tau_* = 2(1+\beta_*)\left(1 + \frac{\gamma-1}{2}M_\infty^2\right) \Big/ (\gamma+1), \quad (11)$$

$$n_* = \left[\frac{\gamma+1}{2}M_\infty^2 \Big/ \left(1 + \frac{\gamma-1}{2}M_\infty^2\right)(1+\beta)\right]^{1/2}. \quad (12)$$

For $M_\infty \gg 1$ Eqs. (10)–(12) take the form

$$\varkappa_* \simeq (\gamma+1)/\gamma, \quad \tau_* \simeq \gamma^2 M_\infty^2/(\gamma+1)^2,$$
$$n_* \simeq \gamma M_\infty^2/(\gamma+1). \quad (13)$$

In our particular problem, the wake behind the planar energy source is a supersonic underexpanded jet in an accompanying supersonic flow (Fig. 1a). This type of flow was investigated in fairly great detail in Refs. 8 and 9. Heating of the gas in the energy source leads to a rise in pressure and subsequent expansion of the gas. In the wake behind the source five surfaces of strong discontinuity are formed whose position is determined by the flow structure. The stream of heated gas is separated from the stream of cold gas flowing past the source by a tangential discontinuity *i*. The surface *e* is the bow shock wave while the surfaces *s*, *f*, and *m* are the suspended, reflected, and central shock waves, respectively. These surfaces of discontinuity separate the regions of free expansion *1*, the compressed layer of the jet *2*, and the compressed layer of the outer stream *3*.

The flow pattern is qualitatively the same in the two-dimensional and axisymmetric variants. The flow parameters in the wake (including the flow geometry) using the model of a nonviscous ideal gas are determined by the Mach numbers M_∞ and M_i, γ, and n_i. In the region of free expansion, rapid expansion of the heated gas is accompanied by a rapid drop in the dynamic pressure $p_D = \rho u^2/2$ (Fig. 1b). In this case, p_D in the region of free expansion is considerably lower than p_D in the incoming stream. This is the main factor in the mechanism responsible for reducing the drag of an object in the wake behind this type of energy source.

From data obtained[8] by generalizing numerical analyses of nonviscous axisymmetric jets in an accompanying supersonic stream for $n \gg 1$ and $\gamma = 1.4$, the longitudinal and transverse dimensions of the region of free expansion are approximately

$$x_s/b \simeq 0.5 M_i\sqrt{n}, \quad y_s/b \simeq M_i\sqrt{n}/M_\infty. \quad (14)$$

For two-dimensional flow we have

$$x_s/b \sim M_i n, \quad y_s/b \sim M_i n/M_\infty. \quad (15)$$

The drag of an object moving in the region of free expansion of the wake is given by

$$F_1 = C_{x1}\frac{\rho_1 u_1^2}{2}S, \quad (16)$$

where C_{x1} is the drag coefficient, ρ_1 and u_1 are the density and velocity of the gas in front of the object in the region of free expansion, and S is the area of the midsection of the object. In order to estimate the efficiency with which the drag of an object is reduced in this flow scheme, we introduce the parameter

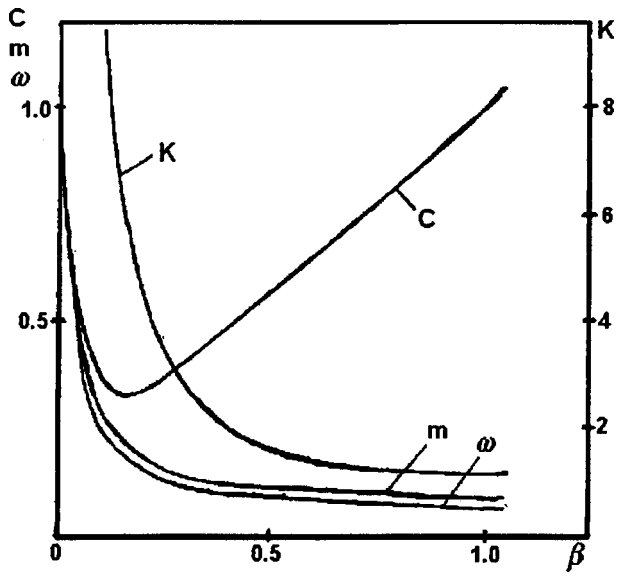

FIG. 2. Dependences of ω, m, K, and C on the heating parameter β for $M_\infty=10$ and $\gamma=1.4$.

$$\omega=F_1/F_0=(C_{x1}/C_{x\infty})(\rho_1 u_1^2/\rho_\infty u_\infty^2). \tag{17}$$

The ratio for the total heat flows to the object similar to (17) is

$$m=(C_{H_1}/C_{H\infty})(\rho_1 u_1^3/\rho_\infty u_\infty^3), \tag{18}$$

where C_H is the coefficient of heat transfer. The minimum values of ω and m are achieved at the end of the region of free expansion. For $C_{x1}=C_{x\infty}$, $C_{H1}=C_{H\infty}$, $M_\infty\gg 1$, and $M_1\gg 1$ the limiting (lowest) values of ω and m are approximately

$$\omega_m\simeq\varkappa_*(1+\beta_*)/n_*=(\gamma+1)^2/M_\infty^2, \tag{19}$$

$$m_m\simeq\omega_m\gamma/(\gamma^2-1)^{1/2}=\gamma(\gamma+1)^2/(\gamma^2-1)^{1/2}M_\infty^2. \tag{20}$$

Figure 2 plots ω and m as functions of the heating parameter β for $M_\infty=10$, $\gamma=1.4$, $C_{x1}=C_{x\infty}$, and $C_{H1}=C_{H\infty}$. The limiting values of ω and m are 0.06 and 0.085, respectively. The estimates of ω given in Fig. 2 are confirmed by the calculated results[6] for axisymmetric flow.

We shall estimate the efficiency of using this type of energy source as a means of reducing the drag, using the parameters[6]

$$K=(N_0-N_1)/N_i, \quad C=(N_1+N_i)/N_0, \tag{21}$$

where $N_i=\rho_\infty u_\infty c_p S_i(T_{0i}-T_{0\infty})$, $N_0=F_0u_\infty$, $N_1=F_1u_\infty$.

Using formula (17) we can transform the expressions (21) to give

$$K=C_{x\infty}\frac{\gamma-1}{2}\frac{M_\infty^2}{1+(\gamma-1)M_\infty^2/2}\frac{S}{S_i\beta}(1-\omega), \tag{22}$$

$$C=\omega+\frac{2}{C_{x\infty}}(\gamma-1)\frac{1+(\gamma-1)M_\infty^2/2}{M_\infty^2}\frac{S_1\beta}{S}. \tag{23}$$

By way of example, Fig. 2 gives K and C as a function of β for $M_\infty=10$, $\gamma=1.4$, $C_{x1}=C_{x\infty}=1$, and $S=S_i$. For small β, highly energy-efficient regimes are achieved, corresponding to $K\gg 1$. However, the reduction in the drag is relatively small. As β increases, the value of K decreases monotonically. The total energy dissipated in the motion of the object has a minimum at moderate values of β which for $M_\infty=10$ correspond to values of ω and m of the order of 0.2–0.3. Estimates of K and C were obtained for $C_{x1}=C_{x\infty}=1$. At significantly lower values of C_x the scope for achieving energetically favorable regimes of motion is reduced appreciably. The fundamental possibility of reducing the total thermal loads on an object at high Mach numbers M_∞ is of major interest in its own right. The thermal aspect of the problem requires more detailed analysis.

[1] P. Yu. Georgievskiĭ and V. A. Levin, Pis'ma Zh. Tekh. Fiz. **14**, 684 (1988) [Sov. Tech. Phys. Lett. **14**, 303 (1988)].
[2] V. A. Levin and L. V. Teren't'eva, Izv. Akad. Nauk SSSR. Ser. Mekh. Zhidk. Gaza No. 2, 110 (1993).
[3] V. Yu. Borzov, I. V. Rybka, and A. S. Yur'ev, Inzh.-Fiz. Zh. **67**(5–6), 355 (1994).
[4] P. K. Tret'yakov, A. F. Garanin, G. N. Grachev *et al.*, Dokl. Ross. Akad. Nauk **351**, 339 (1996) [Phys. Dokl. **41**, 566 (1996)].
[5] S. V. Guvernyuk and A. B. Samoĭlov, Pis'ma Zh. Tekh. Fiz. **23**(9), 1 (1997) [Tech. Phys. Lett. **23**, 333 (1997)].
[6] G. A. Luk'yanov, Preprint No. 04–98 [in Russian], Institute of High-Performance Computations and Databases, St. Petersburg.
[7] G. G. Chernyĭ, *Gasdynamics* [in Russian], Nauka, Moscow (1988), 424 pp.
[8] V. S. Avduevskiĭ, É. A. Ashratov, A. V. Ivanova, and U. G. Pirumov, *Gasdynamics of Supersonic Nonisobaric Jets* [in Russian], Mashinostroenie, Moscow (1989), 320 pp.
[9] V. G. Dulov and G. A. Luk'yanov, *Gasdynamics of Flow Processes* [in Russian], Nauka, Novosibirsk (1994), 234 pp.

Translated by R. M. Durham

Characteristics of series-connected chains of YBaCuO Josephson junctions on a bicrystal substrate

A. A. Verevkin, V. A. Il'in, A. P. Lipatov, D. V. Meledin, and A. A. Naumov

Moscow State Pedagogical University
(Submitted May 8, 1998)
Pis'ma Zh. Tekh. Fiz. **24**, 83–89 (December 26, 1998)

An investigation was made of the electrophysical characteristics of chains of high-temperature superconducting Josephson junctions on a bicrystal substrate. Their interaction with millimeter radiation was also studied. It was shown that these chains can be used to detect millimeter and submillimeter radiation. © *1998 American Institute of Physics.* [S1063-7850(98)03212-1]

It is known[1,2] that the use of series-connected chains of Josephson junctions in low-noise broad-band detectors for electromagnetic radiation can overcome may of the difficulties encountered when single Josephson junctions are used for this purpose. Using chains of Josephson junctions increases the dynamic range of the devices N times, where N is the number of junctions in the chain,[2] and the resistances of the nonlinear elements can be optimized from the point of view of achieving the highest degree of matching. In addition, structures with higher critical currents can be used in chain systems than with single junctions with the same resistance and thus the former are more stable to current overloads.

These advantages have stimulated the development of chains of Josephson junctions using low-temperature superconductors specially designed for use in microwave devices.[2–4] They have been used to produce receiving elements with highly stable and reproducible parameters and to fabricate Josephson radiometers with almost optimal maximum fluctuation sensitivity over a large dynamic range.[3] The main limitation is the technological feasibility of fabricating chains containing separate junctions with identical or at least similar characteristics.

To date, the Josephson junctions with the most reproducible parameters among the high-temperature superconductors have been fabricated from films of YBaCuO deposited on bicrystal substrates.[5,6] Strontium titanate and other high-permittivity materials have conventionally been used for this purpose, which has limited their application in microwave devices.

At present, among the high-temperature superconductors, films of YBaCuO deposited on bicrystal substrates have been used to fabricate Josephson junctions with the most reproducible parameters.[5,6] Strontium titanate and other high-permittivity materials have conventionally been used for this purpose, which has limited their application in microwave devices.

The aim of the present study is to determine the electrophysical characteristics of chains of YBaCuO Josephson junctions fabricated on bicrystal ZrO_2 substrates and to investigate the characteristics of their interaction with microwave radiation in the short-wavelength part of the millimeter range.

The chains were fabricated using YBaCuO films ~ 200 nm thick, deposited by magnetron sputtering on bicrystal substrates of yttrium-stabilized ZrO_2 ($\varepsilon \approx 28$ at $T = 77$ K) with the crystallographic axes misoriented by 32°. Junctions in the form of bridges 2–6 μm wide were formed at the bicrystal boundary by wet photolithography. The chains contain 3–11 series-connected bridges. The Josephson junctions are matched with the incident radiation by means of planar butterfly antennae.[7] For comparison we also investigated single Josephson junctions made in the same fabrication cycle as the chains of junctions. The single junctions had normal resistances $R_n = 2.5$–$5\ \Omega$ and critical currents $I_c = 5$–$35\ \mu$A at $T = 77$ K and 10–120 μA at $T = 10$ K. The normal resistances of the chains varied in the range 8.5–15 Ω and the critical currents were 10–35 μA and 50–92 μA at 77 K and 10 K, respectively. The fabrication technology produced chains of Josephson junctions for which the spread of the critical currents of the individual junctions was less than 5%.

For the measurements in the millimeter wavelength range, the substrate with the structures was placed in the detector chamber so that the radiation was incident on either the side of the superconducting structure or on the substrate side. The investigations were carried out at temperatures in the range 6–89 K. The radiation frequency varied between 128 and 145 GHz and its power measured at the exit from the detector chamber was 10^{-8}–10^{-5} W.

Figure 1 gives the results of investigations of a single Josephson junction with a critical current of 120 μA and normal resistance of 3 Ω. Curve *1* gives the current–voltage characteristic obtained at $T = 14$ K when radiation at a frequency of 135 GHz was incident on the junction from the structure side. The characteristic shows Shapiro current steps whose exact position can be determined from the dependence of the differential resistance of the junction on its bias voltage $R_d(V)$, which is also plotted (curve *2*). Four steps are clearly visible at bias voltages below 1.1 mV. Note that the characteristic voltage ($V_c = I_c R_n$) for this junction is 530 μV. When the radiation was incident from the substrate side,

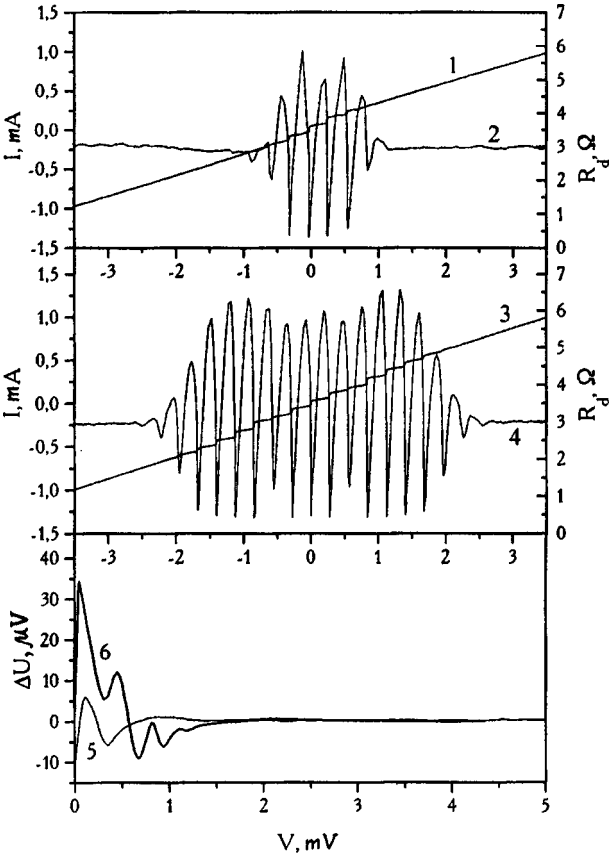

FIG. 1. Current–voltage characteristics of a single Josephson junction exposed to microwave power on the structure side (*1*) and on the substrate side (*3*), and dependences of the differential resistance (*2*) and (*4*) and the response (*5*) and (*6*) on the junction voltage measured under the same conditions.

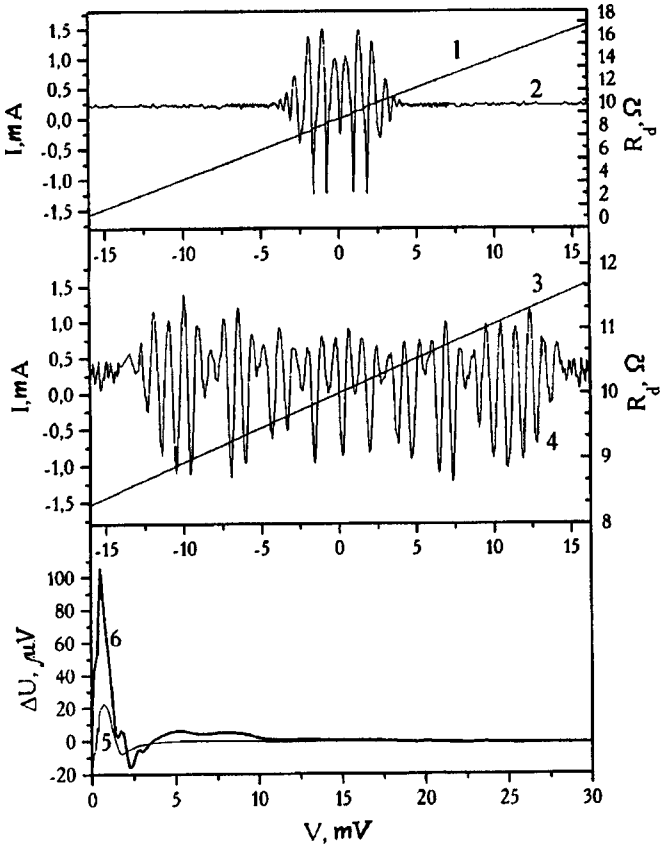

FIG. 2. Current–voltage characteristics of a chain of Josephson junctions exposed to microwave power on the structure side (*1*) and on the substrate side (*3*), and dependences of the differential resistance (*2*) and (*4*) and the response (*5*) and (*6*) on the junction voltage measured under the same conditions.

its current–voltage characteristic and $R_d(V)$ clearly show nine steps at voltages below 2.5 mV (see curves *3* and *4* in Fig. 1). The response of a single junction to microwave radiation incident on the structure side and on the substrate side is given by curves *5* and *6* in Fig. 1, respectively.

Figure 2 gives the results of similar investigations of chains of three Josephson junctions with $R_n = 9.5\,\Omega$ and $I_c = 60\,\mu$A, obtained at $T = 20$ K. The radiation frequency was 131.5 GHz. When the radiation was incident on the structure side, the current–voltage characteristic and the $R_d(V)$ curves reveal six steps at bias voltages below 4 mV (curves *1* and *2*, respectively). When the radiation was incident on the substrate side, these curves exhibit 17 Shapiro steps up to 14 mV (curves *3* and *4*). Curves *5* and *6* give the response of a chain of Josephson junctions measured for the same orientation of the substrate relative to the incident radiation as in Fig. 1 for a single junction.

Thus, the response to the radiation and the number of Shapiro steps for radiation incident on the substrate side is substantially (between four and ten times) higher than that for radiation incident on the structure side. This result is a direct consequence of the asymmetry of the angular distribution of a planar antenna formed on a thin dielectric substrate with high ε (Ref. 7).

The results plotted in Figs. 1 and 2 can be used to estimate the voltage–power sensitivity η of a detector using a chain of Josephson junctions or a single junction as the nonlinear element. This sensitivity is 60 and 18 V/W respectively at $T \sim 20$ K; at $T \sim 60$ K η decreased by a factor of 1.5–2. Thus, the sensitivity η for a chain of Josephson junctions is substantially higher than that for a single junction. This is evidently because the normal resistance of the chain is three times higher than that of a single junction, which improves the matching of the element with the microwave radiation approximately threefold.

Although the spacing between the steps on the current–voltage characteristic is three times greater for the chain than for the single junction, in the first case there are 1.5–2 times more steps than in the second. This effect can be attributed to the partial synchronization of the contacts observed under the action of external monochromatic radiation, and its interaction with the Josephson self-radiation in a resonant electrodynamic system such as the detector chamber with an inserted Josephson junction or chain of junctions.[8–10]

The shape and behavior of the current–voltage characteristics in an electromagnetic field and also the dependence of the step height on the microwave power are accurately described using a resistive model.[2] However, the dependence of the microwave response on the voltage for a chain of Josephson junctions measured under the same conditions has a number of notable features. Of particular note is that in addition to the usual Josephson response observed at low

bias voltages <5 mV, a negative response component is also observed at bias voltages above 8 mV. This is caused by the increased quasiparticle conduction of the junctions as a result of photostimulation of inelastic resonant tunneling via a finite number of trapped states.[11] A similar effect was observed for single Josephson junctions on a bicrystal substrate.[12,13]

The parameters of these response components differ substantially. For example, at a radiation power of $\sim 10^{-7}$ W the voltage–power sensitivity of a detector comprising a chain of Josephson junctions was 60 V/W in the range of bias voltages where the Josephson response predominates and only 5 V/W in the range where the response caused by the quasiparticle conduction predominates. The Josephson response component has no structure attributable to a difference between the critical currents of the separate junctions in the chain, which also indicates that the characteristics of the individual junctions in the chain are similar. However, the curve describing the quasiparticle response is jagged, which suggests a strong dependence on the parameters of the junctions in the chain (this structure cannot be identified on curve *5* in Fig. 2 because of the small scale).

A comparison between the experimental values of the response of single YBaCuO Josephson junctions and chains of these junctions suggests that the voltage–power sensitivity of the chains is several times higher and they have a larger dynamic range which makes them easier to use in millimeter and submillimeter wavelength detectors. This property can be attributed to their better matching with the microwave channel. Further prospects for improving the technology of chains of YBaCuO Josephson junctions could involve using bicrystal substrates with natural faces for which the spread of the parameters of individual junctions is substantially smaller.[14]

[1] A. L. Gudkov, V. A. Kulikov, V. N. Laptev *et al.*, Pis'ma Zh. Tekh. Fiz. **13**, 1109 (1987) [Sov. Tech. Phys. Lett. **13**, 462 (1987)].
[2] K. K. Likharev, *Dynamics of Josephson Junctions and Circuits* (Gordon and Breach, New York, 1986; Nauka, Moscow, 1985).
[3] A. L. Gudkov, V. A. Il'in, V. N. Laptev *et al.*, Zh. Tekh. Fiz. **58**, 2261 (1988) [Sov. Phys. Tech. Phys. **33**, 1377 (1988)].
[4] V. A. Il'in and M. D. Kitaĭgorodskiĭ, Tekh. Fiz. **60**(19), 197 (1990) [Sov. Phys. Tech. Phys. **35**, 525 (1990)].
[5] D. Dimos, P. Chaudhari, J. Manhart, and F. K. LeGoues, Phys. Rev. Lett. **61**, 219 (1988).
[6] I. I. Vengrus, S. I. Krasnosvobodtsev, M. Yu. Kupriyanov *et al.*, Sverkhprovodimost' (KIAE) **6**, 1730 (1994).
[7] B. Rutledge, D. P. Neikirk, and D. P. Kasilingam, Int. J. Infrared Millim. Waves **10**, 1 (1983).
[8] G. A. Ovsyannikov, L. S. Kuz'min, and K. K. Likharev, Radiotekh. Elektron. **27**, 1613 (1982).
[9] L. É. Amatuni, V. N. Gubankov, and G. A. Ovsyannikov, Fiz. Nizhk. Temp. **9**, 939 (1983) [Sov. J. Low Temp. Phys. **9**, 484 (1983)].
[10] A. A. Verevkin, V. A. Il'in, and A. P. Lipatov, Sverkhprovodimost' (KIAE) **8**, 745 (1995).
[11] I. I. Vengrus, M. Yu. Kupriyanov, O. V. Snigirev *et al.*, JETP Lett. **60**, 381 (1994).
[12] A. P. Lipatov, A. A. Verevkin, I. I. Vengrus *et al.*, JETP Lett. **64**, 454 (1996).
[13] A. P. Lipatov, V. A. Ilyin, A. A. Verevkin *et al.*, in *Extended Abstracts of the International Superconductive Electronics Conference, ISEC'97*, Berlin, 1997, Vol. 3, p. 129 (1997).
[14] I. I. Vengrus, A. M. Balbashov, A. V. Mozhaev *et al.*, in *Extended Abstracts of the International Superconductive Electronics Conference, ISEC'97*, Berlin, 1997, Vol. 2, p. 46 (1997).

Translated by R. M. Durham

Photoluminescence of *n*-GaN: influence of chemical treatment of the surface using sulfide solutions

Yu. V. Zhilyaev, M. E. Kompan, E. V. Konenkova, A. S. Mokeev, and S. D. Raevskiĭ

A. F. Ioffe Physicotechnical Institute, Russian Academy of Sciences, St. Petersburg
(Submitted July 16, 1998)
Pis'ma Zh. Tekh. Fiz. **24**, 90–93 (December 26, 1998)

Results are presented of the photoluminescence of *n*-GaN ($T=300$ K) after chemical treatment of the surface using solutions of inorganic sulfides (Na_2S and $(NH_4)_2S$) in water or isopropanol. It is shown that the maximum intensity of the photoluminescence spectrum of *n*-GaN increases after chemical treatment of the surface using alcohol solutions of sulfides and this increase is greater for solutions of the strong-base sulfide Na_2S compared with the weak-base sulfide $(NH_4)_2S$. © *1998 American Institute of Physics.* [S1063-7850(98)03312-6]

The development of ultraviolet semiconductor optoelectronics has necessitated the development of methods of preparing III–V nitrides as well as methods of treating their surfaces. The chemical treatment of III–V nitrides includes dry etching[1,2] and etching from NaOH (Ref. 3) or KOH solutions.[4]

Recent publications have reported theoretical[5] and experimental investigations of the electronic properties of a GaN surface treated at high temperature (1000°C) in vacuum.[6] Studies of the electronic properties of the surface of III–V semiconductors are primarily aimed at reducing the surface recombination velocity and enhancing the photoluminescence quantum efficiency, among other factors. The electronic properties of the surface have been successfully modified using solutions of Na_2S and $(NH_4)_2S$ sulfides in water[7] or alcohols.[8]

Here we attempt to use technology for passivating the surface with alcohol solutions of sulfides to enhance the electronic properties, especially to improve the photoluminescence intensity of an *n*-GaN surface.

The investigations were carried out using *n*-GaN layers ($n=5\times10^{18}$ cm^{-3}) 400–600 μm thick grown on a sapphire substrate by chloride gas-transport epitaxy.[9] During the epitaxial growth process the layers were separated from the substrate.

The chemical treatment of the GaN surface involved immersing the semiconductor for 1 min at room temperature in the following solutions: a 10% aqueous solution of $(NH_4)_2S$, a 1% solution of $(NH_4)_2S$ in isopropanol (i-C_3H_7OH), or a saturated Na_2S solution in isopropanol.

Photoluminescence was excited by a pulsed nitrogen laser ($\lambda=337$ nm, $I=20$ W) and was recorded at room temperature. The experimental technique was similar to that described by Kompan and Shabanov.[10]

The following experimental results were obtained. The photoluminescence intensity of *n*-GaN increases after sulfide treatment of the surface using an isopropanol-based solution (see Fig. 1) and remains almost constant after treatment with aqueous sulfide solutions. The most significant increase in intensity (by a factor of 1.4) compared with that of the untreated *n*-GaN is observed for a saturated solution of Na_2S in isopropanol. The full-width at half-maximum of the edge line of the *n*-GaN photoluminescence spectrum increases negligibly after chemical treatment using an alcohol solution because of the increased intensity of the long-wavelength edge of this line (see Fig. 1).

The increase in the photoluminescence intensity of GaN after chemical treatment using isopropanol-based sulfide solutions can be explained in terms of model concepts of the chemical processes accompanying the sulfide passivation of

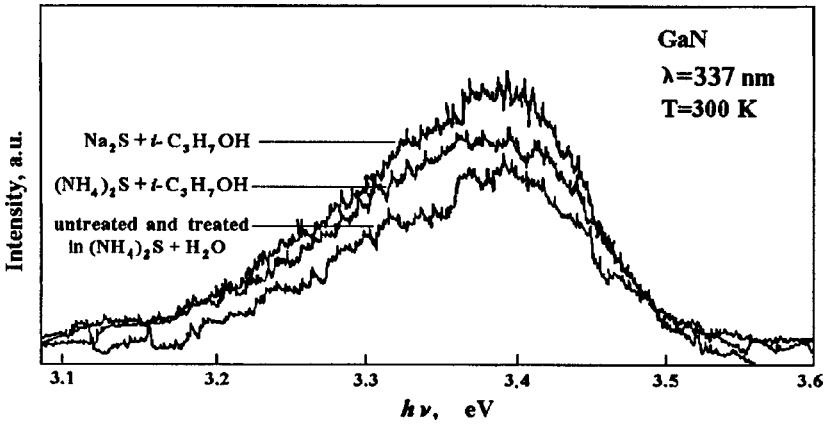

FIG. 1. Photoluminescence spectra of *n*-GaN after sulfide treatment of the surface using three different solutions: a 10% aqueous solution of $(NH_4)_2S$, a 1% solution of $(NH_4)_2S$ in isopropanol (i-C_3H_7OH), and a saturated solution of Na_2S in isopropanol (i-C_3H_7OH). The spectra are normalized to the maximum intensity of the photoluminescence spectrum of the untreated *n*-GaN.

TABLE I. Experimental values of the intensity (I) and the full-width at half-maximum (δ) of the photoluminescence spectrum for GaN and GaAs[12] after various chemical treatments using sulfide solutions.

	GaN ($n=5\times10^{18}$ cm^{-3})		GaAs ($n=1\times10^{18}$ cm^{-3}) (Ref. 12)
Chemical solution	I, a.u.	δ, eV	I, a.u.
Untreated	1.0	0.17	1.0
$(NH_4)_2S+H_2O$	1.0	0.17	1.5
$(NH_4)_2S+i$-C_3H_7OH	1.16	0.20	1.7
Na_2S+i-C_3H_7OH	1.4	0.20	2.3

a GaAs surface.[11] We know that sodium sulfide is the salt of a strong base and a weak acid, whereas ammonium sulfide is the salt of a weak base and a weak acid, so that during chemical treatment in alcohol solutions of sodium sulfide, the rate of the chemical reaction with the GaN surface should naturally be higher than the rate of the chemical reaction for treatment with alcohol solutions of ammonium sulfide. A decisive factor for improving the electronic properties of the surface during the chemical treatment of III–V semiconductors (GaAs) is the chemical reaction rate,[11] and we can therefore postulate that this also applies to III–V nitrides. Thus, since the chemical reaction rate for aqueous solutions of ammonium sulfide is the lowest among the solutions used, the efficiency of the chemical treatment of the GaN surface is very low in this case (see Table I).

A comparison between the GaN photoluminescence intensity obtained here and the GaAs photoluminescence intensity quoted by Bessolov *et al.*[12] after chemical treatment of the surface using solutions of strong-base salts (Na_2S) and weak-base salts ($(NH_4)_2S$) indicates that the degree of increase in the photoluminescence intensity for both semiconductors shows good agreement with the model concepts.[11]

To sum up, chemical treatment of the surface of n-GaN using isopropanol solutions of sulfides causes a reduction in the surface state density similar to that observed when GaN is annealed at 1000 °C and the surface bombarded with nitrogen ions.[6]

The authors would like to thank V. N. Bessolov for stimulating this work and V. M. Botnaryuk for assistance with the GaN epitaxy.

This work was partially supported by the Russian Fund for Fundamental Research (Grant No. 97-02-18088).

[1] S. J. Pearton, C. R. Abernathy, and F. Ren, Appl. Phys. Lett. **64**, 2294 (1994).
[2] M. E. Lin, Z. F. Fan, Z. Ma, L. H. Allen, and H. Markoç, Appl. Phys. Lett. **64**, 887 (1994).
[3] M. Onkubo, Jpn. J. Appl. Phys., Part 1 **36**, L955 (1997).
[4] J. R. Mileham, S. J. Pearson, C. R. Abernathy, Y. D. Mackenzie, R. J. Shul, and S. R. Kilcoyne, Appl. Phys. Lett. **67**, 1119 (1995).
[5] A. D. Bykhovski and M. S. Shur, Appl. Phys. Lett. **69**, 2397 (1996).
[6] C. I. Wu, A. Kahn, N. Taskar, D. Dorman, and D. Gallagher, J. Appl. Phys. **83**, 4249 (1998).
[7] C. J. Sandroff, R. N. Nottonburg, J. C. Bischoff, and R. Shat, Appl. Phys. Lett. **51**, 33 (1987).
[8] V. N. Bessolov, A. F. Ivankov, E. V. Konenkova, and M. V. Lebedev, Pis'ma Zh. Tekh. Fiz. **21**(1), 46 (1995) [Tech. Phys. Lett. **21**, 20 (1995)].
[9] V. V. Bel'kov, V. M. Botnaryuk, L. M. Fedorov, I. N. Goncharuk, S. V. Novikov, V. P. Ulin, Yu. V. Zhilyaev, T. S. Cheng, N. J. Jeffs, C. T. Foxon, N. I. Katsavets, and I. Harrison, J. Cryst. Growth **187**, 29 (1998).
[10] M. E. Kompan and I. Yu. Shabanov, Fiz. Tverd. Tela. (St. Petersburg) **39**, 1165 (1997) [Phys. Solid State **39**, 1030 (1997)].
[11] V. N. Bessolov, E. V. Konenkova, and M. V. Lebedev, Fiz. Tverd. Tela. (St. Petersburg) **39**, 63 (1997) [Phys. Solid State **39**, 54 (1997)].
[12] V. N. Bessolov, M. V. Lebedev, N. M. Binh, M. Friedrich, and D. R. T. Zahn, Semicond. Sci. Technol. **13** (1998) [to be published].

Translated by R. M. Durham